



SOLUTE REDISTRIBUTION AND DENDRITE MORPHOLOGY IN
IRON BASE ALLOYS

by

RICHARD VINCENT BARONE

S.B. Massachusetts Institute of Technology (1958)

S.M. Massachusetts Institute of Technology (1960)

Submitted in Partial Fulfillment of the Requirements
for the Degree of
DOCTOR OF SCIENCE
at the
Massachusetts Institute of Technology
September 1966

Signature of Author

~~Department of Metallurgy~~

Certified by

~~Thesis Supervisor~~

Accepted by

~~Chairman, Departmental Committee on
Graduate Students~~

ABSTRACTSOLUTE REDISTRIBUTION AND DENDRITE MORPHOLOGY IN
IRON BASE ALLOYS

by

RICHARD VINCENT BARONE

Submitted to the Department of Metallurgy on August 22, 1966 in partial fulfillment of the requirements for the degree of Doctor of Science.

Microsegregation and dendrite morphology were studied in detail for a series of unidirectionally solidified iron-nickel, iron-phosphorus, iron-copper, and iron-carbon-nickel alloys. In the iron-nickel alloys, over the range of compositions studied, the solidification morphology shifted from cellular to highly branched dendritic as the solute content increased and/or the solidification time increased. Primary dendrite arm spacing in the iron-nickel alloy system was found to increase with increasing solute content and to increase approximately with the solidification time raised to the 0.5 power. The addition of up to 0.4 per cent carbon in iron-nickel alloys increased the primary arm spacing and increased the tendency for higher order branching. In the iron-nickel alloys over the range of composition studied, the secondary dendrite arms ranged from being unobservable in the iron-10 per cent nickel alloy near the chill to well formed for slower cooling rates and/or higher alloy contents. The series of iron-26 per cent nickel alloys containing various amounts of carbon had approximately the same secondary spacings and were all slightly larger than the 26 per cent nickel alloy containing no carbon. The iron-25 per cent copper alloy exhibited branching and a cruciform structure in horizontal sections adjacent and parallel to the chill. Rather than forming higher order growth forms, the cruciform structure persisted and became enlarged as the distance from the chill increased. The secondary dendrite arm spacings measured in the iron-copper alloy were finer than in any other alloy studied. The iron-4.0 per cent phosphorus alloy exhibited a strong tendency to form branched dendrites; the structure of the alloy ranged from slightly branched for rapid cooling rates to highly branched dendritic for slower cooling. The secondary dendrite arm spacings in the iron phosphorus alloy were almost identical to that of the iron-26 per cent nickel alloy. The primary arm spacing in the iron-copper and iron-phosphorus alloys also increases approximately with the solidification time raised to the 0.5 power. Two characteristics of all the secondary dendrites observed were that (1) wherever the secondary dendrites were well formed their spacing was less than that of the primary arms, (2) the increase in dendrite arm spacings with solidification time was never as rapid for secondary as for primary arms.

ABSTRACT (Continued)

Microsegregation in several ingots was measured using the electron beam microprobe analyzer. The room temperature segregation ratio, S^0 , which is defined as the ratio of the maximum solute content, C_M^0 to the minimum solute content, C_m^0 , in iron-10 per cent nickel alloys varied from 1.32 to 1.38; S^0 in iron-26 per cent nickel alloys varied from 1.15 to 1.28; in iron-26 per cent nickel-0.4 per cent carbon S^0 was about 1.16. In iron-4.0 per cent phosphorus alloy, the minimum solute content measured was approximately 1.8 per cent and the weight fraction of the eutectic measured by quantitative metallography was approximately 26 weight per cent.

A new computer program was developed to analyze solute redistribution during solidification, during cooling to room temperature and/or during post-solidification heat treatments. The program simulates solidification by making a series of incremental mass balances and by computing solid diffusion by a finite difference technique. The program may be applied with facility to either eutectic, peritectic or complete solid solution type binary alloys and will account for large amounts of diffusion in the solid. In this study, computations were made for the iron-nickel and iron-phosphorus systems for both a plate-like and a cylindrical volume element, and for linear and parabolic volume growth rates.

The amount of solid diffusion during solidification, and thus microsegregation, was shown to depend for a given alloy on the parameter $\eta = \theta_f / \lambda^2$ (where λ = one-half the dendrite arm spacing and θ_f = solidification time). Extent of microsegregation in all alloys studied (as measured by the minimum composition, the segregation ratio, or the weight fraction eutectic) required the presence of solid diffusion during solidification, and, in qualitative agreement with theory, extent of microsegregation changed only slightly with distance from the chill (hence with increasing solidification time). Good quantitative agreement was obtained for the iron-nickel binary system by correcting the experimentally measured primary dendrite spacings by a factor of .127 for the Mass Balance Technique - plate model and .165 for the Mass Balance Technique - cylinder model. The correction factor for the iron-26 per cent nickel alloy for secondary arm spacings was 0.303 for the Mass Balance Technique - plate model and 0.378 for the Mass Balance Technique - cylinder model. The correction factor necessary for the iron-phosphorus alloy was 0.193 based on primary arm spacings and 0.556 based on secondary arm spacings.

Thesis Supervisor:

Merton C. Flemings

Title:

Associate Professor of Metallurgy

TABLE OF CONTENTS

<u>Chapter Number</u>		<u>Page Number</u>
	ABSTRACT	ii
	LIST OF ILLUSTRATIONS	vi
	LIST OF TABLES	xii
	ACKNOWLEDGEMENTS	xiii
I	INTRODUCTION	1
II	ANALYSIS: MICROSEGREGATION IN IRON BASED ALLOYS	5
	A. Introduction	5
	B. Classical Analysis	12
	C. Model for Solidification of Iron Based Alloys	14
	D. Diffusion in the Solid; Analytic Solution	15
	E. Diffusion in the Solid Finite Difference Solution	19
	F. 1. The Mass Balance Technique	23
	The Solidification Interval	23
	Cooling from the Nonequilibrium Solidus	27
	2. Program Features and Operations	28
	Cylindrical Geometry	28
	Element Size	30
	Cooling Curves	31
	Evaluating Microsegregation	34
	3. Computation Results	35
	G. Summary	38
III	INGOT PREPARATION	65
	A. Alloys Investigated	65
	B. Melting Molding Casting	65
IV	THERMAL MEASUREMENTS	69
	A. Introduction	69
	B. Experimental Procedure	70
	C. Results of Thermal Measurements	72
V.	MORPHOLOGY	78
	A. Introduction	78
	B. Procedure	79
	C. Observations	80

TABLE OF CONTENTS (Continued)

v

<u>Chapter Number</u>		<u>Page Number</u>
	D. Dendrite Arm Spacing Measurements	82
	E. The Power Law	84
	F. Summary	85
VI	MEASUREMENTS OF MICROSEGREGATION IN IRON BASE ALLOYS	
	A. Procedure	108
	1. Electron Microprobe Measurements	108
	2. Quantitative Metallography	111
	B. Microprobe Results and Comparison with Theory	
	1. Iron-Nickel System	111
	Segregation Ratios	111
	The Effect of Carbon on the Segregation Ratio of Iron-Nickel	114
	Composition Deviation Index	114
	2. Iron-Phosphorus System	116
VII	SUMMARY AND CONCLUSIONS	130
VIII	SUGGESTIONS FOR FURTHER WORK	134
IX	REFERENCES	135
X	APPENDIX	
	A. List of Symbols	138
	B. Dendrite Arm Spacings	142
XI	BIOGRAPHICAL NOTE	144

LIST OF ILLUSTRATIONS

<u>Figure Number</u>		<u>Page Number</u>
2-1	Iron-nickel phase diagram.	40
2-2	Iron-phosphorus phase diagram.	41
2-3	Solidification curve for iron-26 per cent nickel alloy.	42
2-4	Solid composition at the liquid-solid interface, C_S^* , versus fraction solid, f_S , for the limiting cases for an iron-26 per cent nickel alloy. Comparison of equilibrium and nonequilibrium cases.	43
2-5	Solidification curve for an iron-10 per cent nickel alloy. Comparison of equilibrium and nonequilibrium cases.	44
2-6	Solid composition at the liquid-solid interface, C_S^* , versus fraction solid, f_S , for the limiting cases for an iron-10 per cent nickel alloy. Comparison of equilibrium and nonequilibrium cases.	45
2-7	Plate growth model used for calculations.	46
2-8	Composition of the solid at the liquid-solid interface, C_S^* , as a function of the fraction solid, f_S , for equilibrium, nonequilibrium and several intermediate cases for an iron-26 per cent nickel alloy. Analytic solution.	47
2-9	Composition of the solid at the liquid-solid interface, C_S^* , as a function of the fraction solid, f_S ,	48

<u>Figure Number</u>	List of Illustrations (Continued)	<u>Page No.</u>
	for equilibrium, nonequilibrium, and three intermediate cases for an iron-26 per cent nickel alloy. Analytic solution including the solute balance correction factor.	
2-10	Flow diagram for executive computer program (MAIN) for the Mass Balance Technique.	49
2-11	Schematic diagram of the sequence of steps in the Mass Balance Technique for calculating solute redistribution in an alloy solidifying into a single solid phase of variable composition.	50
2-12	Predicted room temperature solute distributions for a 25, 50, and 100 element plate model for an iron-26 per cent nickel alloy with $n = 4 \times 10^6$ Mass Balance Technique.	51
2-13	Master cooling curve for iron-nickel alloys.	52
2-14	Predicted segregation ratios at the solidus versus n for an iron-26 per cent nickel alloy and plate model. Analytic solution finite difference method (ASFD), analytic solution finite difference method solute corrected envelope (ASFD)-(SC), Mass Balance Technique (MBT).	53
2-15	Predicted maximum and minimum solute contents as a function of n for an iron-26 per cent nickel alloy at the solidus and at room temperature. Mass Balance Technique - plate model.	54
2-16	Predicted maximum and minimum solute contents as a function of n for an iron-10 per cent nickel al-	55

<u>Figure Number</u>	List of Illustrations (Continued)	<u>Page No.</u>
	loy at the solidus and at room temperature. Mass Balance Technique - plate model.	
2-17	Distribution curves for an iron-26 per cent nickel alloy for several η values. Mass Balance Technique - plate model.	56
2-18	Predicted solidus temperature solute distribution for an iron-26 per cent nickel alloy with $\eta = 4 \times 10^6$ for different geometries and growth rates. Mass Balance Technique.	57
2-19	Predicted values of the segregation ratio at the solidus, S' , and at room temperature, S^0 , as a function of η for an iron-26 per cent nickel alloy. Mass Balance Technique - plate model.	58
2-20	Predicted values of the segregation ratio at the solidus, S' , and at room temperature, S^0 , as a function of η for an iron-10 per cent nickel alloy. Mass Balance Technique - plate and cylinder model.	59
2-21	Predicted composition deviation index at the solidus, σ_m^i , and at room temperature, σ_m^0 , versus η for an iron-26 per cent nickel alloy. Mass Balance Technique - plate model.	60
2-22	Predicted composition deviation index at the solidus, σ_m^i , and at room temperature, σ_m^0 versus η for an iron-10 per cent nickel alloy. Mass Balance Technique - plate model.	61

<u>Figure Number</u>	List of Illustrations (continued)	<u>Page No.</u>
2-23	Weight per cent eutectic versus n for an iron-3.5 per cent phosphorus alloy. Mass Balance Technique - plate model.	62
2-24	Weight per cent eutectic versus n for an iron-4.0 per cent phosphorus alloy. Mass Balance Technique - plate model.	63
2-25	Minimum solute content at room temperature, C_m^0 , for an iron-3.5 per cent phosphorus alloy. Mass Balance Technique - plate model.	64
3-1	Schematic diagram of plate mold.	67
4-1	Cooling curves from the unidirectionally solidified ingot with thermocouples at 1.13, 2.17, 3.15, 4.17, 5.36, and 6.53 inches from the chill.	74
4-2	Position of the liquidus and solidus isotherms as a function of the square root of time.	75
4-3	Square root of solidification time versus distance from the chill.	76
5-1	Schematic diagram of growth forms and their terminology.	87
5-2	Iron-10 per cent nickel alloy. Photomicrographs at 1", 2" and 4" from the chill. Casting 1, 7.6X.	88
5-3	Iron-10 per cent nickel alloy. Photomicrographs at 1", 2" and 4" from the chill. Casting 1, 34X.	89
5-4	Iron-15 per cent nickel alloy. Photomicrographs at	90

<u>Figure Number</u>	List of Illustrations (continued)	<u>Page No.</u>
	1", 2" and 4" from the chill. Casting 2, 7.6X.	
5-5	Iron-15 per cent nickel alloy. Photomicrographs at 1", 2" and 4" from the chill. Casting 2, 34X.	91
5-6	Iron-20 per cent nickel alloy. Photomicrographs at 1", 2" and 4" from the chill. Casting 3, 7.6X.	92
5-7	Iron-20 per cent nickel alloy. Photomicrographs at 1", 2" and 4" from the chill. Casting 3, 34X.	93
5-8	Iron-26 per cent nickel alloy. Photomicrographs at 1", 2" and 4" from the chill. Casting 4, 7.6X.	94
5-9	Iron-25 per cent nickel alloy. Photomicrographs at 1", 2" and 4" from the chill. Casting 4, 34X.	95
5-10	Iron-26 per cent nickel-0.12 per cent carbon alloy. Photomicrographs at 1", 2" and 4" from the chill. Casting 5, 7.6X.	96
5-11	Iron-26 per cent nickel-0.12 per cent carbon alloy. Photomicrographs at 1", 2" and 4" from the chill. Casting 5, 34X.	97
5-12	Iron-26 per cent nickel-0.33 per cent carbon alloy. Photomicrographs at 1", 2" and 4" from the chill. Casting 6, 7.6X.	98
5-13	Iron-26 per cent nickel-0.33 per cent carbon alloy. Photomicrographs at 1", 2" and 4" from the chill. Casting 6, 34X.	99
5-14	Iron-26 per cent nickel-0.42 per cent carbon alloy. Photomicrographs at 1", 2" and 4" from the	100

<u>Figure Number</u>	List of Illustrations (continued)	<u>Page No.</u>
	chill. Casting 7, 7.6X.	
5-15	Iron-26 per cent nickel-0.42 per cent carbon alloy. Photomicrographs at 1", 2" and 4" from the chill. Casting 7, 34X.	101
5-16	Iron-25 per cent copper alloy. Photomicrographs of 1", 2" and 4" from the chill. Casting 9, 64X.	102
5-17	Iron-4 per cent phosphorus alloy. Photomicrographs at 1", 2" and 4" from the chill. Casting 10, 34X.	103
5-18	Primary dendrite arm spacing versus distance from the chill for binary iron-nickel alloys containing from 10 to 26 per cent nickel.	104
5-19	Primary dendrite arm spacing versus distance from the chill for ternary iron-nickel-carbon alloys containing 26 per cent nickel and from 0 to .42 per cent carbon.	105
5-20	Secondary dendrite arm spacing versus distance from the chill for iron-nickel-carbon alloys, containing nominally 26 per cent nickel and from 0 to .42 per cent carbon.	106
5-21	Primary and secondary dendrite arm spacing versus distance from the chill for binary iron-4.0 per cent phosphorus, iron-25 per cent copper and iron-26 per cent nickel.	107
6-1	Typical cumulative composition curve. Iron-10 per cent nickel 2 inches from the chill.	119

LIST OF TABLES

<u>Table No.</u>		<u>Page No.</u>
3-1	Chemical Analyses of Ingots Studied.	68
4-1	Thermocouple locations with respect to the chill surface after solidification.	77
6-1	Electron Probe Microanalyzer Results	120
6-2	Comparison of the Correction Factors for Primary Dendrite Arm Spacings Calculated for the Iron-26 Per Cent Nickel Alloy and Iron-10 Per Cent Nickel Alloy with the Mass Balance Technique	121
6-3	Comparison of Measured and Theoretical Segregation Ratios, Iron-26 Per Cent Nickel Alloy - Mass Balance Technique - Plate Model	122
6-4	Comparison of Measured and Theoretical Segregation Ratios, Iron-10 Per Cent Nickel - Mass Balance Technique - Cylinder Model	123
6-5	The Effect of Carbon on Microsegregation in an Iron-26 Per Cent Nickel Alloy - 2 Inches from the Chill	124
6-6	Measurements of the Composition Deviation Index, σ^o and Results Predicted by the Mass Balance m Technique - Plate Model Based on Primary Dendrite Arm Spacings	125
6-7	Volume Per Cent Eutectic Measured Metallographically at Different Distances from the Chill	126
6-8	Electron Microprobe Analysis for Minimum Phosphorus Contents at Different Distances from the Chill	127
6-9	Results of Wet Chemical Analysis on the Iron Phosphorus Ingot	128
6-10	Comparison of the Weight Per Cent Eutectic Predicted by the Mass Balance Technique - Plate Model with that Measured Experimentally for the Iron-4.0 Per Cent Phosphorus Alloy.	129

ACKNOWLEDGEMENTS

The author wishes to express his gratitude particularly to the following people whose continued support and encouragement made this thesis possible:

His parents for the many sacrifices endured, their continued aid, and their enthusiasm for this endeavor.

Professor Merton C. Flemings for his inspirational talks, guidance, leadership, and patience.

Dr. Harold Brody for his originality, encouragement, and many selfless hours of collaboration on computer programming, technical problems, and manuscript preparation.

Mr. Ernest Poirier who initiated the casting work and provided some of the materials studied in this thesis.

Mr. Edwin Backman whose foundry experience was quite valuable.

Mrs. Barbara Marks for typing this thesis.

Miss Frances Gedziun for typing the rough drafts.

The members and staff of the M.I.T. Computation Center who tried their best to keep the computer going.

The members of the solidification group who provided a congenial atmosphere and several valuable suggestions on various aspects of this study.

The U.S. Army Materials Research Agency who sponsored the project.

I. INTRODUCTION

The quest for maximizing material properties consistent with process and economic feasibility is of utmost importance. Alloys, casting techniques, and homogenization procedures which endeavor to achieve the ultimate in a material's capability are perpetually sought.

Microsegregation resulting from solidification has been proven to have a pronounced effect on many phenomena including hot tearing,¹ casting fluidity,² banding in wrought materials,^{3,4} stress corrosion,⁵ mechanical properties of cast and wrought materials.^{6,7}

The microsegregation in a cast material is caused by solute partitioning and transport between and within phases both during and after solidification. Treatments of this solute partitioning for the case of plane front solidification⁸ for both equilibrium and normal nonequilibrium conditions have been devised and exploited in the crystal growing and the semiconductor field. The analysis for the equilibrium case assumes perfect diffusion in both the solid and the liquid states, and solid and liquid interface compositions given by the phase diagram. The result is the familiar lever rule:

$$C_o = f_s C_s + f_L C_L \quad (1)$$

where:

C_o = overall alloy composition in weight per cent

C_s = composition of the solid in weight per cent

f_S = weight fraction solid

C_L = composition of the liquid in weight per cent

f_L = weight fraction liquid

The classical nonequilibrium case originally derived by Scheil⁹ assumes perfect diffusion in the liquid but no diffusion in the solid and equilibrium at the liquid solid interface and results in the following expression for a constant partition ratio:

$$C_S^* = k C_O (1 - f_S)^{k-1} \quad (2)$$

where:

C_S^* = solid composition at the solid-liquid interface

k = equilibrium partition ratio

Since no diffusion in the solid is permitted, isoconcentration contours (after as well as during solidification), enclose weight fractions of solids given by equation (2), up to the limits of solid solubility. The Scheil analysis may be rewritten to yield the fraction solid as a function of temperature. The result is:

$$f_S = 1 - \left[\frac{m_L C_O}{T_m - T} \right]^{\frac{1}{1-k}} \quad (3)$$

where:

m_L = slope of the liquidus line

T_m = liquidus temperature

T = temperature

Techniques for handling microsegregation in the case where limited solid state diffusion occurs, and their application to

castings which solidify dendritically have recently been investigated by Flemings et al.^{10,11,12} In that work, microsegregation in structures solidified at different cooling rates was quantitatively measured and shown to be relatively insensitive to cooling rate. Dendrite morphology was examined and shown to be remarkably platelike.

The effect of homogenization treatments on microsegregation was also examined analytically and experimentally with good results.^{13,14} It was predicted that a low alloy steel casting solidified at a moderate rate requires at least one hour at 2500°F (or much longer at lower temperatures) to achieve significant homogenization of elements other than carbon. This was verified by microprobe analysis and its importance in practice was demonstrated in the work of Ahearn and Quigley¹⁵ who showed that a remarkable improvement in properties could be obtained from high temperature homogenization. Their experimental measurements illustrated that reduction in area is increased by up to a factor of 7 at 180,000 psi yield strength in a low alloy steel.

It is clear from the foregoing that significant microsegregation exists in cast steels, that usual homogenization treatments do not eliminate it, and that it significantly affects mechanical properties of cast alloys.

Because of the engineering importance of microsegregation in iron base alloys, this work has been undertaken to develop improved analytic and experimental techniques for quantitative

determination of the important variables influencing it. A high speed digital computer is employed to quantitatively evaluate the effect on solute redistribution of (1) solidification variables such as cooling rate and solidification time, (2) material variables as diffusivity, alloy content, and phase diagram configuration, and (3) structural variables as dendrite morphology and dendrite arm spacing. The computer technique may be applied to the solidification process, post solidification cooling or homogenization treatments. The quantities evaluated include C_M and C_m , the maximum and minimum solute contents, S , the segregation ratio, f_E , the amount of nonequilibrium eutectic, and σ_m , a parameter which indicates the deviation of solute distribution from the mean alloy content.

The technique is an extension of a previous analysis originally devised for eutectic systems using a plate-like model. The new solution offers increased versatility featuring: (1) operability on both ferrous and nonferrous solid solution and peritectic alloys as well as eutectics; (2) choice of a cylindrical or spherical solidification growth form in addition to the plate; (3) applicability to systems in which considerable diffusion takes place in the solid.

To substantiate the validity of the analysis, microsegregation predictions on both the solid solution type iron-nickel and iron-phosphorus eutectic system were compared to actual solute distributions measured by electron microprobe analysis.

II. ANALYSIS: MICROSEGREGATION IN IRON BASE ALLOYS

A. Introduction

In this section solute redistribution in iron alloys is related to the phase diagram and to the casting parameters dendrite arm spacing and solidification time. The solidification process is idealized for the analysis, by the selection of microscopic transport conditions and a growth model.

In previous work, microsegregation has been described successfully for eutectic type aluminum alloys¹⁶ using a plate-like growth geometry. In this work, the analyses have been extended to apply to an increased number of system types, e.g., solid solution alloys, and to cylindrical growth geometries as well as plate-like growth geometries.

The computer analysis of microsegregation on systems such as iron-nickel differs significantly from that of the previously studied aluminum alloys in two ways:

1. The absence of significant eutectic or other phase solidifying at a single temperature and composition at the end of freezing.
2. The presence of much greater diffusion in the solid both during and after solidification than that encountered in most aluminum alloys.

Major characteristics of the model employed are similar to those used in previous studies.^{12,17,18}

1. A characteristic volume element of simple geometry selected such that growth and transport within that volume element is representative of the rest of the two phase region. The dimensions of the volume element will be the same as the dendrite arm spacing.
2. The gradients and concentration differences are for the local areas where distances are on the order of the dendrite arm spacing.
3. Negligible undercooling prior to the nucleation of the solid phases.
4. Negligible supercooling at the solid-liquid interface due to kinetic or curvature effects.
5. Perfect diffusion in the liquid over distances the order of dendrite arm spacings.
6. The equilibrium partition ratio applies at the interface.
7. Solute conservation within a dendrite volume element; i.e., no macroscopic segregation.
8. Solidification occurs by the continuous thickening of dendrite growth forms.
9. Evolved time may be described by:

$$\theta = \left(\frac{\lambda}{\ell}\right)^h \theta_f \quad (4)$$

where h is 1 for plate, 2 for cylinder, and 3 for sphere models with a linear volumetric growth rate; or where h is 2 for a

plate, 3 for a cylinder, and 4 for a sphere with a parabolic volumetric growth rate.

The above for a plate model results in:

$$\text{Linear growth: } \lambda_i = u\theta \quad (5)$$

$$\text{Parabolic growth: } \lambda_i = \gamma \sqrt{\theta} \quad (6)$$

where u and γ are constants.

10. Temperature is uniform throughout the growth element.
11. Solute transport in the solid phases by volume diffusion which may be described by Fick's equations.
12. Liquid and solid densities are equal and constant; thus neglecting volume changes.

These assumptions have been discussed and justified by Bower, Brody, and Flemings¹² for dendritic solidification of aluminum alloys. Similar considerations for iron-base alloys are discussed further in the text.

Through application of mass balances and numerical analysis techniques, macroscopic parameters such as the solidification curve and the average composition of the phases may be computed and detailed analyses made of solute distribution within the dendrites (i.e., microsegregation).

Previously, laborious hand calculations were necessary to carry out this type of analysis for any but the simplest assump-

tions and for any alloy systems but those having a constant partition ratio. The availability of an I.B.M. 7094 digital computer made it feasible to carry out these analyses for alloy systems such as iron-nickel and iron-phosphorus to account in detail for casting parameters such as diffusion in the solid phases.*

Computations are based on the iron-nickel phase diagram¹⁹ drawn in Figure 2-1 and the iron-phosphorus diagram²⁰ drawn in Figure 2-2. These phase diagrams are compiled from the best data presently available in the literature.

Data for the diffusion coefficient used in calculations for iron-nickel alloys are from Goldstein²¹ who showed the diffusion coefficient for the phase varies with both temperature and nickel content according to the relation,**

$$D_S = \exp [0.0519 X_{Ni} + 1.15] \exp \left[- \frac{38,380 - 5.85 X_{Ni}}{T_k} \right] \quad (7)$$

where X_{Ni} = atomic per cent nickel

T_k = temperature, degrees Kelvin

*The work was carried out at the M.I.T. Computation Center, M.I.T. Cambridge, Massachusetts.

**Goldstein reports the above expression to be in agreement with his measured values of D_S within ten per cent for nickel contents up to 50 per cent in the temperature range of 1000°C to 1288°C. In the work equation (7) is employed for compositions up to 68 per cent nickel and in the temperature ranges 800°C to 1469.5°C.

Data for the diffusion coefficient used in the calculations for the iron-phosphorus system were taken from Seibel²² who lists the following expression for phosphorus diffusion in α or δ :

$$D_S = 2.90 \exp \left[- \frac{55000}{RT_k} \right] \quad (8)$$

where R = gas constant.

To evaluate the amount of microsegregation, in single phase alloys, two parameters have been defined, the segregation ratio and the composition deviation index. Both parameters are readily determined empirically by measuring concentration gradients and extremes of concentration in local areas where distances are the order of the dendrite arm spacing.

The segregation ratio is defined as

$$S = \frac{C_M}{C_m} \quad (9)$$

where C_M = maximum solute concentration in the solid dendrite

C_m = minimum solute concentration in the solid dendrite

To supplement the information given by the segregation ratio the composition deviation index, σ_m , was devised. This parameter evaluates the average deviation from the mean composition. It will distinguish between two alloys of identical S, one possessing a mildly sloping solute distribution and one which contains a very steep concentration gradient. The composition deviation

index is defined as:

$$\sigma_m = \frac{2}{C_o} \int_0^{V_f^*} |C_o - C_S| d V_f \quad (10)$$

where C_o = the average alloy solute content

C_S = the composition at any point

V_f^* = volume fraction at which C equals C_o

σ_m is normalized by dividing by the overall alloy content. This allows comparison of alloys of different composition, i.e., a 1 per cent absolute variation in a 25 per cent alloy is not considered as segregated as a 1 per cent variation in a 2 per cent alloy.

These parameters may be evaluated at any temperature; however, two cases are of special interest. These are: (1) at the solidus after solidification and prior to cooling to room temperature, and (2) at room temperature. Special symbols have been defined for these cases:

S' = segregation ratio at the solidus temperature

σ_m' = composition deviation index at the solidus temperature

S^o = segregation ratio at room temperature

σ_m^o = composition deviation index at room temperature

Both S^o and σ_m^o will usually be less than S' and σ_m' because of solid state diffusion which occurs during cooling from the solidus to room temperature.

For eutectic systems or those in which a second phase forms, the amount of nonequilibrium eutectic or amount of nonequilibrium second phase are commonly used as a measure of extent of microsegregation. Here the amount of eutectic present, f_E , is compared to the amount which would form during equilibrium solidification (that predicted by the phase diagram).

For the idealized plate morphology, the segregation parameters S , σ_m and f_E , are single valued functions of the dimensionless product $\alpha k = (D_S \theta_f / \ell^2)(k)$ where D_S is the solid diffusion coefficient, θ_f is solidification time, ℓ is one half the plate spacing, and k is the equilibrium partition ratio. For $\alpha k \ll 1$, segregation ratio is a maximum; for $\alpha k \gg 1$, compositions in the primary phases approach homogeneity. For a given alloy system, microsegregation may be considered as a function of θ_f / ℓ^2 since the expression for D_S and the phase diagram from which k is obtained are identical. This quantity occurs repeatedly and is so important that it is given the special designation η .

Thus

$$\eta = \theta_f / \ell^2 \quad (11)$$

Empirical observation of the variation of dendrite arm spacing with solidification time indicates that it may be represented by the expression:^{23,24,25}

$$\ell = \gamma \theta_f^n \quad (12)$$

where γ and n are constants. Substituting this α becomes:

$$\alpha = \frac{D_S}{\gamma^2} \theta_f^{(1-2n)} \quad (13)$$

For the special case where $n = 0.5$

$$\alpha = \frac{D_S}{\gamma^2} \quad (14)$$

Thus if the dendrite arm spacing is proportional to the square root of the solidification time microsegregation should be independent of solidification time and the segregation parameters will remain constant. Similarly microsegregation can be decreased by (1) increasing the solidification time if n is less than 0.5, (2) decreasing the solidification time if n is greater than 0.5.

B. Classical Analysis

Minimum segregation, $\alpha k \gg 1$, occurs in the ideal "equilibrium" freezing; i.e., complete diffusion occurs in both solid and liquid phases, with the interface compositions as given by the phase diagram. Consider an iron-26 per cent nickel alloy. The first solid forms at the liquidus temperature and is 19.3 weight per cent nickel; the alloy is completely solid at the equilibrium solidus (1456°C) and the solid is uniformly 26 weight per cent nickel. The solidification curve for the equilibrium case (temperature versus fraction solid) is drawn for an iron-26 per cent nickel alloy in Figure 2-3 and the

interface composition of the solid is plotted as a function of the fraction solid in Figure 2-4. Similar plots for iron-10 per cent nickel are shown in Figures 2-5 and 2-6.

For equilibrium solidification the segregation ratio is unity ($S' = 1$, $S^0 = 1$). From measurements of microsegregation in slowly cooled samples²⁵ and unidirectionally cast ingots (Chapter V, this thesis), it is known that the segregation ratio in as-cast iron-26 per cent nickel alloys differs from unity and is about 1.25.

The maximum segregation ratio, for $\alpha k \ll 1$, is calculated by the classical treatment of nonequilibrium solidification;¹⁶ i.e., complete diffusion in the liquid, no diffusion in the solid phases, and equilibrium at the interface. The solidification curves based on these assumptions are plotted in Figures 2-3 and 2-5. The interface compositions of the solid are plotted as a function of fraction solid in Figure 2-4 and 2-6. Since the classical treatment allows no solid diffusion this curve also represents the final solute distribution. The alloy is not completely solid until the temperature reaches the minimum point, 1436°C. The first solid to freeze is 19.3 per cent nickel and the last solid to freeze is 68 per cent nickel. Thus, for normal nonequilibrium solidification $S' = S^0 = 3.5$ again in poor agreement with experiment.

C. Model for Solidification of Iron Base Alloys

For iron base alloys αk is neither very large nor very small compared with 1, and diffusion in the solid must be considered in the calculation of the segregation ratio. (For example, for iron nickel alloys a typical value of αk is 0.1.)*

Other assumptions of the classical analysis, however, remain valid. Diffusion in the liquid over distances the order of dendrite spacings is essentially complete when $D_L \eta = D_L \theta_f / \lambda^2 \gg 1$, where D_L = diffusion coefficient of solute in the liquid phase. For iron base alloys such as iron-nickel a typical value of $D_L \theta_f / \lambda^2$ is 100.* The "characteristic distance"*** for diffusion from the thickening dendrite arms is about 100 times the dendrite spacing.

In dendritic solidification of alloys, temperature gradients provide a source of solute redistribution. As a result of the temperature gradient there is a composition gradient in the liquid increasing from the bulk composition at the dendrite tips to the liquid composition of the nonequilibrium solidus temperature at the root of the dendrites. Thus, there is a potential

$$*D_S = 10^{-8} \text{ cm}^2/\text{sec}; \theta_f / \lambda^2 \sim 10^7 \text{ sec}/\text{cm}^2; k \sim 0.7; D_L \sim 10^{-5} \text{ cm}^2/\text{sec}$$

***The "characteristic distance" is the distance at which the solute build-up decreases to $1/e$ of its original value.

flux of solute across the liquid plus solid "mushy" zone and into the liquid in advance of dendrite tips. It has been shown previously that such a flux can be neglected⁶ for $b \ll 1$; where b is defined:

$$b = \frac{G_L D_L}{R_t m_L} \quad (15)$$

and

G_L = temperature gradient in the liquid at the dendrite tips ($^{\circ}\text{C}/\text{cm}$)

R_t = rate of advance of the dendrite tips (cm/sec)

m_L = slope of the liquidus line ($^{\circ}\text{C}/\%$)

For iron-nickel alloys, a typical value of b is .018.*

D. Diffusion in the Solid; Analytic Solution

A simple plate-like model, as depicted in Figure 2-7 is taken for the solidification element. The growth forms are considered to be dendrite plates separated at their centers by the final (dendrite) spacing 2λ . The plates start to grow smoothly at the liquidus and each face advances a distance λ within the solidification time θ_f . Growth may be either linear (proportional to θ_f) or parabolic (proportional to $\sqrt{\theta_f}$).

 *Values used to evaluate b : $D_L = 10^{-5}$ cm²/sec; $R_t = 10^{-2}$ cm/sec;
 $m_L = 2^{\circ}\text{C}/\text{wt.}\%$; $G_L = 35^{\circ}\text{C}/\text{cm}$.

Brody²⁶ devised a solute balance for an infinitesimal increment of solidification as follows: conservation of solute within the volume element of constant weight fraction requires:

$$d(f_L C_L) + d(f_S C_S) = 0 \quad (16)$$

where

$$d(f_S C_S) = f_S dC_S + C_S df_S \quad (17)$$

if the solute increase in the solid is given by the atom transport across the liquid-solid interface, and this diffusion flux for a one-dimensional model is represented by Fick's Law as:

$$\frac{dC_S}{d\theta} = - D_S \frac{\partial C_S}{\partial \lambda_1} A \frac{1}{\rho_S} \quad (18)$$

where:

A = the liquid-solid interface area

D_S = volume diffusion constant for the solute in the solid

λ_1 = the position of the liquid-solid interface

ρ_S = the density of the solid

and the approximation made that the diffusion that does occur does not change the composition gradient in the solid at the interface significantly, then the following equation which places an upper limit on diffusion may be written as:

$$\left(\frac{dC_S}{d\lambda} \right)_{\lambda=\lambda_1} = \frac{dC_S^*}{d\lambda_1} \quad (19)$$

Allowing $A = 1/\rho_S \ell$ where ℓ = one half the dendrite arm spacing and $f_L = (1 - f_S)$ then combining expressions (16) through (19)

results in the following differential expression involving the solid interface composition C_S^* :

$$(C_L - C_S^*) df_S = (1 - f_S) dC_L + \frac{D_S}{l} \frac{d\theta}{d\lambda_1} dC_S^* \quad (20)$$

The differential expression (20) may be written for the special cases of linear and parabolic growth as follows:

$$\frac{d\lambda}{d\theta} = \text{constant}: (C_L^* - C_S^*) df_S = \alpha dC_S^* + (1 - f_S) dC_L \quad (21)$$

$$\frac{d\lambda}{d\theta} = \frac{\text{constant}}{\sqrt{\theta}}: (C_L^* - C_S^*) df_S = 2\alpha f_S dC_S^* + (1 - f_S) dC_L \quad (22)$$

where

$$\alpha = \frac{D_S \theta_f}{2} \quad (23)$$

For constant partition ratio, k , and constant diffusion coefficient, D_S , (21) and (22) may be integrated to yield:

$$\frac{d\lambda}{d\theta} = \text{constant}: C_S^* = kC_0 \left[1 - \frac{f_S^{k-1}}{1+\alpha k} \right] \quad (24)$$

$$\frac{d\lambda}{d\theta} = \frac{\text{constant}}{\sqrt{\theta}}: C_S^* = kC_0 \left[1 - (1 - 2\alpha k) f_S^{\frac{k-1}{1-2\alpha k}} \right] \quad (25)$$

In the case of a eutectic system solute diffusion during solidification decreases the amount of eutectic, and the primary eutectic phase boundary recedes into the eutectic. Brody⁽²⁶⁾ derived the following expressions for the increase in primary

phase for a system with a constant partition ratio at the eutectic temperature, T_E :

$$\frac{d\lambda}{d\theta} = \text{constant}: \quad f_S(T_E) = \alpha k \left[\frac{1 - f_S}{1 + \alpha k - f_S} \right] \quad (26)$$

$$\frac{d\lambda}{d\theta} = \frac{\text{constant}}{\sqrt{\theta}}: \quad f_S(T_E) = \alpha k \left[\frac{1 - f_S^2}{1 - (1 - 2\alpha k)f_S} \right] \quad (27)$$

In agreement with the previous presentation, equations (24) through (27) demonstrate the dependence of the extent of microsegregation on the structure sensitive property α .

The more general case of curved phase boundaries (non-constant partition ratio) and nonconstant diffusion coefficient is solved with the aid of a computer. The phase boundaries are represented by a series of straight line segments that approximate the actual phase diagram within experimental accuracy. Within any small region that the solidus and liquidus are straight lines, the solid and liquid compositions at the interface are represented by an equation of the form

$$C_S^* = AC_L + B \quad (28)$$

Now equations (24) and (25) can be successively integrated over narrow increments from the liquidus temperature to the temperature of interest using (28) to express the relation between C_L and C_S^* and using the proper value of the diffusion coefficient $D_S(T, C_S^*)$.

The differential expression (24) has been evaluated for an iron-26 per cent nickel alloy and the results are plotted for several values of the parameter n ($= \frac{\theta_f}{x^2}$) in Figure 2-8.

E. Diffusion in the Solid—The Finite Difference Method

The analytic solution predicts only the interface composition, C_s^* and does not yield a detailed description of the concentration profile within the dendrite. For example, for a given n , the results yield the value of the maximum composition at the end of freezing C_M' but does not predict the minimum C_m' .

The first technique which was employed to rectify the above deficiencies followed the analysis previously applied to aluminum alloys and is as follows. The growth element is considered to be divided into a number of equally spaced slices each $\Delta\lambda$ in thickness. Solidification is allowed to occur as the liquid solid interface progresses in steps from $\lambda = 0$ at time $\theta = 0$ to $\lambda = \lambda_1$ at time θ ; where θ is given by one of the simple growth expressions (5) or (6). After each increment of solidification diffusion is allowed to occur for a time $\Delta\theta$ in the already formed solid using Fick's Second Law.

$$\frac{dC_S}{d\theta} = \frac{\partial}{\partial \lambda} \left(D_S \frac{\partial C_S}{\partial \lambda} \right) \quad (29)$$

which is transformed by the finite difference²⁷ method to

$$C_{S,j,k} = \frac{C_{S,j+1,k-1} + C_{S,j,k-1} (M_{jk} - 2) + C_{S,j-1,k-1}}{M_{j,k}} \quad (30)$$

where

$$M = \frac{\Delta \lambda^2}{D(T, C_S) \Delta \theta} \quad (31)$$

and the subscripts j refer to steps in the λ direction and k to steps in time, and $\Delta \theta$ is the difference between the times when the interface is at λ_1 and at $\lambda_1 - \Delta \lambda$.

The finite difference approximation is most accurate for large values of M and the solution will be unstable for values of M less than two²⁵. For this reason whenever $\frac{\Delta \lambda^2}{D_S \Delta \theta}$ was less than 4, diffusion was considered to take place over $p \geq \frac{4 \Delta \lambda^2}{D_S \Delta \theta}$ time increments each Δt in length, such that $\frac{\Delta \lambda^2}{D_S \Delta t} \geq 4$ and $p \Delta t = \Delta \theta$. The solution for the incremental time period θ is then attained by repeating equation (30) over all slices j , p times.

In this first method the initial and boundary conditions during solidification when $T = T_L$, $\theta = 0$; $\lambda_1 = 0$ and $C_S(\lambda_1) = kC_0$ at $\lambda = 0$, $\frac{\partial C_S}{\partial \lambda} = 0$; $\lambda = \lambda_1$, $C_S(\lambda_1) = C_S^*$ where the values of C_S^* which form the envelope of the solution are given for a particular value of λ_1 by solution of the appropriate analytic expression (21) or (22) and for the appropriate value of n .

Such a procedure was shown to be satisfactory in nonferrous systems when αk was sufficiently small and C_M^i was fixed by an invariant transformation at the end of solidification (e.g., in eutectic formation). For ferrous alloys and specifically for the iron-nickel alloys considered here, αk is larger and the maximum solid composition is not confined to one value. For improved accuracy of results it is desirable to rewrite equation (19) introducing a factor w to compensate for the effect of diffusion on the interface composition and thus obtain a more realistic envelope. The result is:

$$\left(\frac{\partial C_S}{\partial \lambda}\right)_{\lambda=\lambda_1} = w \left(\frac{\partial C_S^*}{\partial \lambda}\right) \quad (32)$$

Note that this is identical to the previous case if w equals 1.

The procedure adopted was to combine the analytic expression and finite difference solution and then to require that solute be conserved during solidification. This was done in the following way. The differential mass balance, equation (20) is integrated assuming an arbitrary average value for w . The envelope (C_S^* versus f_S) obtained is next employed in the finite difference techniques to compute the solute distribution in the solid dendrites. The solute content of the dendrite is then computed after the solidification computation. If the solute content is different from C_0 , a new value of w is selected and the computation is repeated. New values of w are tried until one value is found that will conserve solute.

Values of w for several values of n were obtained as described above for the iron-26 per cent nickel alloy. The corrected envelopes of interface composition are drawn in Figure 2-9. Comparison with Figure 2-8 shows that these envelopes lie somewhat above the uncorrected values. When incorporated in the finite difference solution, the higher envelope gives rise to larger gradients during solidification and thus more diffusion. Minimum diffusion occurs with $w = 1$.

As the amount of solid state diffusion increases and even though w helps to extend the range of applicability, the assumption that the solute increase in the solid phase may be approximated using the change in the solid interface composition to estimate the solute flux (equation 19), grows progressively worse. The procedure becomes increasingly tedious as w is neither a constant nor an obvious function of n . Thus, for a given n , a new solute envelope must be calculated prior to applying the finite difference solution. If solute is not conserved, another w must be chosen, a new envelope calculated, and the finite difference solution repeated. This procedure usually requires several cycles when appreciable diffusion is involved. These facts suggested great value to any approach avoiding these pitfalls, and led to the Mass Balance Technique (MBT).

F. The Mass Balance Technique

The assumptions and boundary conditions for the third and final technique employed are identical to the previous computations except that the composition C_S^* at the interface ($\lambda = \lambda_1$) is independent of any other solution and is derived by making successive mass balances to determine the liquid composition after solid diffusion has taken place. The composition allowed to form in the slice at the interface is then the composition in equilibrium with the liquid. The mechanics of the computer solution are illustrated in Figure 2-11 and are described below.

The Solidification Interval:

(1) Consider the composition distribution in the solid of a plate-like dendrite to be approximated by the heavy line ($C_{S_{j,k}}$) in Figure 2-11. The composition of the liquid is calculated from the mass balance

$$C_{L_k} = \frac{C_o - \frac{1}{\ell} \sum_{j=1}^{j^*} C_{S_{j,k}} \Delta\lambda}{(1 - f_S)} \quad (33)$$

where

$$f_S = \frac{\lambda_1}{\ell} \quad (34)$$

(Note: for the first step $C_L = C_o$.)

(2) The interface is advanced a distance $\Delta\lambda$ by transformation

of an increment of solid of composition $C_{S_{k+1}}^*$ which is in equilibrium with the liquid C_{L_k} .

(3) The temperature of the volume element is determined from the phase diagram and the value of C_{L_k} .

(4) Diffusion is allowed to occur in the solid for an amount of time $\Delta\theta$ which is the time elapsed as the interface moves from λ_{i_k} to $\lambda_{i_{k+1}}$. The finite difference method (30) is used as described above: the time may be computed by a growth expression such as equations (5) and (6) or by a cooling curve that relates temperature and time. The diffusion coefficient may be re-evaluated, if necessary, for every iteration of the algorithm (30) as a function of the temperature and composition. The boundary conditions for this computation are:

$$\lambda = 0, \frac{\partial C}{\partial \lambda} = 0 ; \quad \lambda = \lambda_{i_k} \quad C_S = C_{S_k}^* \quad (35)$$

where $C_{S_k}^*$ is given as a result of the mass balance (steps 1 and 2).

(5) After diffusion has occurred for a time $\Delta\theta$ and a new composition distribution has been computed steps 1 through 4 are repeated; a new liquid composition is computed, the composition of a new solid increment and the temperature are found from the phase diagram and diffusion is again allowed to occur. The above procedure is repeated until the alloy

is all solid or until a eutectic composition is reached in the liquid.

(6a) Eutectic Systems: During solidification of an alloy in a eutectic system, if the liquid composition reaches the eutectic composition at a time θ_E , diffusion is computed in the primary phase at the eutectic temperature until solidification is completed, i.e., $\Delta\theta = \theta_f - \theta_E$. As a result of diffusion of solute into the primary phase, some eutectic must disappear; and this shift in the primary phase-eutectic interface is monitored throughout the calculation. The following boundary conditions are used in the computation from time θ_E to θ_f :

$$\lambda = 0, \frac{\partial C}{\partial \lambda} = 0 ; \quad \lambda = \lambda_E, C_S^* = C_S(\text{maximum solubility}) \quad (36)$$

where λ_E represents the distance to the eutectic interface.

In the special case that the last increment of solidification is reached (i.e., $\lambda_1 = l - \Delta\lambda$) and the liquid composition is less than the eutectic composition and greater than the maximum solubility limit some eutectic is considered to have formed and the amount is given by

$$f_E = \frac{C_L - C_S(\text{maximum solubility})}{C_E - C_S(\text{maximum solubility})} \left(\frac{\Delta\lambda}{l} \right) \quad (37)$$

where

f_E = weight fraction eutectic

C_E = composition of the eutectic at the eutectic temperature

C_S (maximum solubility) = composition of the primary phase at
the eutectic temperature

In the above two cases the nonequilibrium solidus temperature is considered to be the eutectic temperature.

In the case that the last increment of solidification is reached and the liquid composition is less than the maximum solubility limit, the computation is handled in the same manner as a single phase alloy.

(6b) Single Phase Alloys: Since the compositions gradients near the end of solidification are usually steep, the average composition of the last increment to freeze may not be a good indication of the nonequilibrium solidus temperature. It is often desirable to look at the last slice to freeze in more detail (and in the time sharing version of this program the decision is left to the human operator). When desirable, the last increment to freeze is divided into smaller slices and the composition distribution within that increment calculated in greater detail. The last increment is broken into one fifth the number of slices that were used in the original computation and the analysis repeated for the new C_0 , ℓ , and Θ_f . The factor of 0.2 was found to be adequate to describe the final solidification and the computer time reasonable. By

reducing ℓ and θ_f , the n is increased and for this reason the process of breaking up the final increment does not result in an ever higher final C_S if continued for several cycles. This is because as n increases, equilibrium is approached and thus a concentration gradient in the final solid becomes increasingly difficult to maintain. For example, if 100 spaces are chosen, then the final increment or 1 per cent of the material will be broken up into 20 parts each part equal to .05 per cent of the original material and the new solidification time will be .01 of the original. The effective n for the last space will be smaller by two orders of magnitude. The composition of the last solid to freeze in this final calculation is then used to define the nonequilibrium solidus temperature.

Cooling from the Nonequilibrium Solidus:

Following the completion of solidification, the change in solute redistribution that occurs on cooling from the nonequilibrium solidus to room temperature may be computed using the finite difference technique. The cooling rate relation may be input to the computer from hypothetical or empirical tabular data or in the form of an expression. The cooling rate relation defines the time for diffusion within each temperature interval and the diffusion coefficient is calculated on the basis of the average temperature within the temperature interval. The amount of diffusion is computed by evaluation of the

algorithm (30) at each slice j within each temperature interval and the size of the temperature interval is chosen to keep M greater than 4. The initial condition is the solute distribution at the solidus temperature. The boundary conditions for a single phase alloy are

$$\lambda = 0; \frac{\partial C}{\partial \lambda} = 0; \lambda = \ell, \frac{\partial C}{\partial \lambda} = 0 \quad (38)$$

and for a eutectic alloy

$$\lambda = 0; \frac{\partial C}{\partial \lambda} = 0; \lambda = \ell(1 - f_E), C_S^* = C_S(\text{max. solubility}) \quad (39)$$

Computations are continued until room temperature is reached or until the effect of diffusion on microsegregation becomes negligible.

2. Program Operation and Features

A schematic diagram of the executive program (MAIN) used for the calculations is given in Figure 2-10. This describes the major roll played by the subroutines which comprise the program.

Cylindrical Geometry:

In some cases a cylindrical volume element may be of more interest than a plate-like volume element. In such a case the axis of the cylinder is considered to coincide with the dendrite spine and the liquid solid interface advances from the axis at

time $\theta = 0$ to a radius of ℓ at time θ_f , where ℓ is one half the dendrite arm spacing and θ_f is the solidification time. The rate of advance of the interface may be given by a linear volume growth rate or a parabolic volume growth rate:

$$\frac{dV}{d\theta} = \text{constant}: \quad r_1 = u \sqrt{\theta} \quad (40)$$

$$\frac{dV}{d\theta} = \frac{\text{constant}}{\sqrt{\theta}}: \quad r_1 = a \sqrt[4]{\theta} \quad (41)$$

where r_1 denotes the position along the radius of the solid-liquid interface and u and a are constants. In addition, as with the plate-like model, the position of the interface may be calculated from a cooling curve. In cylindrical coordinates Fick's Second Law is written

$$\frac{\partial C}{\partial \theta} = D \left(\frac{\partial^2 C}{\partial r^2} + \frac{1}{r} \frac{\partial C}{\partial r} \right) \quad (42)$$

which is transformed by the finite difference method

$$C_{j,k} = \frac{(1 + \frac{0.5}{j-1}) C_{j+1} + (M-2)C_j + (1 - \frac{0.5}{j-1})C_{j-1}}{M} \quad (43)$$

The mechanics of the solution are the same as that used for the plate-like model except, now, equal slices are taken along the radius, the algorithm (43) is used to evaluate diffusion in the solid and the rate of advance of the interface is given by expressions such as (40) or (41).

Results of the computation may be expressed by the computer

program as: The solute distribution and fraction eutectic at any time during solidification or on cooling to room temperature, as an instantaneous value of the segregation ratio, the maximum and minimum composition in the solid, and/or the fraction solid, or as the nonequilibrium solidus temperature. Operation and special features of the program are discussed in section II-2 and some results for iron-nickel and iron-phosphorus alloys are presented in section II-3.

Element Size:

The finite difference numerical analysis technique involves approximating a continuous function by a series of element steps. Mathematical operations such as equation (40) and (41) are applied to adjacent steps to predict variations of a step with time. The error involved in this approximation is dependent on both element size and curve shape including the steepness of the gradients in the curve being evaluated. Too many steps lead to superfluous numerical computation while too few yield a poor approximation. The effect of element number on the Mass Balance Technique was investigated by applying the program to an iron-26 per cent nickel alloy for a 25, 50, and 100 element plate model for a dendrite arm spacing and solidification time close to nonequilibrium ($n = 4 \times 10^6$). The greatest deviations would be anticipated in this region, for as equilibrium is approached, the gradients decrease and the effect of element size becomes minimal. A plot of the solute distribution for

the 25, 50, and 100 element plate model is shown in Figure 2-12. Good agreement between the three results is evident. This information coupled with the computer time requirement of each lead to dividing the unit volumes used in this analysis into 50 divisions.

Cooling Curves:

Since diffusion can be described in terms of n values it is convenient to choose a one second solidification time and to vary the dendrite arm spacing in order to get the microsegregation parameters in terms of n . If actual cooling curves are to be used, this procedure necessitates the re-adjustment of the data to produce a meaningful result. The previous analysis by Brody¹⁶ in the aluminum-copper system did this for both linear and parabolic growth assuming a continuous rate of heat extraction, by equating the rate of heat extraction in cooling from the solidus, i.e., specific heat, to the rate of heat extraction over the solidification range, i.e., the specific heat plus the heat of fusion:

$$\text{Linear: } \lambda = u\theta \quad T = T'_S - \frac{H'}{C_{p_s}} \left(\frac{\theta - \theta_f}{\theta_f} \right) \quad (44)$$

$$\text{Parabolic: } \lambda = a \sqrt{\theta} \quad T = T'_S - \frac{H'}{C_{p_s}} \left(\frac{\sqrt{\theta} - \sqrt{\theta_f}}{\sqrt{\theta_f}} \right) \quad (45)$$

where:

H' = heat released during solidification

C_{p_s} = specific heat of solid

T'_S = nonequilibrium solidus temperature

To evaluate the cooling rates for various value of n , the six thermocouple measurements taken at various distances from the chill in an iron-26 per cent nickel alloy and described in Chapter IV were plotted in a special way. First, the solidification range was taken to be 25°C . The time to drop 25°C was measured from each cooling curve and the six values defined as the solidification times, θ_f . Temperature readings were then taken from each curve at multiples of its own θ_f and plotted. The resulting curves overlapped and deviated less than $\pm 15^\circ\text{C}$ down to 1150°C and approximately $18 \theta_f$. Three overlapped $\pm 10^\circ\text{C}$ all the way down to 1000°C . This allowed the master curve of temperature versus θ_f to be made which ranges from 1469.5 to 1000°C and is shown in Figure 2-13. These values were then used for all n 's in the iron-nickel system as follows:

- (1) The temperature of the zero time point of the master curve and the liquidus point for the alloy were made to coincide by shifting the master curve.
- (2) The solidification temperature range for a given n is taken from the computer solution after solidification has occurred and a solidification time is obtained from the liquidus and solidus temperature, and the cooling curve. The solidification time is then compared with the assigned value, i.e., 1 second

and the remaining times in the solidification curve adjusted by this factor.

(3) In the iron-phosphorus system cooling rates of 200°C/sec and 800°C/sec were used in conjunction with a 1 second solidification time.

Aside from the reduced computer time, optional geometry, solidification paths, and cooling curves which are possible with the new program, the following refinements are noteworthy:

(1) Increased accuracy - if p is greater than 1 during solidification the temperature interval between the new and the old time is calculated and the temperature is incremented by

$$T = \frac{T_k - T_{k+1}}{p} \quad (46)$$

where k refers to incremental steps in time.

(2) A punch option to produce cards containing solute distribution information which may be used as input data for plotter, computer display or further processing.

(3) Added run flexibility - any number of systems, compositions and/or dendrite arm spacings and solidification times within a system may be run in sequence.

(4) Output flexibility - choice of the time intervals throughout solidification at which the solute distribution may be viewed. Variable output frequency during any post solidification heat treatment.

- (5) Provisions for insertion of schemes to account for shrinkage during solidification.

Evaluating Microsegregation:

The computer program is written to evaluate the critical microsegregation parameters as follows:

- (1) Segregation ratio: The ratio of the maximum composition to the minimum composition is calculated and its output frequency is optional and may vary from once after each solidification step to only once after solidification is complete. This may also be calculated for each $\Delta\theta$ in cooling to room temperature or only once after the cooling from the solidus is complete.
- (2) The composition deviation index: Equation (10) is evaluated for the solute distribution at the end of solidification and after cooling is complete. The form of equation (10) is possible because solute is conserved throughout the analysis, hence, in a plot of composition versus volume fraction having that composition the areas enclosed by the distribution curves and C_0 must be equal. The advantage in taking twice the area below the curve is that the calculated value for C_M which is partially dependent on element size is eliminated from the solution.
- (3) Fraction eutectic: Eutectic formation is monitored as previously described and output frequency is optional, rang-

ing from once at the end of solidification and once at the end of the program, to once at the solidus and once after each iteration while cooling from the solidus.

3. Computation Results

Solid Solution Alloys - Iron-Nickel.

In order to compare the results of the three techniques, the predicted segregation ratios at the solidus, S' were computed and the results plotted as a function of n for an iron-26 per cent nickel alloy for a plate model and the ASFD with and without the provision of solute conservation and for the MBT in Figure 2-14. Although the resulting curves are of similar shape, the predicted n from the MBT is lower at the solidus for a given segregation ratio compared to either of the ASFD results.

The ASFD solution - uncorrected envelope predicts values closest to the MBT but lacks the important feature of solute conservation. This deficiency is most prominent for very slow solute redistribution involving a great number of numerical iterations. The difference at the solidus is due entirely to the analysis technique. In cooling from the solidus for identical cooling curves any differences between the analyses observed at room temperature are caused by the residual differences which originated in the solidification range. This

is because identical numerical analysis technique is used from the solidus in all three methods.

The results for C_M^i , C_m^i , C_M^o and C_m^o as a function of n predicted by the MBT plate model are plotted in Figures 2-15 for an iron-26 per cent nickel alloy and 2-16 for an iron-10 per cent nickel alloy. The C_M values vary much more than those of C_m . The reason for this is found in the distribution curves examples of which are plotted for several values of n in Figure 2-17, which show that the steepest gradients form at the end of solidification in the region of maximum solute. Thus greater solute transport occurs in these regions. The minimum areas all have relatively flat composition gradients and thus minimum diffusion potential.

Geometry - To evaluate the effect of geometry while negating any element size effect, a 25 element plate was compared to a 50 element cylinder as the size of the final elements are of essentially equal fractional volumes. The result shows that more diffusion does occur in the cylinder predicting a lower maximum solute content, C_M , i.e., for an iron-26 per cent nickel alloy with $n = 4 \times 10^6$, $C_M^i = 48.4$ for a 25 element plate, $C_M^i = 39.5$ for a 50 element cylinder. This geometric difference is decreased while cooling to room temperature because of the higher gradient at the end of solidification established in the plate. Thus at room temperature the total difference between the cylinder and the plate is less than 3.0

per cent nickel for $\eta = 4 \times 10^6$. A plot of the predicted solute distribution at the solidus temperature for a 50 element plate and a 50 element cylinder experiencing linear growth versus the fractional distance along a dendrite arm, λ/ℓ is shown in Figure 2-18 for $\eta = 4 \times 10^6$. The areas enclosed by the distribution curve and C_0 above and below C_0 do not appear equal in the case of the cylinder because fractional volume is proportional to r^2 rather than r .

Plots of the segregation ratio as a function of η calculated by the Mass Balance Technique for both plate and cylinder models are plotted for an iron-26 per cent nickel alloy in Figure 2-19 and for an iron-10 per cent nickel alloy in Figure 2-20. Corresponding segregation deviation parameters from these analyses are plotted in Figures 2-21 for iron-26 per cent nickel and 2-22 for an iron-10 per cent nickel alloy. These parameters will be discussed and compared to experimentally measured microsegregation in Chapter 6.

Growth Rate - Calculations for an iron-26 per cent nickel alloy with $\eta = 4 \times 10^6$ were made for a parabolic growth rate and the solute distribution at the solidus included in Figure 2-17. The reduced maximum solute content compared to the linear case occurs because more time is taken to solidify the final elements in parabolic growth. This means more diffusion time when gradients are more fully developed and results in more solute lost from the liquid, and thus a lower C_s^* . The

effect of growth rate is negligible after cooling to room temperature. The predicted difference for the above case is only 0.1 per cent.

Eutectic Alloys - Iron-Phosphorus - The results of the Mass Balance Technique - Plate model calculations of weight percentage eutectic for iron-3.5 and 4.0 per cent alloys as a function of η are plotted in Figure 2-23 and 2-24 respectively. C_m^0 is plotted as a function of η in Figure 2-25 for both the 3.5 and 4.0 per cent phosphorus alloys. These show that f_E decreases and C_m^0 increases as either the solidification time θ_f increases and/or the dendrite arm spacing decreases.

Summary

A computer solution for solute distribution was devised for the case of solidification and post solidification thermal treatment. The analysis known as the Mass Balance Technique is an extension of previous work to include cylindrical geometry and solid solution alloys as well as eutectic systems. The Mass Balance Technique is similar to the Analytic Solution Finite Difference method in that it requires the interface composition for each increment solidified. This quantity is now a dynamic calculation based on solute distribution just prior to the incremental freezing and eliminates the approximation that the chemical gradient in the solid at

the liquid-solid interface is unaffected by solid state diffusion. This permits using the MBT program in system which undergo considerable diffusion.

Resulting segregation ratios predicted by the MBT are lower than those obtained by the ASFD method. MBT calculations also predict less segregation for a cylindrical model than for a plate. A qualitative synopsis of the quantitative predictions by the Mass Balance Technique is:

Increasing n will result in the following:

Solid solution alloys or eutectic alloys in which eutectic is absent:

Decrease: S' , S° , C_M^i , C_M° , σ_M^i , σ_M°

Increase: C_m^i , C_m° , T_S^i

Eutectic Alloys in which eutectic is present:

Decrease: f_E , S' , S°

Increase: C_m^i , C_m°

The qualitative and quantitative results from both the MBT and ASFD are compared to actual experimental measurements in Chapter VI.

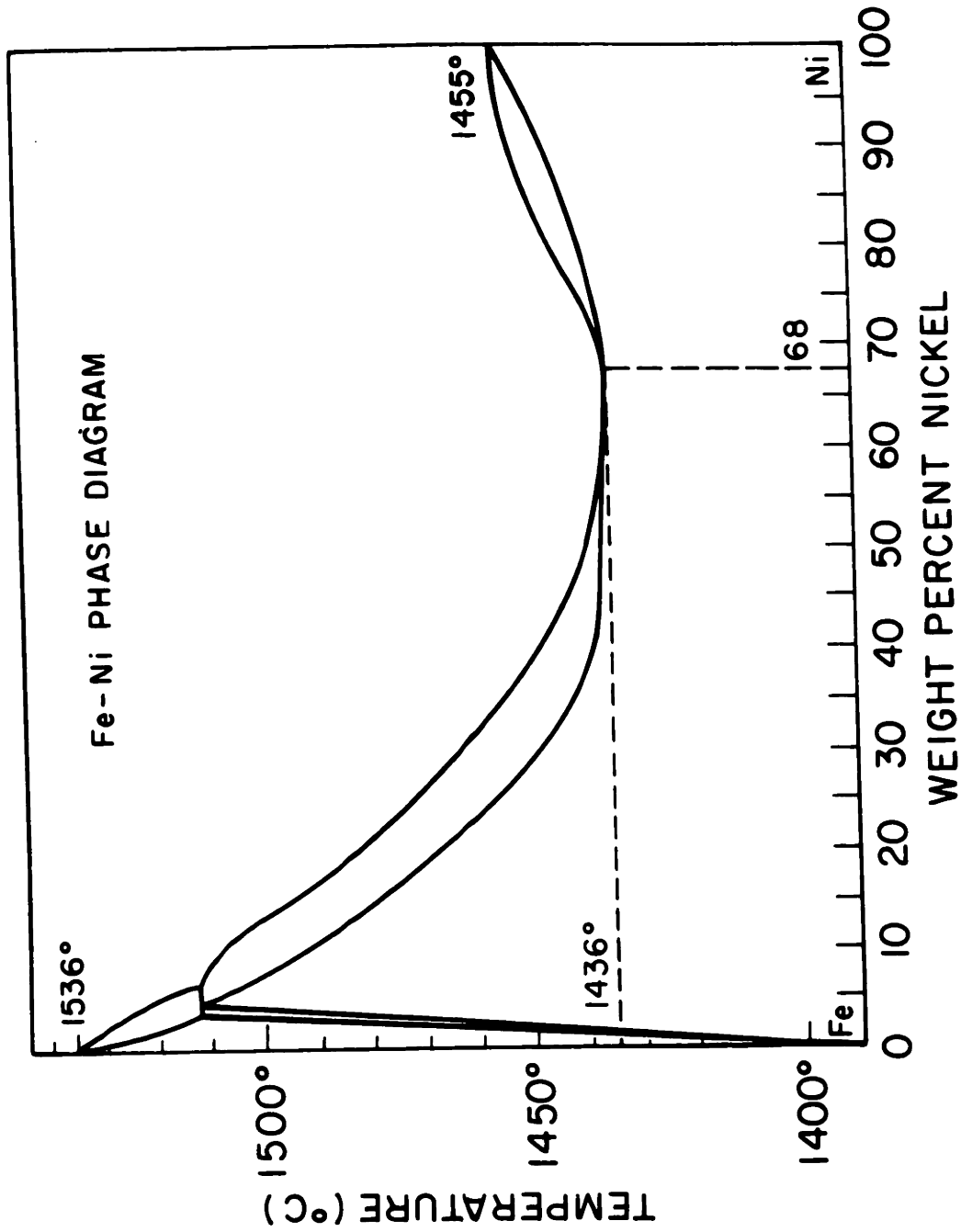


Figure 2-1. Iron-nickel phase diagram.

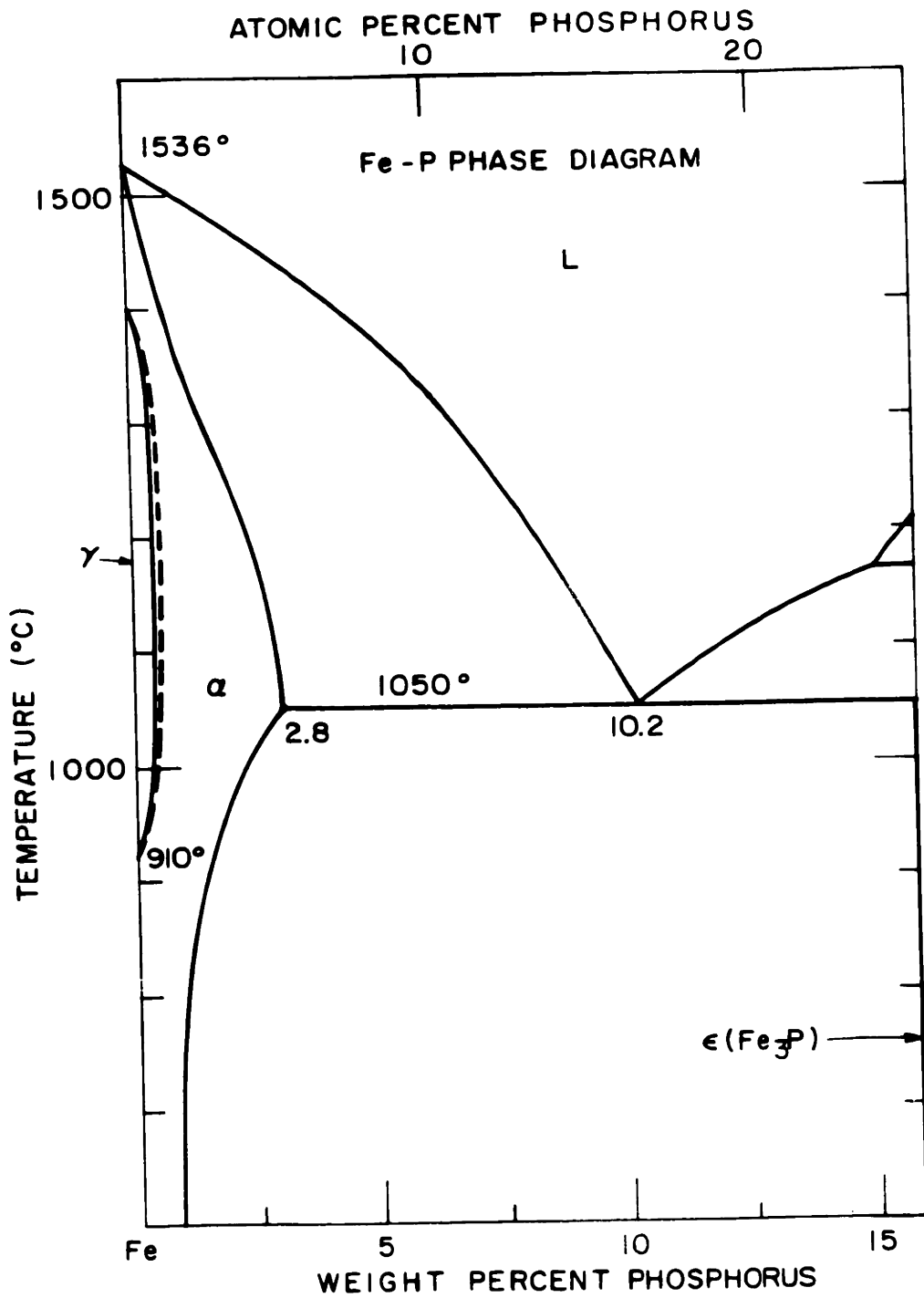


Figure 2-2. Iron-phosphorus phase diagram.

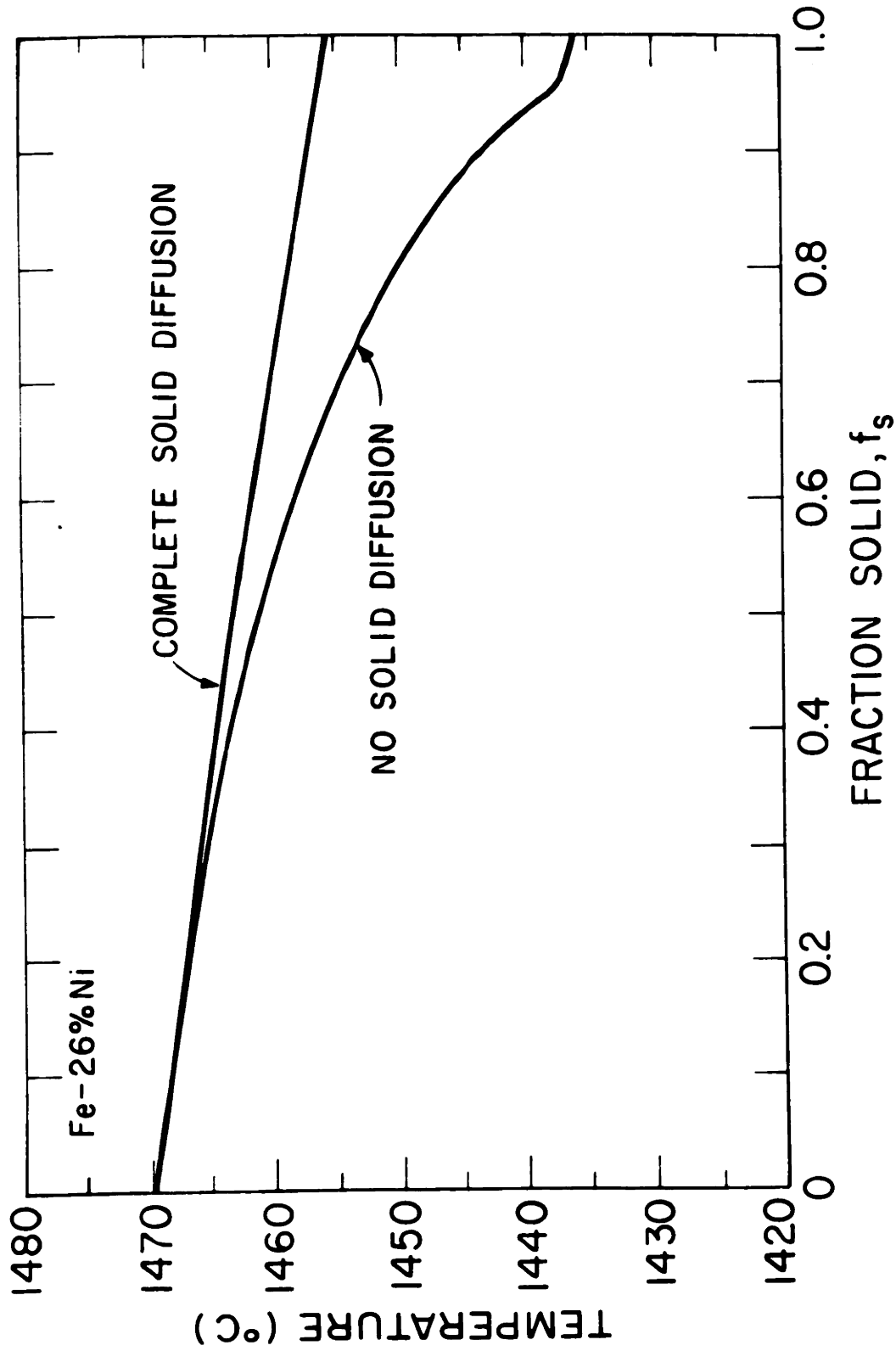


Figure 2-3. Solidification curve for iron-26 per cent nickel alloy. Comparison of equilibrium and nonequilibrium cases.

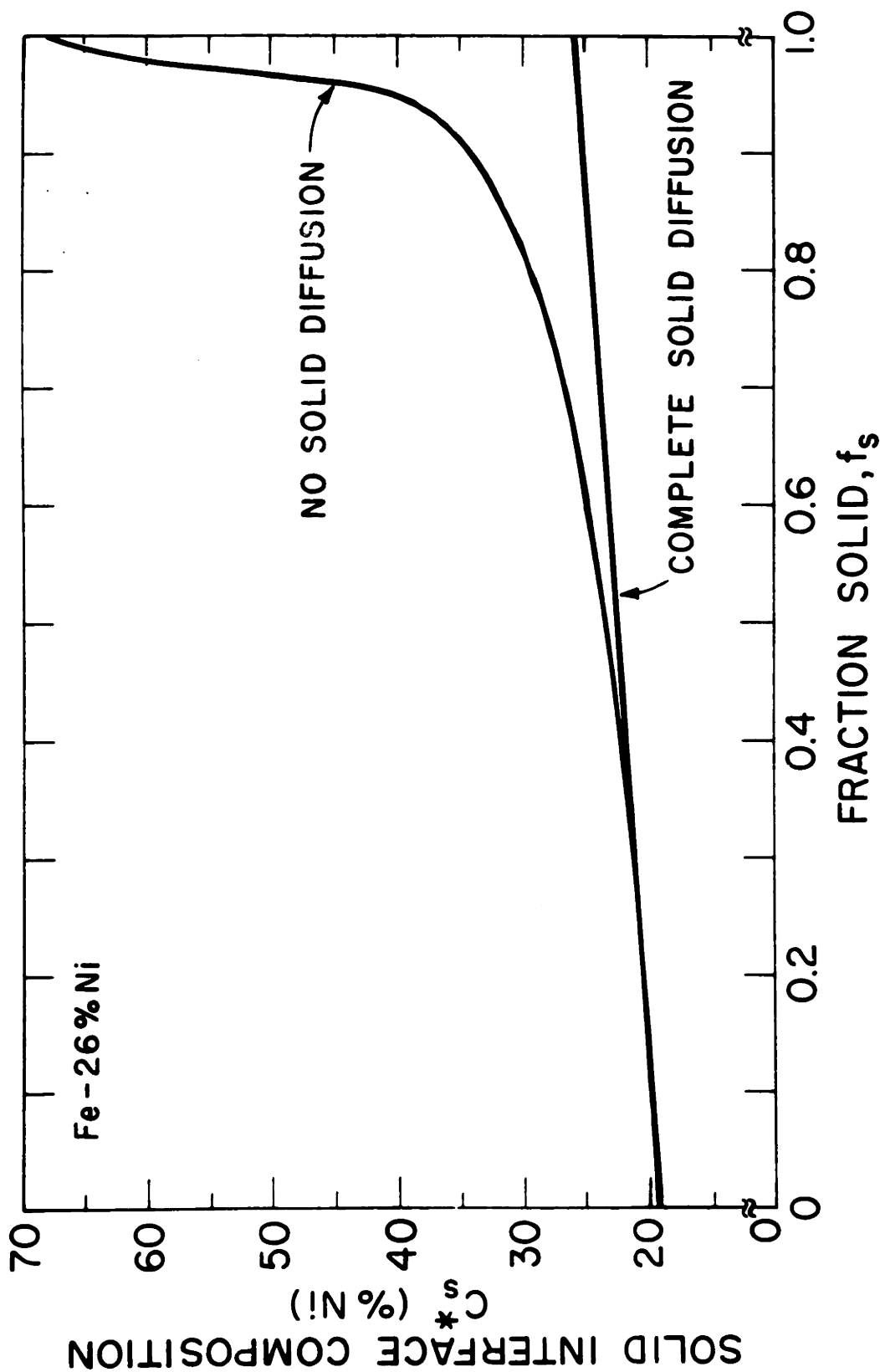


Figure 2-4. Solid composition at the liquid-solid interface, C_s^* , versus fraction solid, f_s , for the limiting cases for an iron-26 per cent nickel alloy. Comparison of equilibrium and nonequilibrium cases.

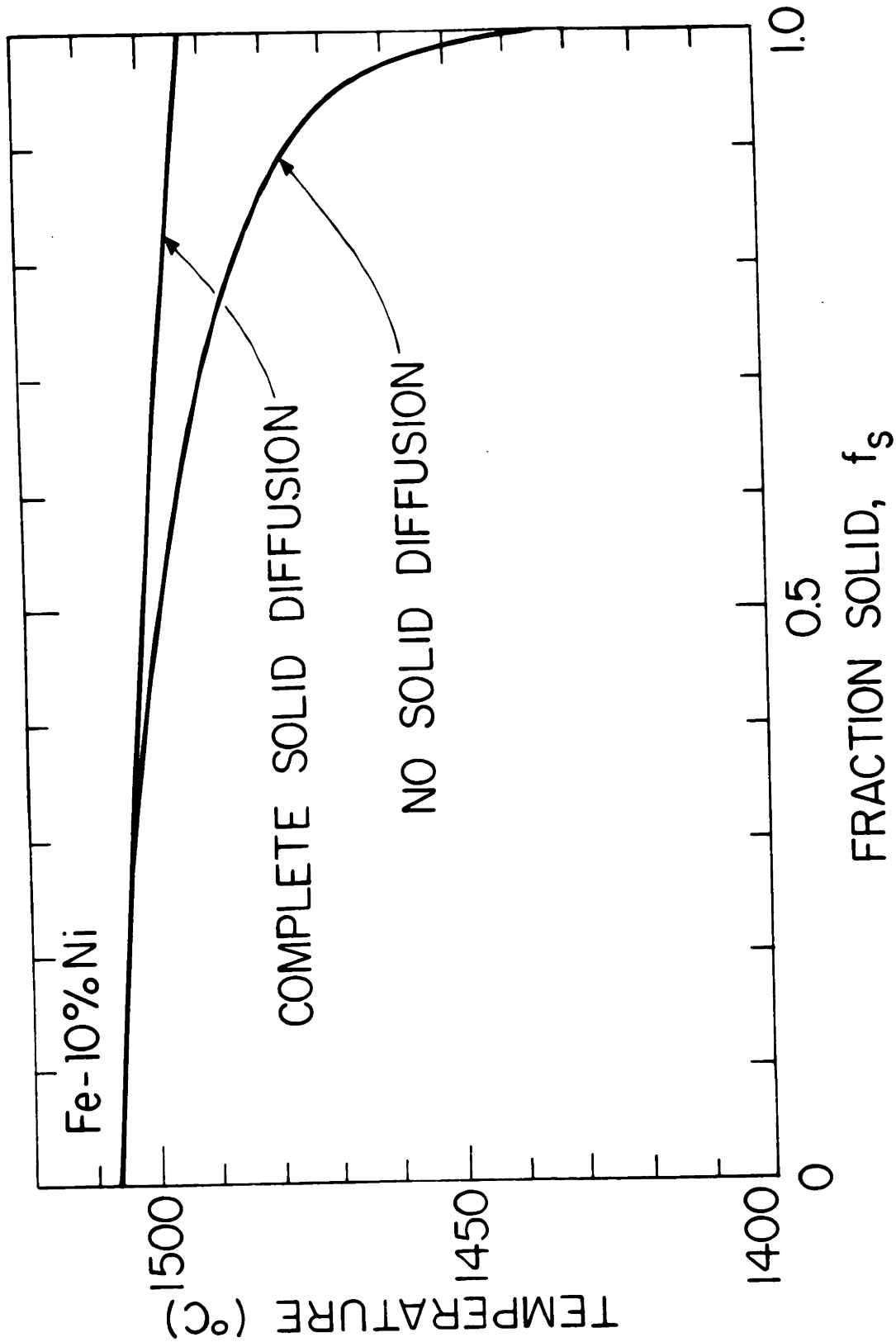


Figure 2-5. Solidification curve for an iron-10 per cent nickel alloy. Comparison of equilibrium and nonequilibrium cases.

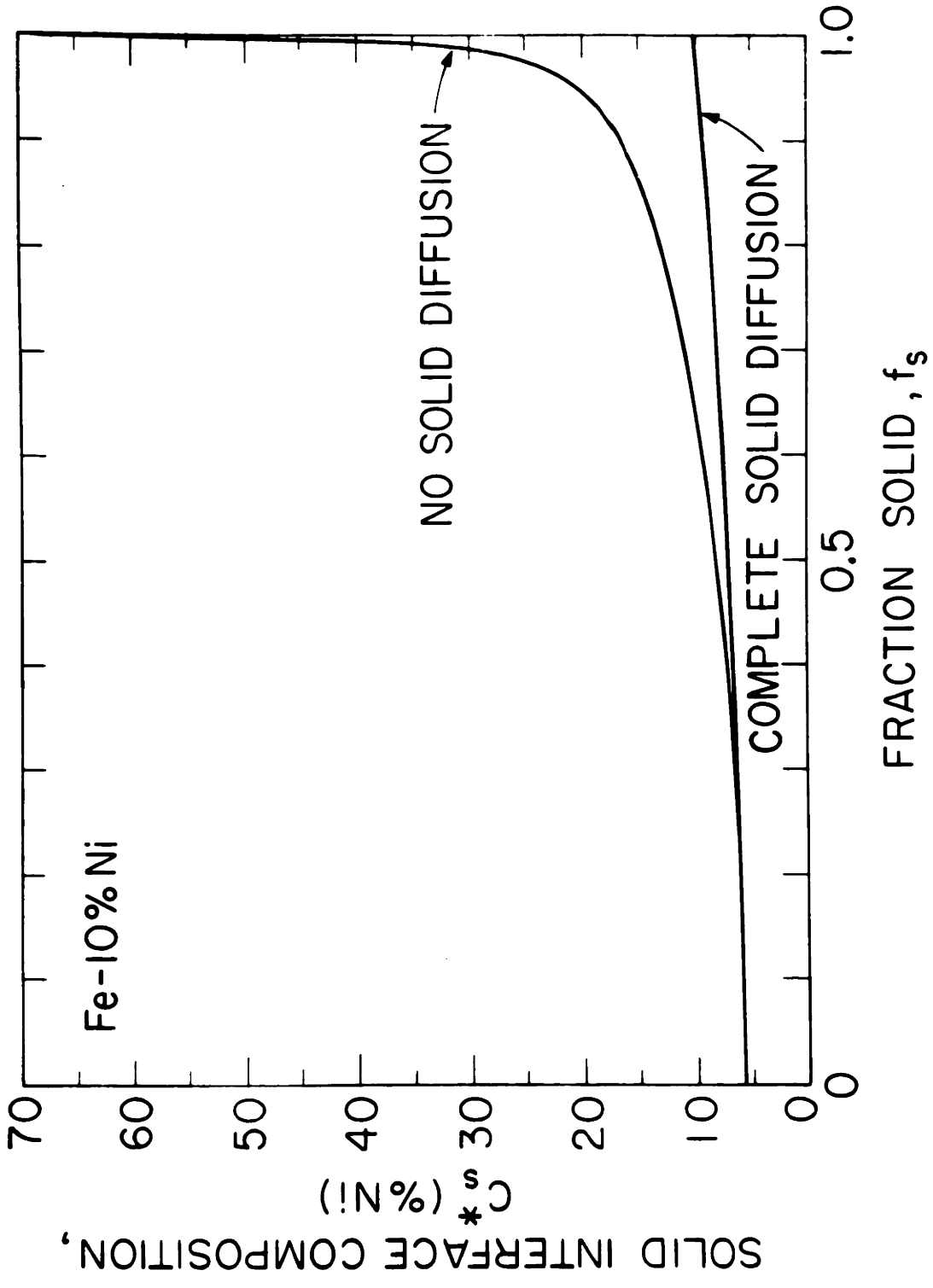


Figure 2-6. Solid composition at the liquid-solid interface, C_s^* , versus fraction solid, f_s , for the limiting cases for an iron-10 per cent nickel alloy. Comparison of equilibrium and nonequilibrium cases.

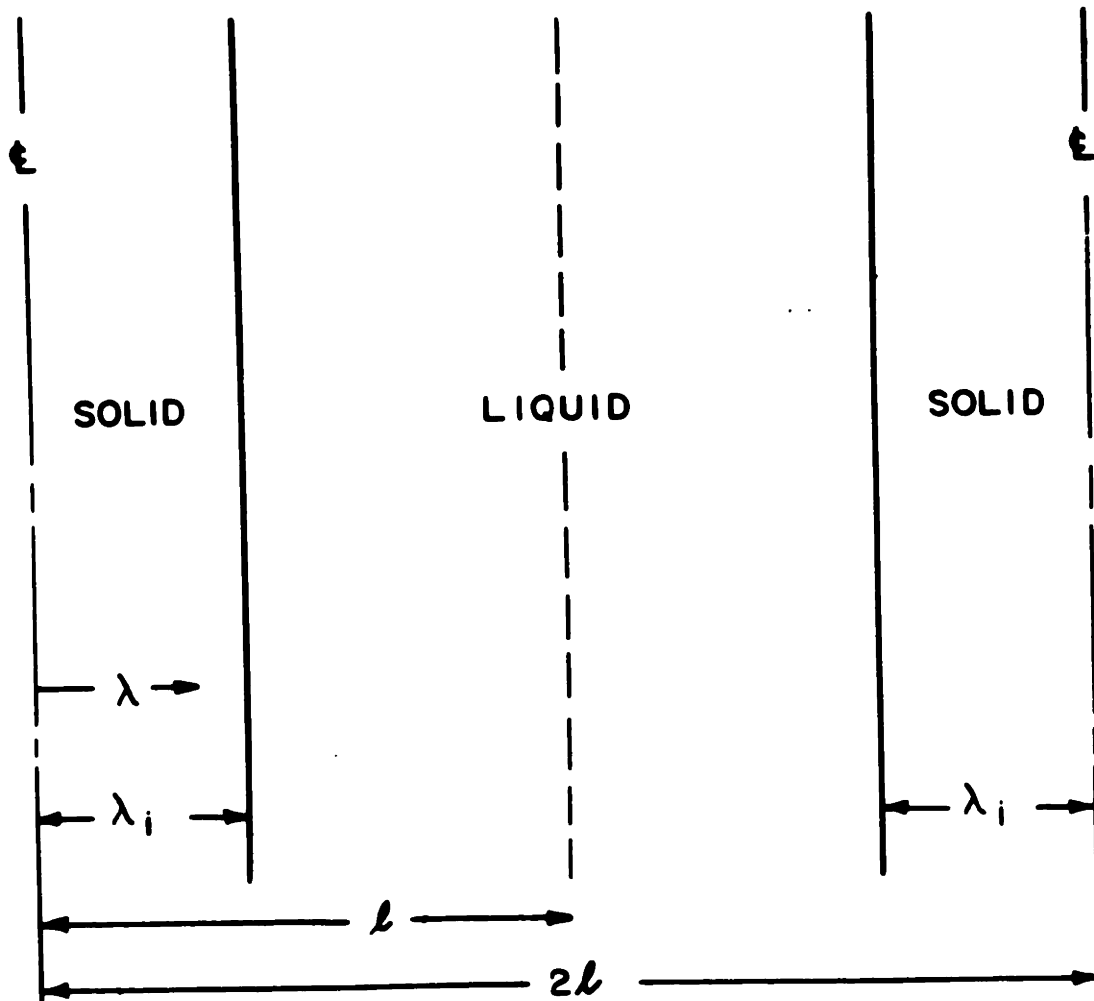


Figure 2-7. Plate growth model used for calculations.

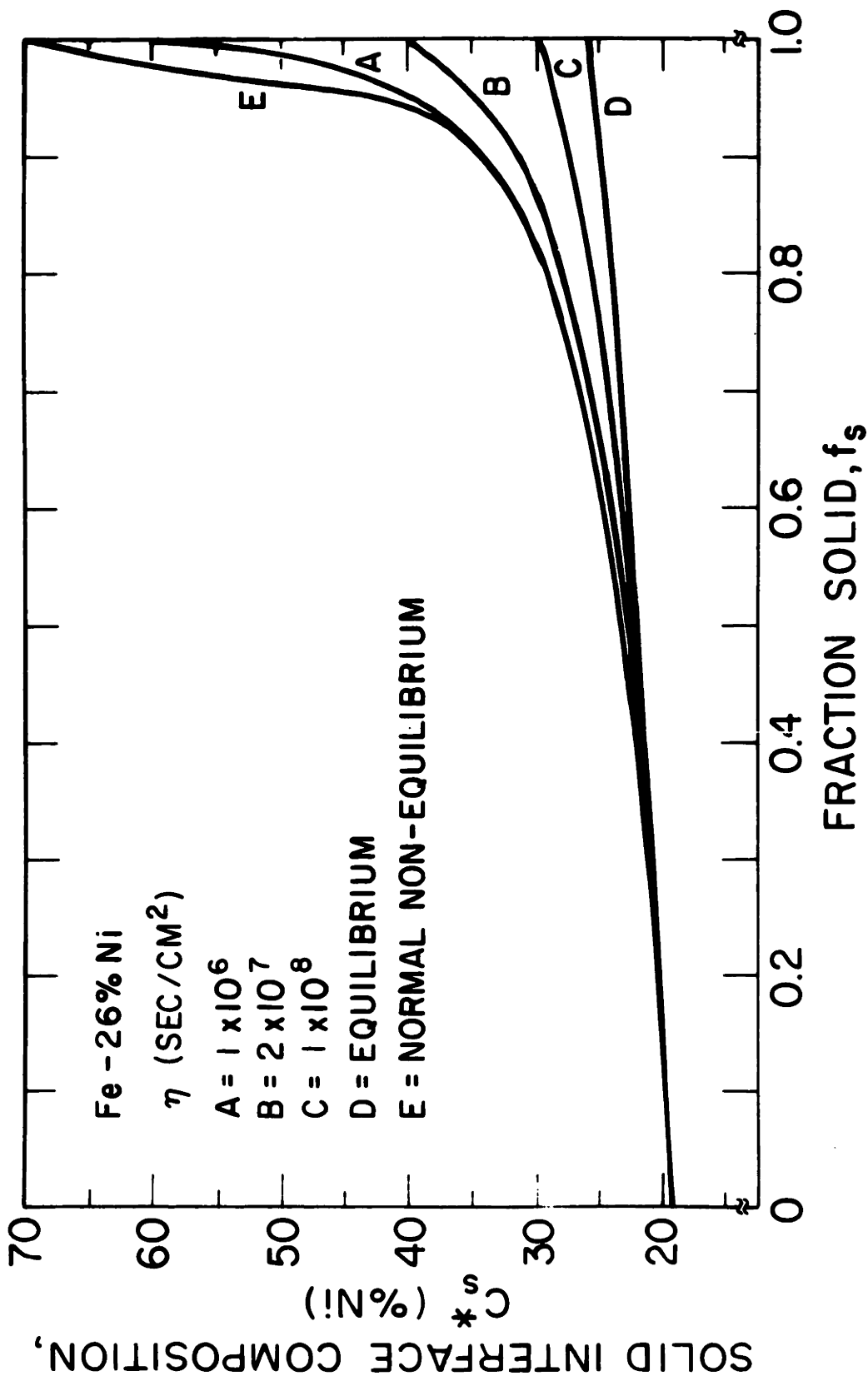


Figure 2-8. Composition of the solid at the liquid-solid interface, C_s^* , as a function of the fraction solid, f_s , for equilibrium, nonequilibrium and several intermediate cases for an iron-26 per cent nickel alloy. Analytic solution.

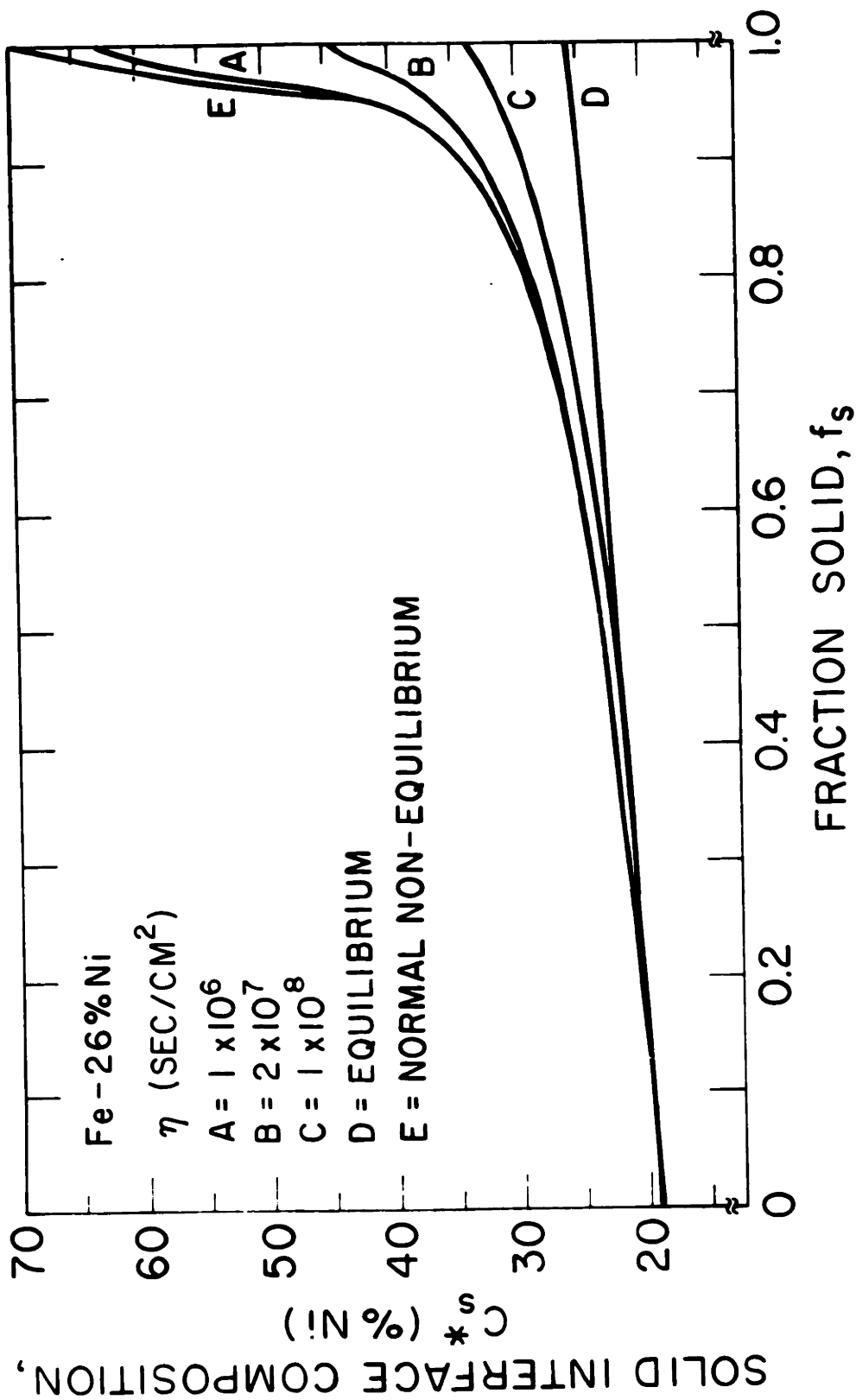


Figure 2-5. Comparison of the solid at the liquid-solid interface, C_s^* , as a function of the fraction solid, f_s , for equilibrium, nonequilibrium, and three-intermediate cases for an iron-26 per cent nickel alloy. Analytic solution including the solute balance correction factor.

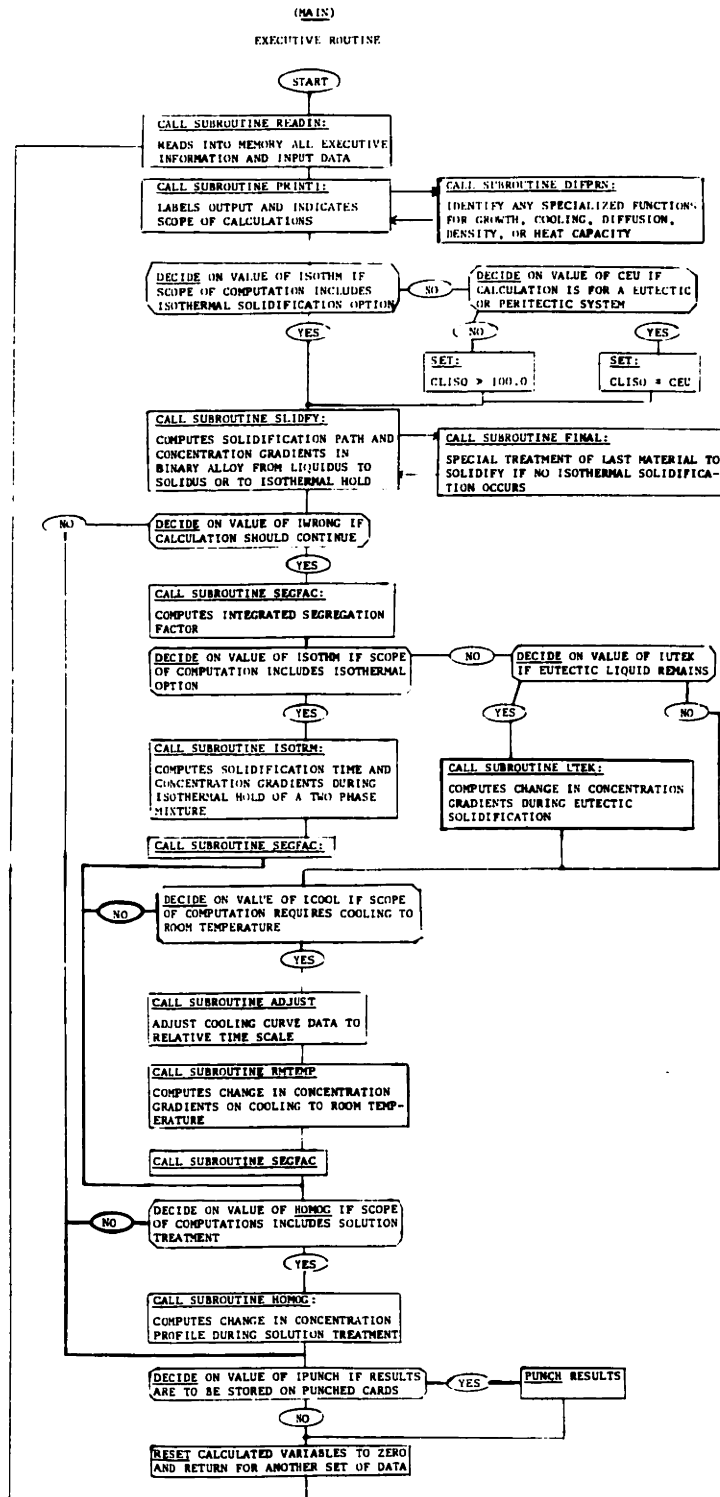


Figure 2-10. Flow diagram for executive computer program (MAIN) for the Mass Balance Technique.

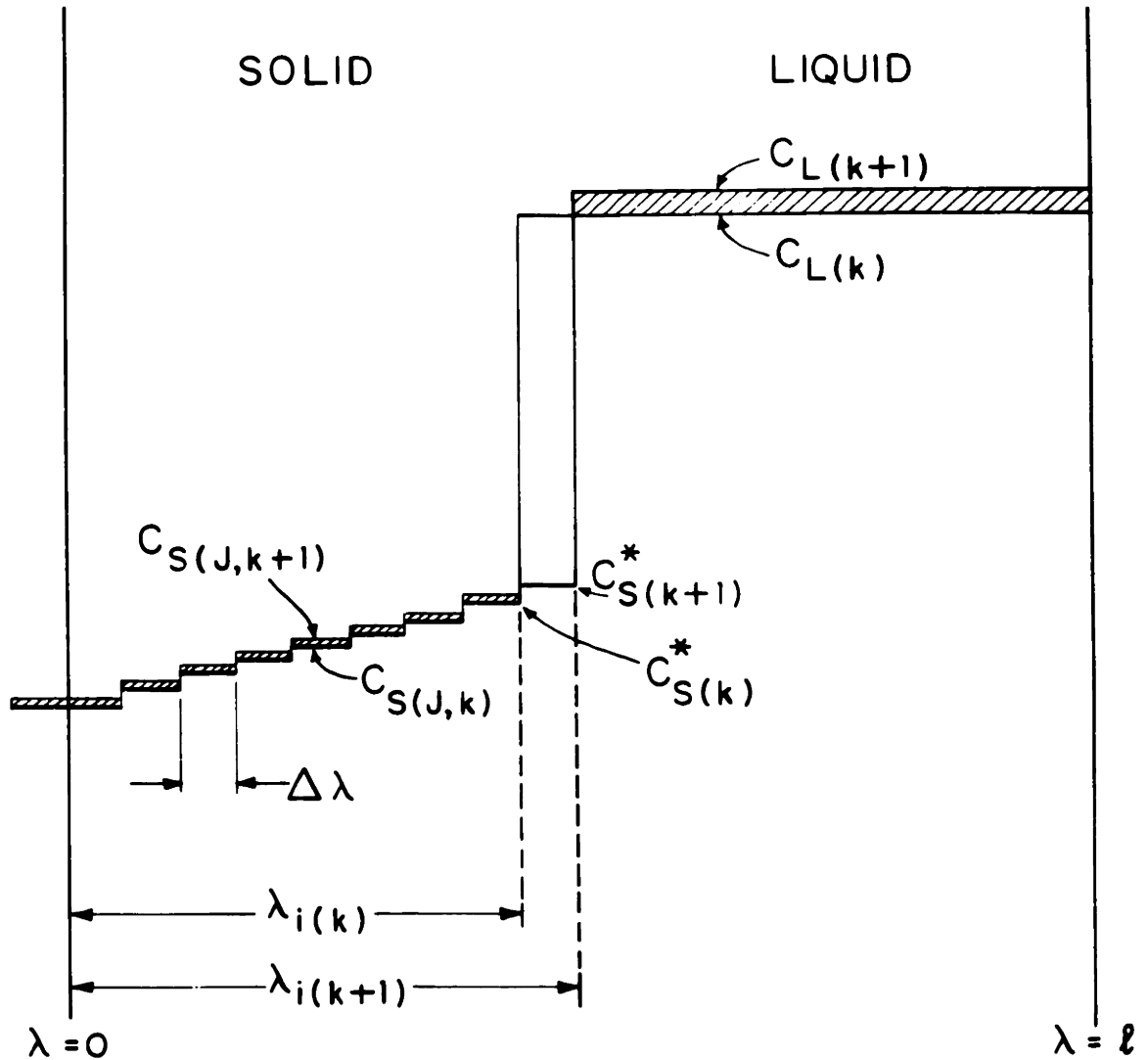


Figure 2-11. Schematic diagram of the sequence of steps in the Mass Balance Technique for calculating solute redistribution in an alloy solidifying into a single solid phase of variable composition.

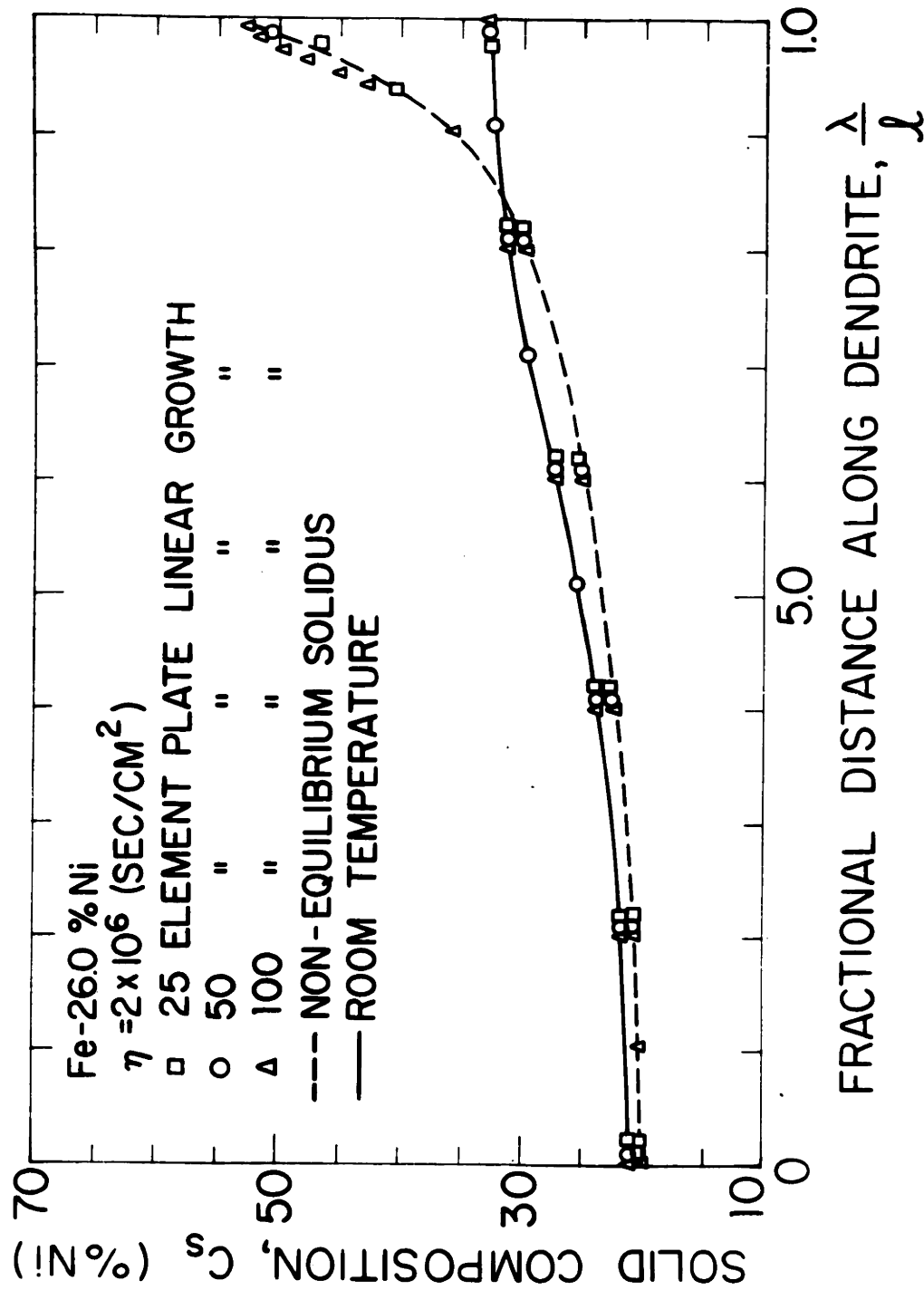


Figure 2-12 Predicted solute distribution at the solidus temperature and at room temperature for a 25, 50, and 100 element plate model for an iron-26 per cent nickel alloy with $\eta = 4 \times 10^6$. Mass Balance Technique.

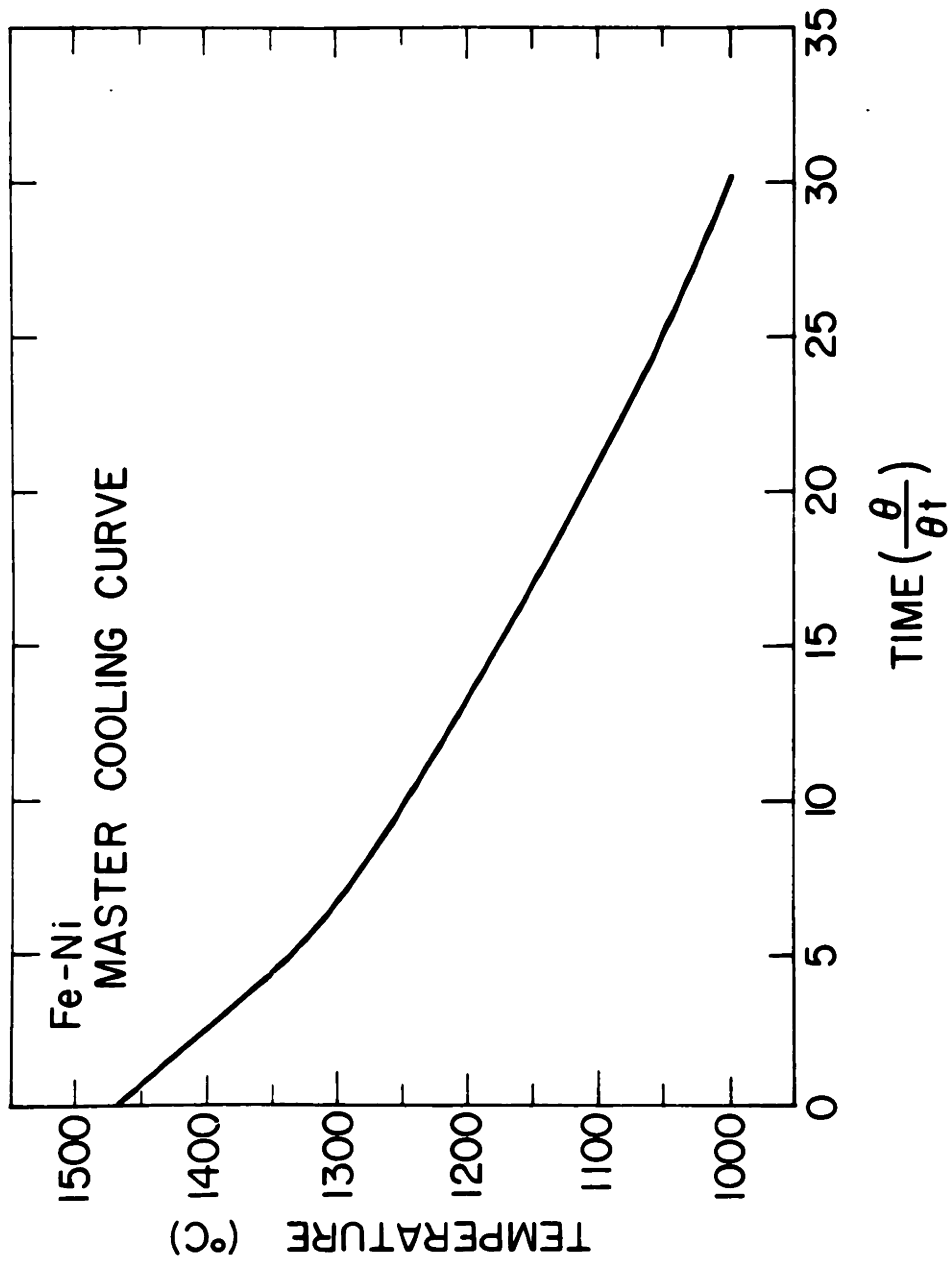


Figure 2-13. Master cooling curve for iron-nickel alloys.

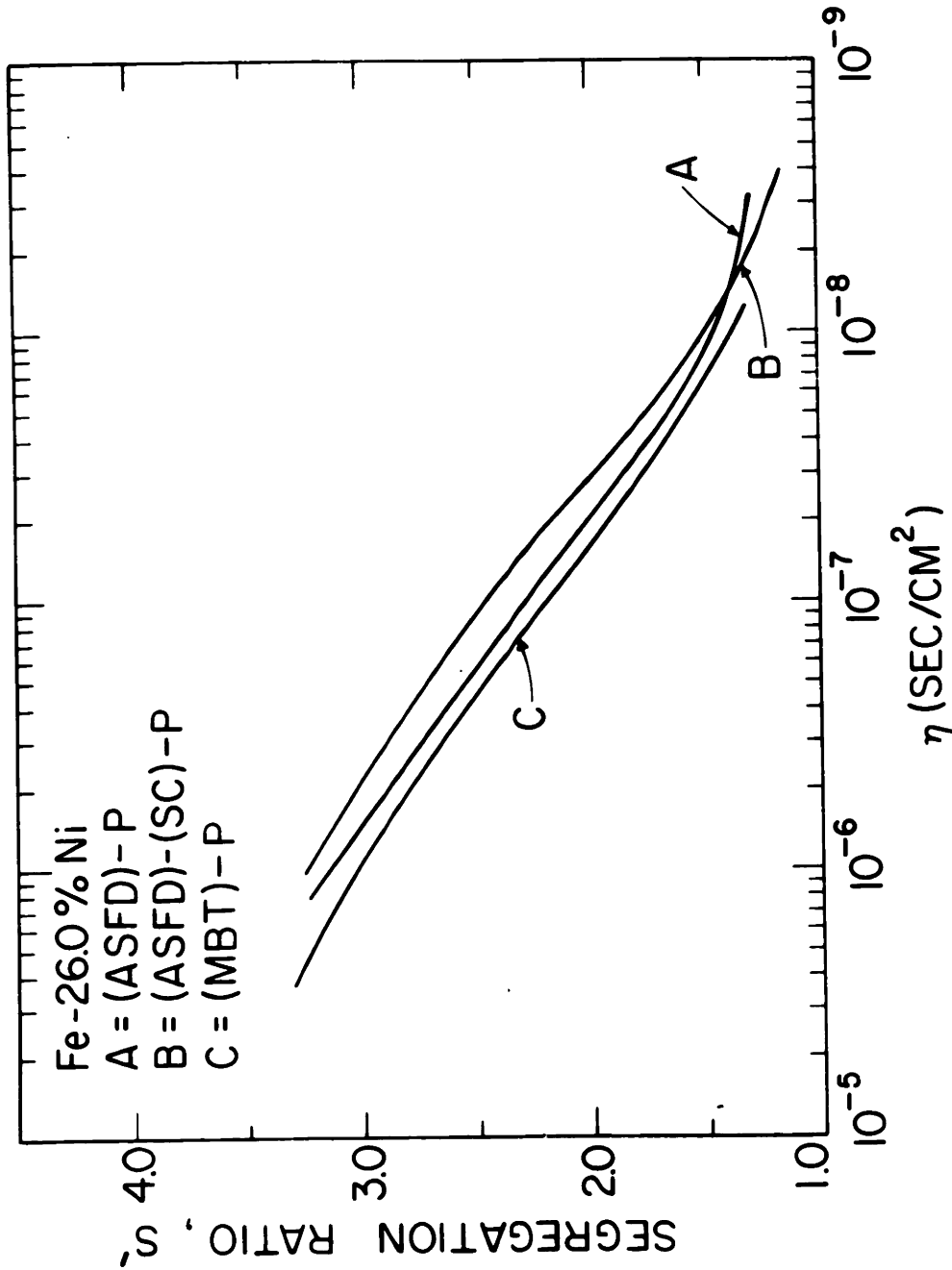


Figure 2-14. Predicted segregation ratios at the solidus versus η for an iron-26 per cent nickel alloy and plate model. Analytic solution finite difference method (ASFD), analytic solution finite difference method solute corrected envelope (ASFD)-(SC), Mass Balance Technique (MBT).

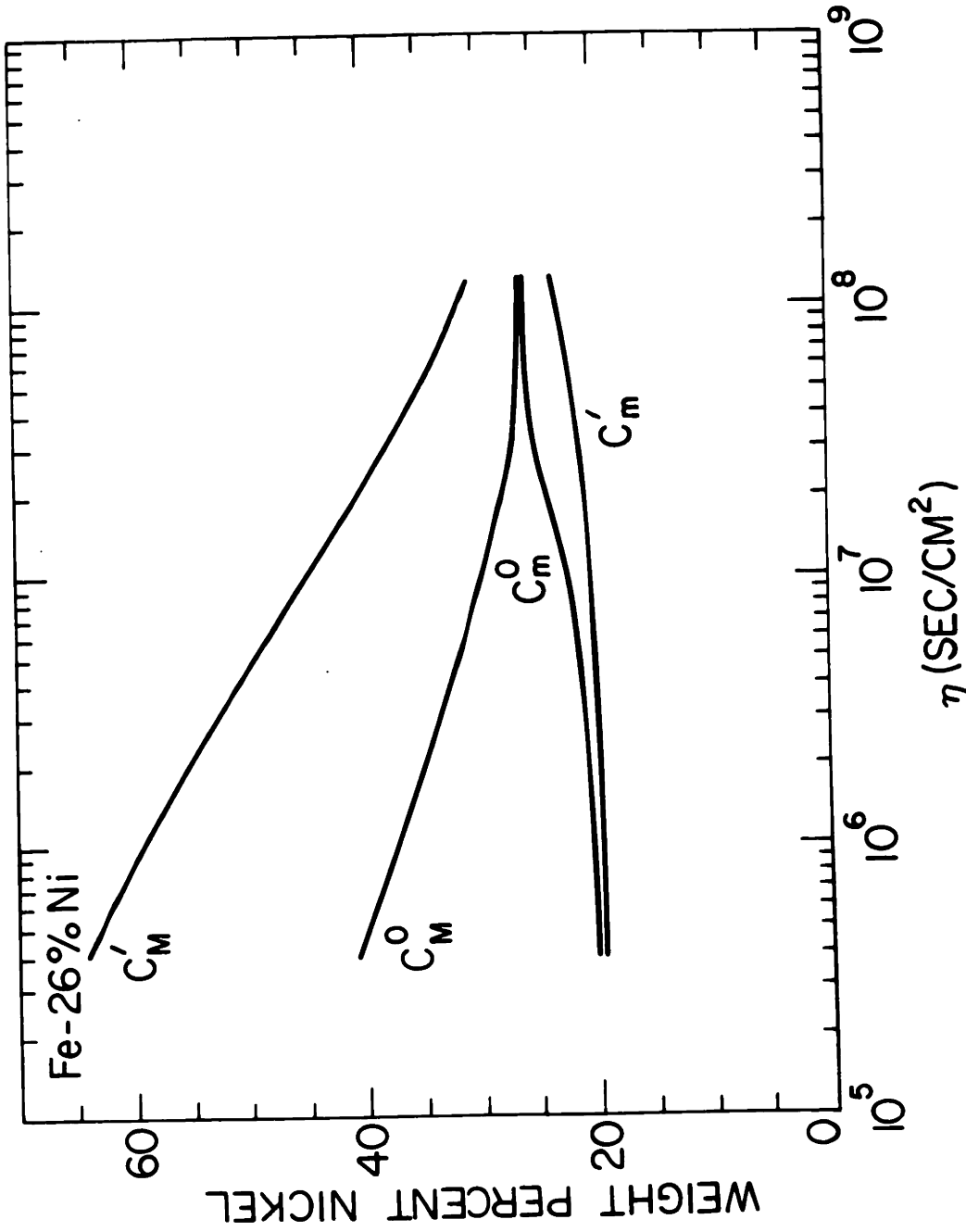


Figure 2-15. Predicted maximum and minimum solute contents as a function of η for an iron-26 per cent nickel alloy at the solidus and at room temperature. Mass Balance Technique - plate model.

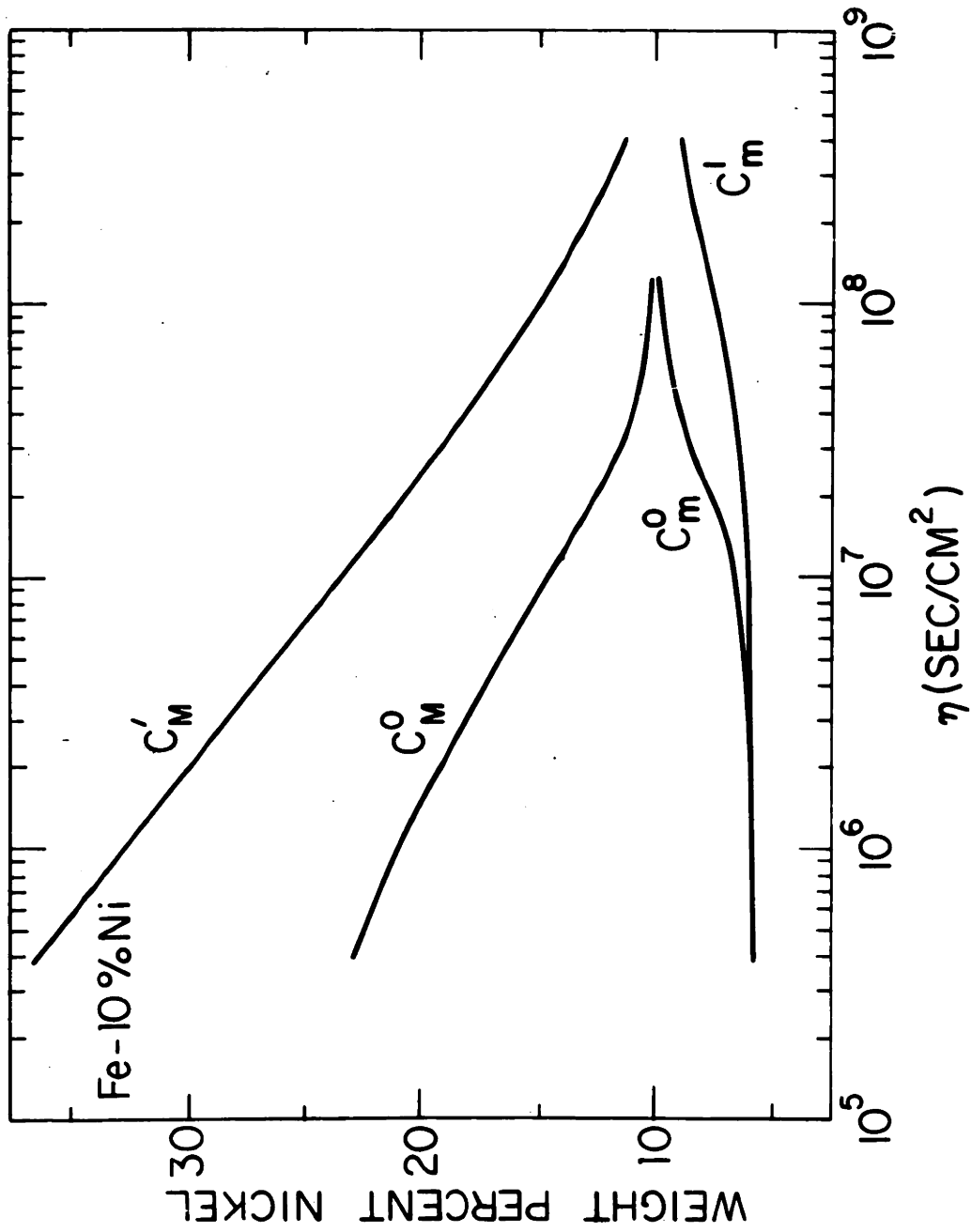


Figure 2-16. Predicted maximum and minimum solute contents as a function of η for an iron-10 per cent nickel alloy at the solidus and at room temperature. Mass Balance Technique - plate model.

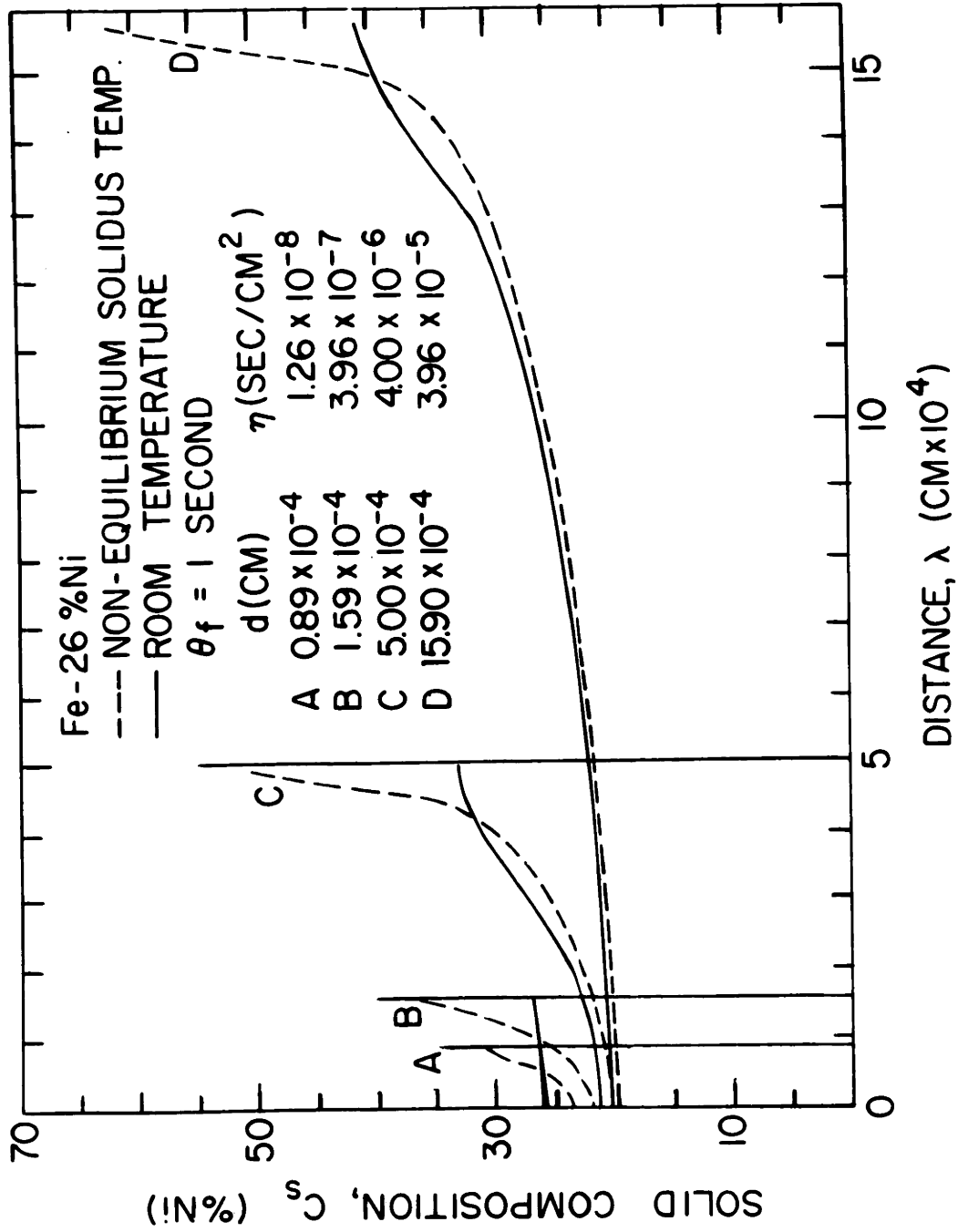


Figure 2-17. Distribution curves for an iron-26 per cent nickel alloy for several η values. Mass Balance Technique - plate model.

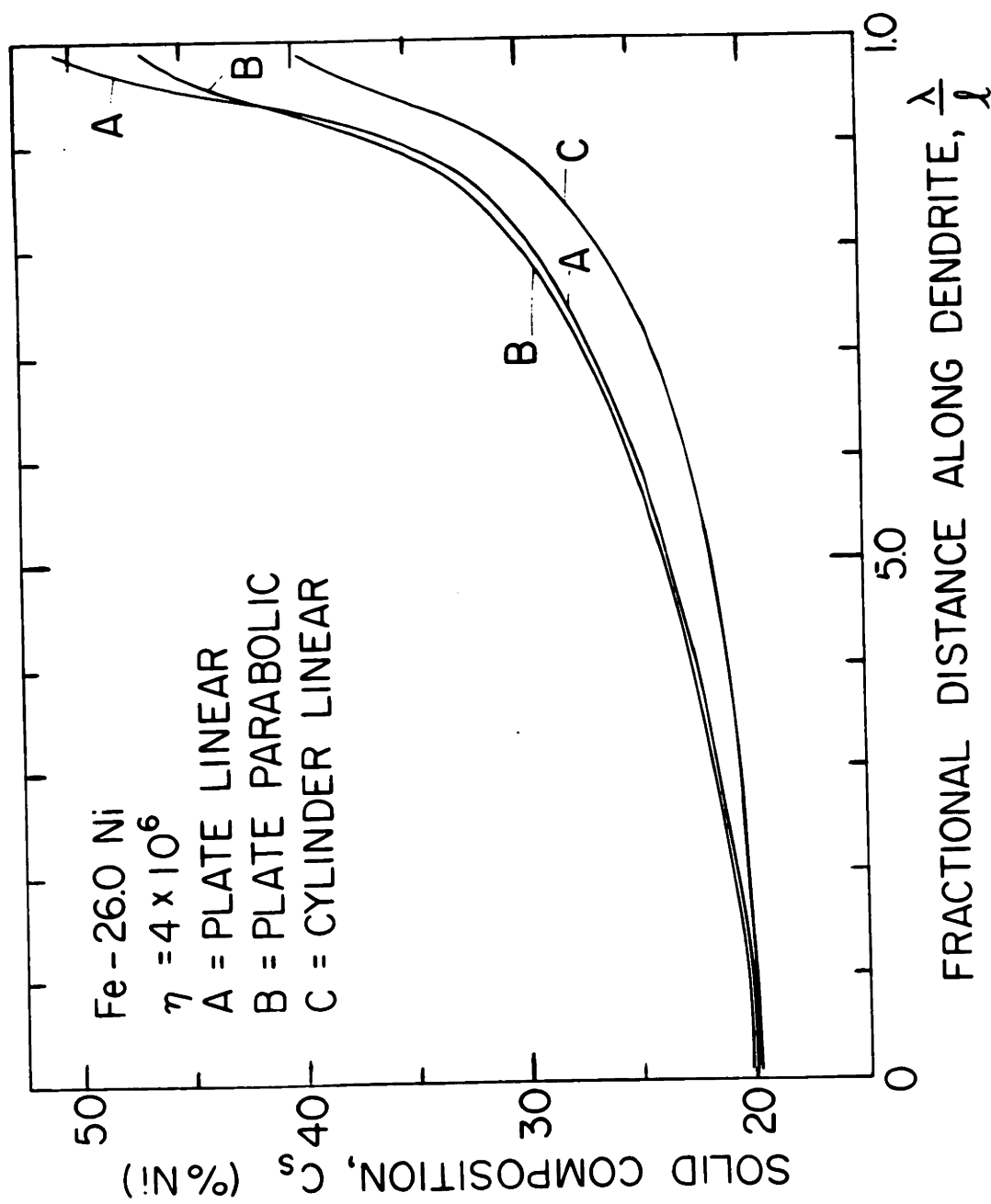


Figure 2-18. Predicted solidus temperature solute distribution for an iron-26 per cent nickel alloy with $\eta = 4 \times 10^6$ for different geometries and growth rates. Mass Balance Technique.

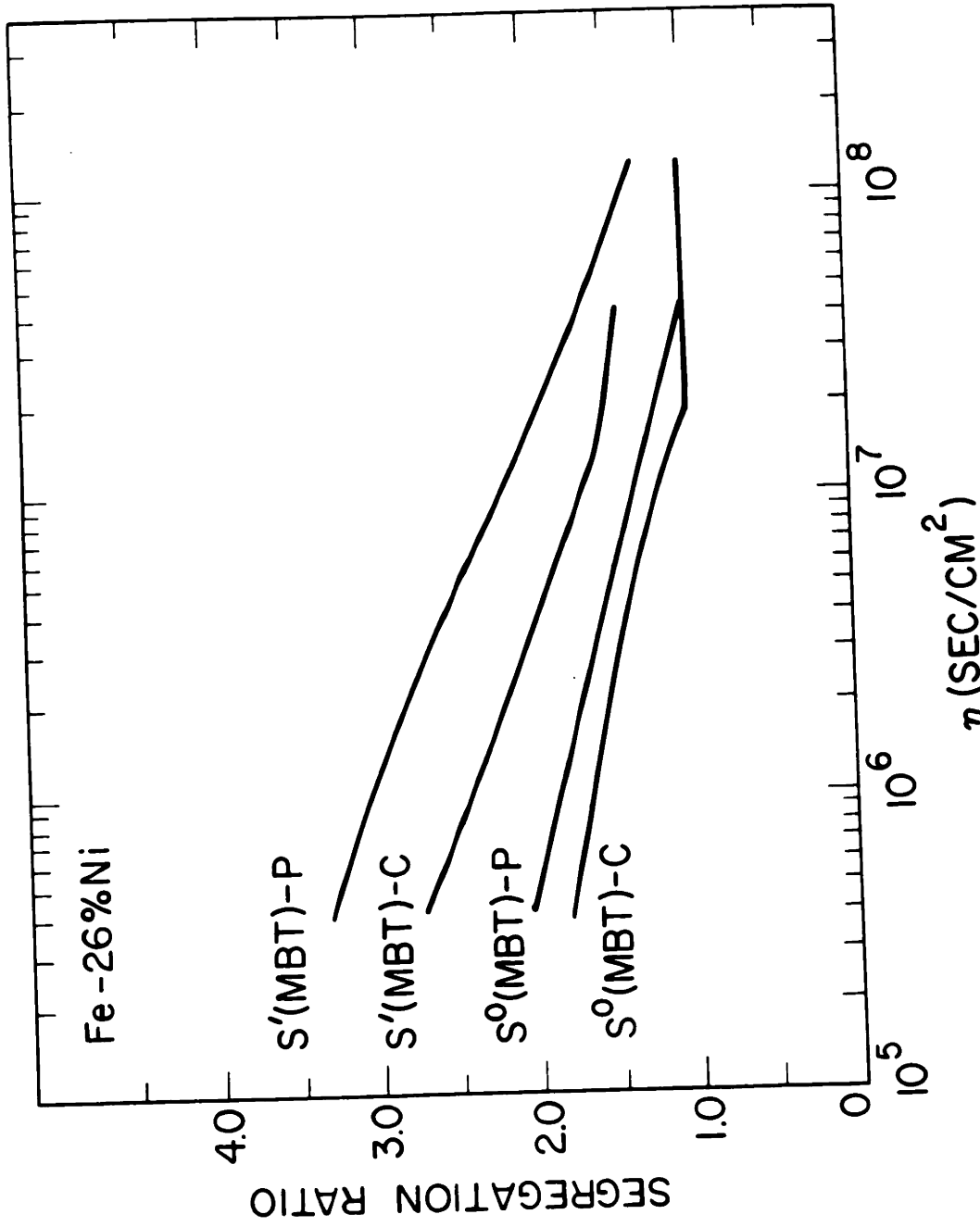


Figure 2-19. Predicted values of the segregation ratio at the solidus, S', and at room temperature, S⁰, as a function of η for an iron-26 per cent nickel alloy. Mass Balance Technique - plate model.

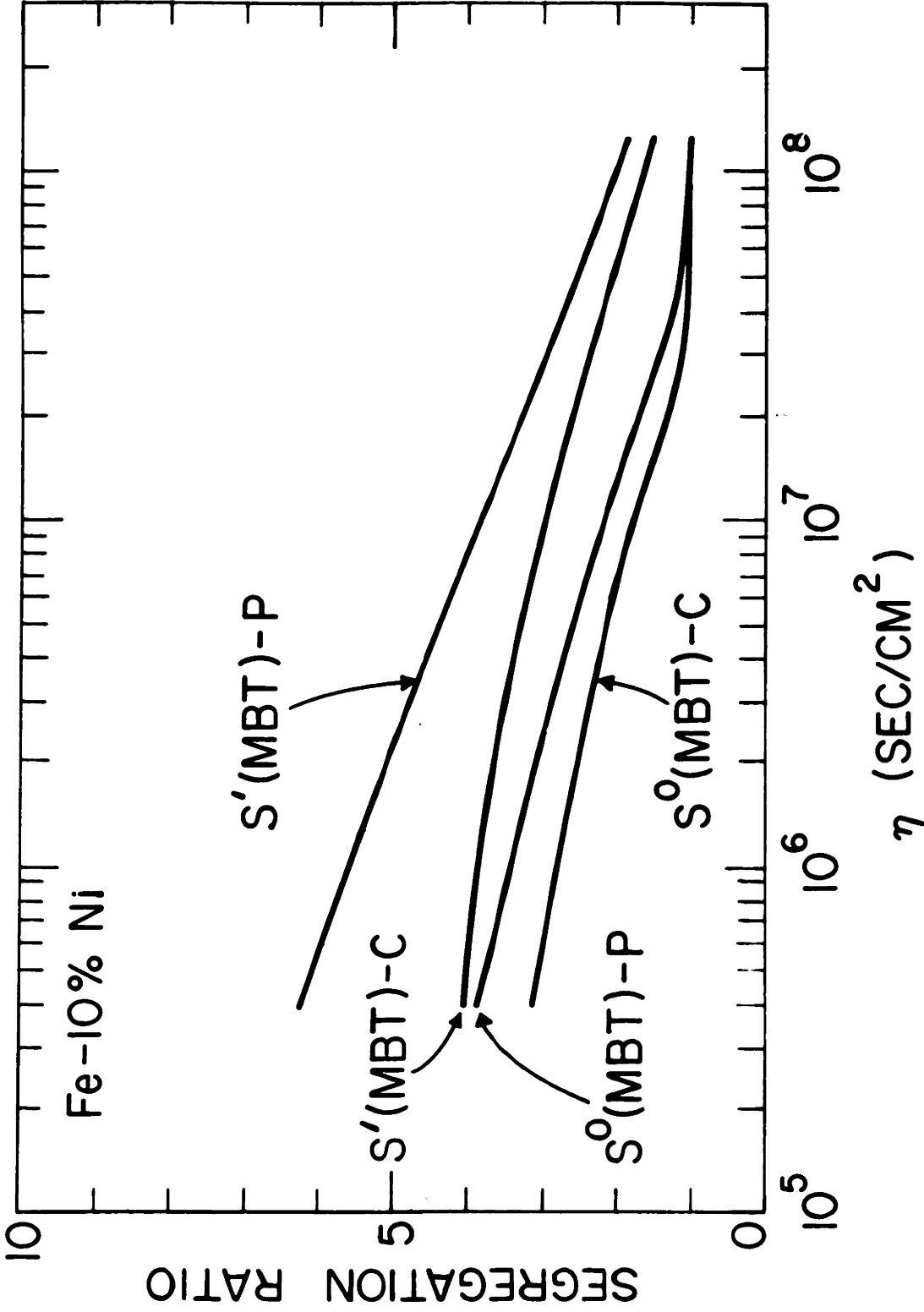


Figure 2-20. Predicted values of the segregation ratio at the solidus, S', and at room temperature, S⁰, as a function of η for an iron-10 per cent nickel alloy. Mass Balance Technique - plate and cylinder model.

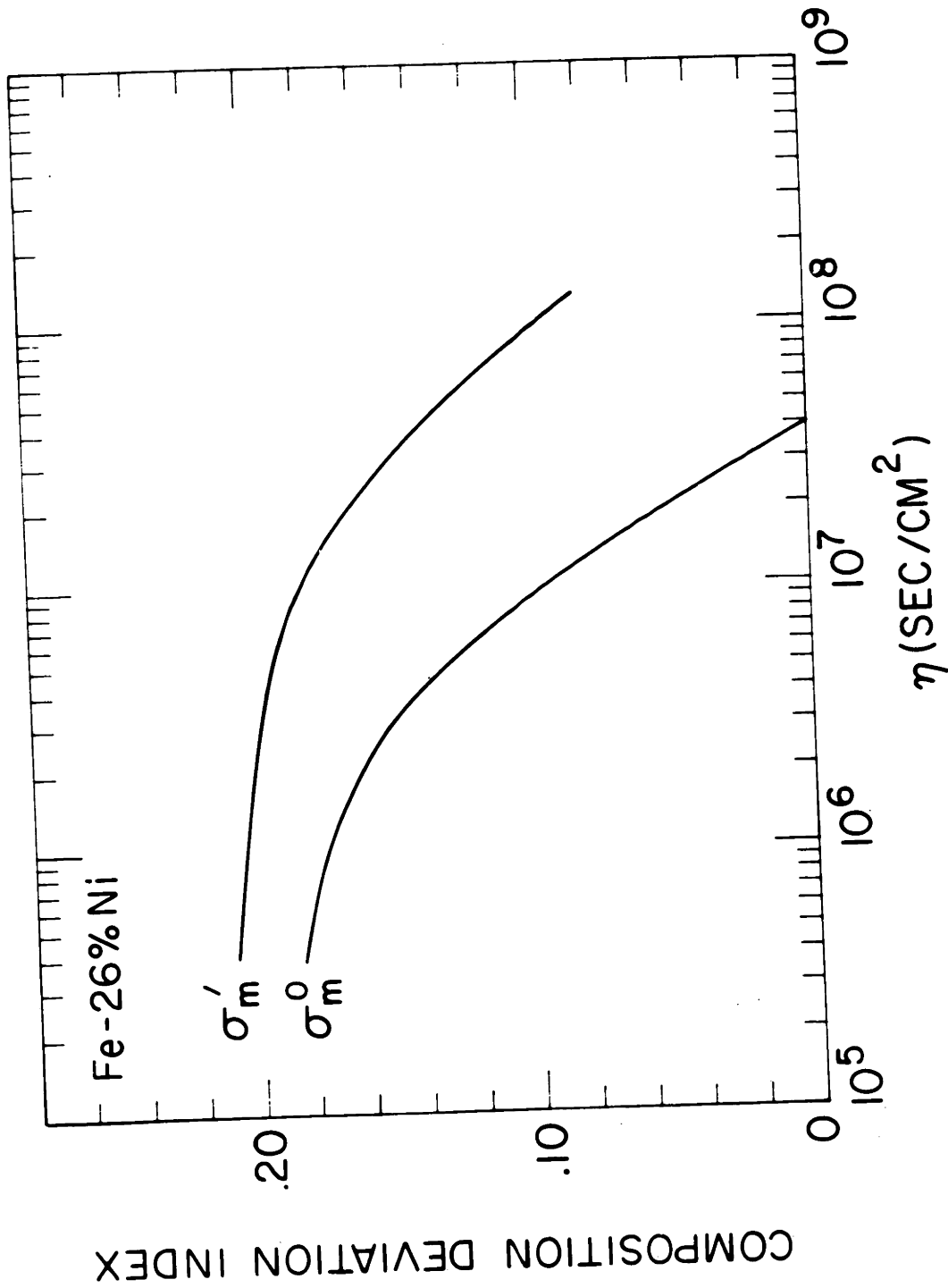


Figure 2-21. Predicted composition deviation index of the solidus, σ'_m , and at room temperature, σ_m^0 , versus η for an iron-26 per cent nickel alloy. Mass Balance Technique - plate model.

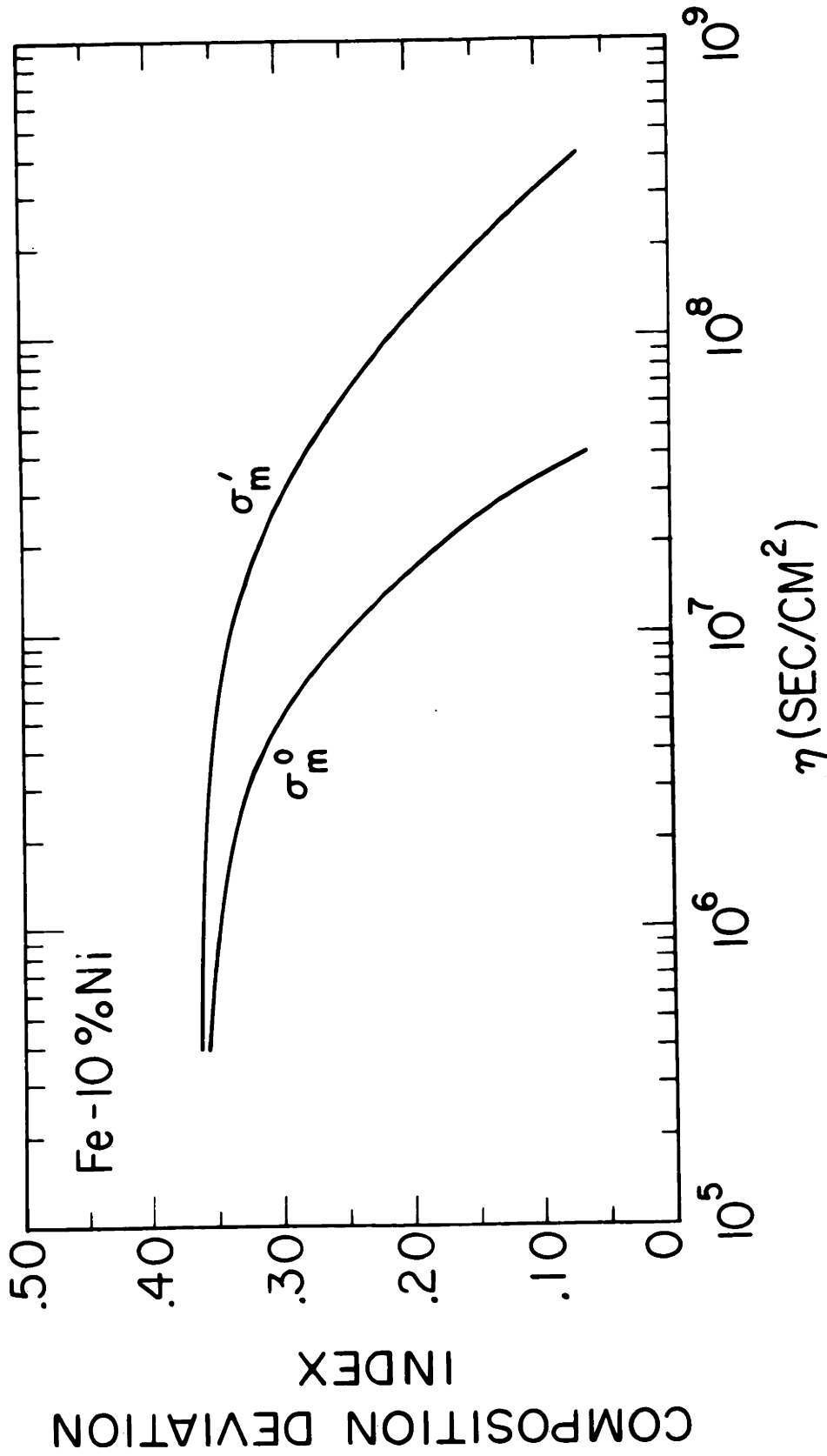


Figure 2-22. Predicted composition deviation index at the solidus, σ_m' , and at room temperature, σ_m^0 , versus η for an iron-10 per cent nickel alloy. Mass Balance Technique - plate model.

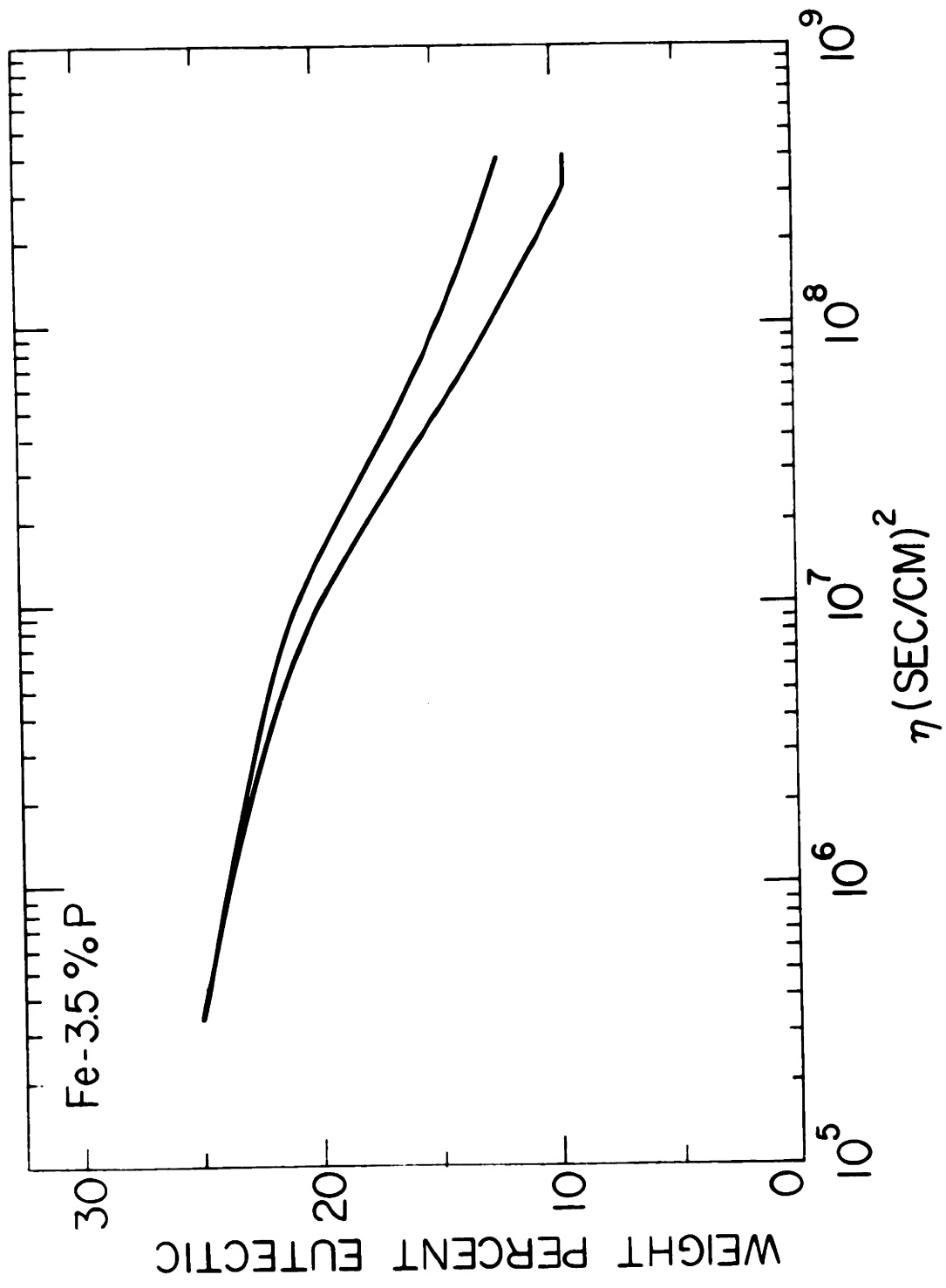


Figure 2-23. Weight per cent eutectic versus η for an iron-3.5 per cent phosphorus alloy. Mass Balance Technique - plate model.

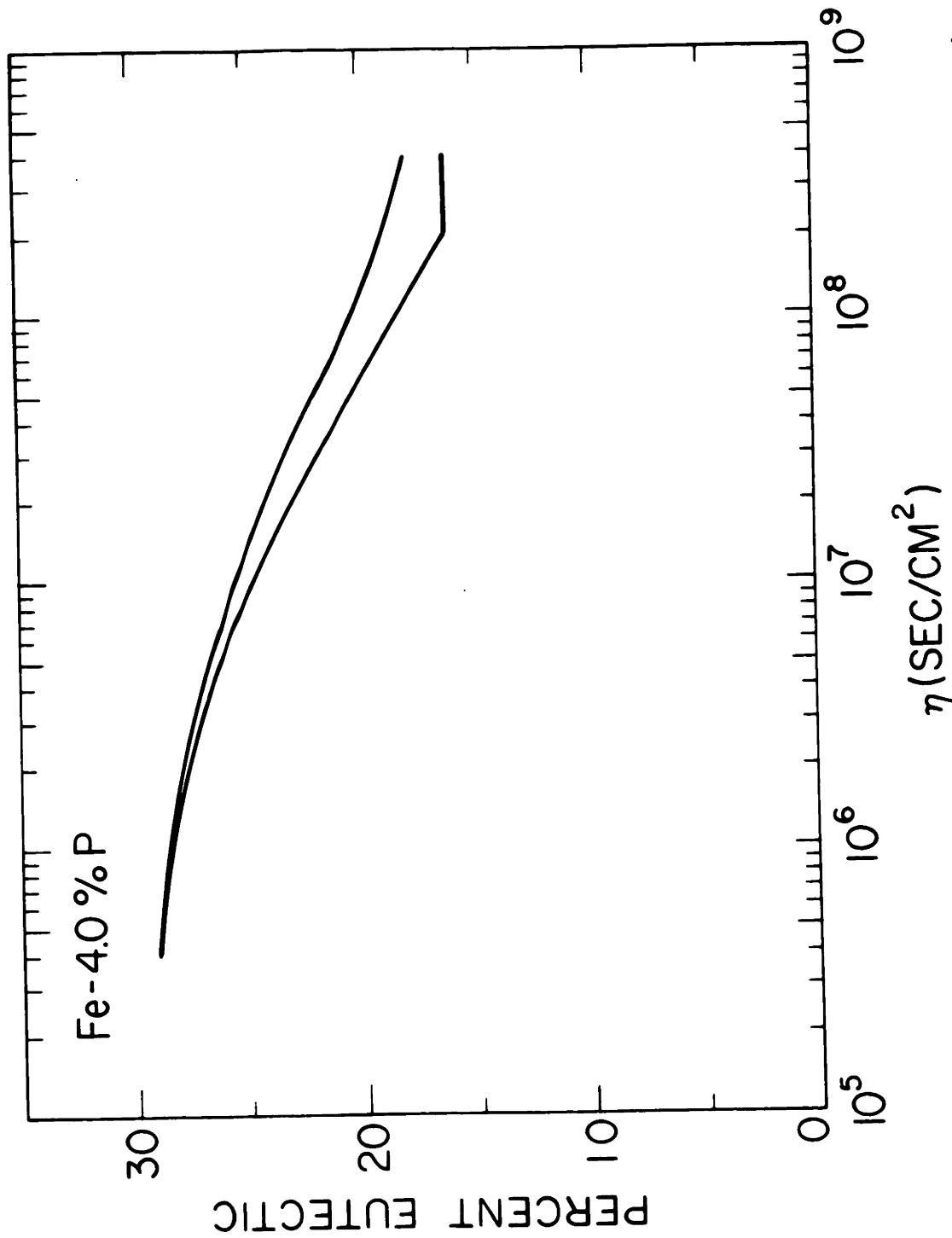


Figure 2-24. Weight per cent eutectic versus η for an Iron-4.0 per cent phosphorus alloy. Mass Balance Technique - plate model.

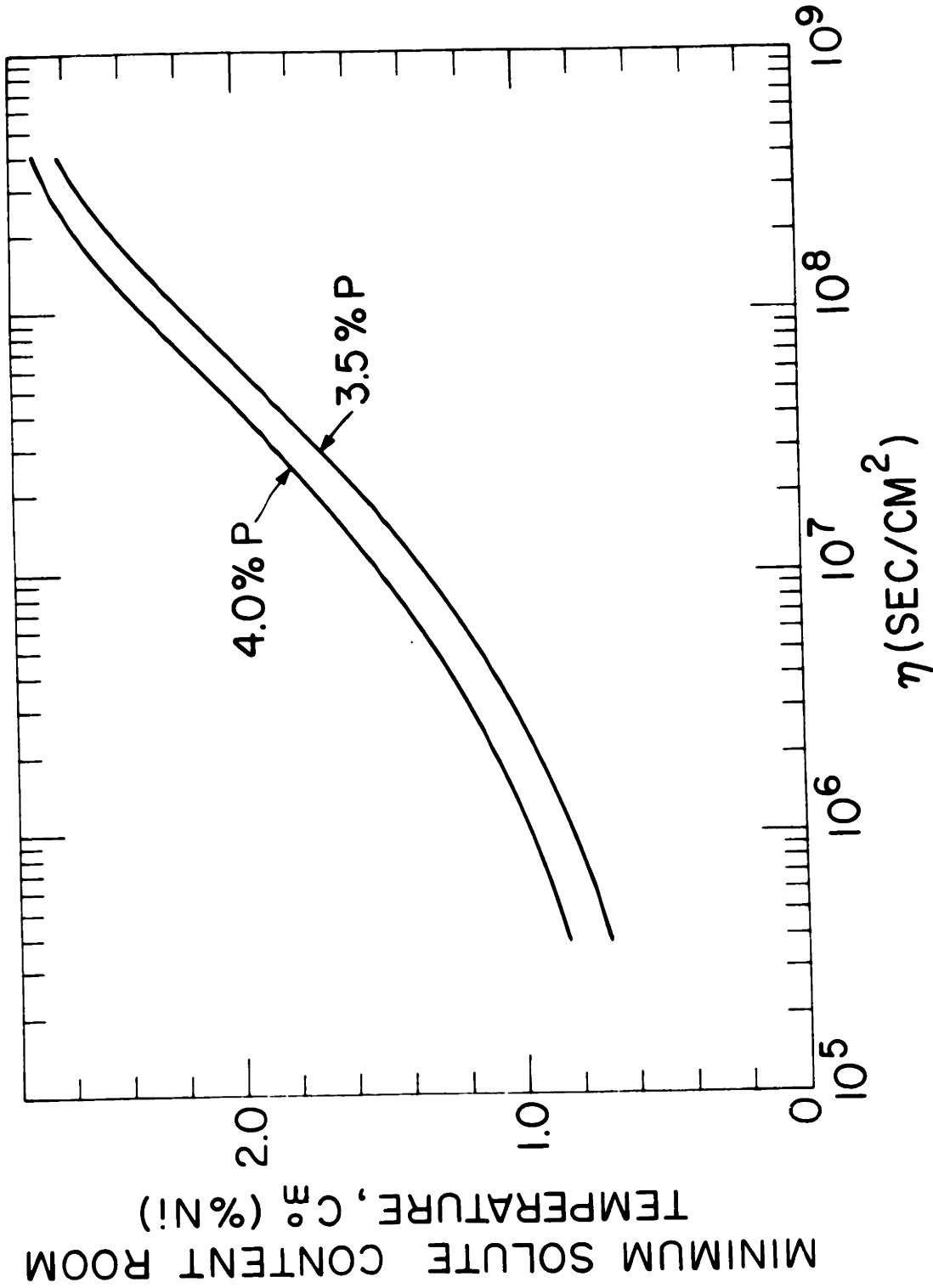


Figure 2-25. Minimum solute content C_m and at room temperature, C_m , for an iron-3.5 per cent phosphorus alloy. Mass Balance Technique - plate model.

III. INGOT PREPARATION

A. Alloys Investigated

A number of alloys were prepared in the iron-nickel iron-phosphorus, and iron-copper binary systems, and the iron-nickel-carbon ternary system for study of microsegregation and dendrite morphology. A list of the alloys cast, the charge compositions, and the results of chemical analyses are given in Table 3-1.

B. Melting, Molding, Casting

All heats were induction melted in clay graphite crucibles with rammed linings of magnesite. Melts were deoxidized by additions of 0.5 per cent aluminum. Part or all of the aluminum was added prior to tapping at 3000°F. In all cases the temperature of the melt was measured using an optical pyrometer prior to tapping. No further temperature measurements were made before pouring.

All of the ingots were cast in plate molds 1 inch thick by 5 inches wide by 8 inches high topped by a riser which tapered from 5 inches by 1 inch to 7 inches by 3 inches over a distance of 4 inches. A schematic diagram of this mold is shown in Figure 3-1. The mold was a composite of CO₂ sand and

a high temperature exothermic molding material. The exothermic sleeve was 1/2" thick at the chill and had a 5/24 in/in taper. The exothermic material ignites and heats to a temperature above that of the melting point of steel. Either of two commercial exothermic materials was used: Exomold E or LD Exothermic Material. To avoid gas pick-up the cope sections were all baked for a minimum of 24 hours at 600°F. The drag portion of the mold consisted of a water cooled copper chill block which was given a light zircon wash and supported by CO₂ sand.

Although the casting weighed 20 pounds, 40 pound heats were always melted in order to improve chemical and temperature control. The iron-phosphorous alloy was melted under argon gas to minimize phosphorous oxidation. All of the heats were skimmed, killed, tapped at 3000°F, and then top poured directly into the mold. The exothermic mold was not ignited before pouring. Hot water was first run through the chill until the molten metal was poured into the mold at which time cold water was used. This procedure prevented condensation on the chill. After filling the mold, the casting was capped with additional exothermic material to reduce top heat loss.

Structures of the castings poured were fully columnar with the columnar grains, extending from the chill up into the riser. Typical microstructures are shown in Figures 5-2 to 5-17 and are discussed in Section V.

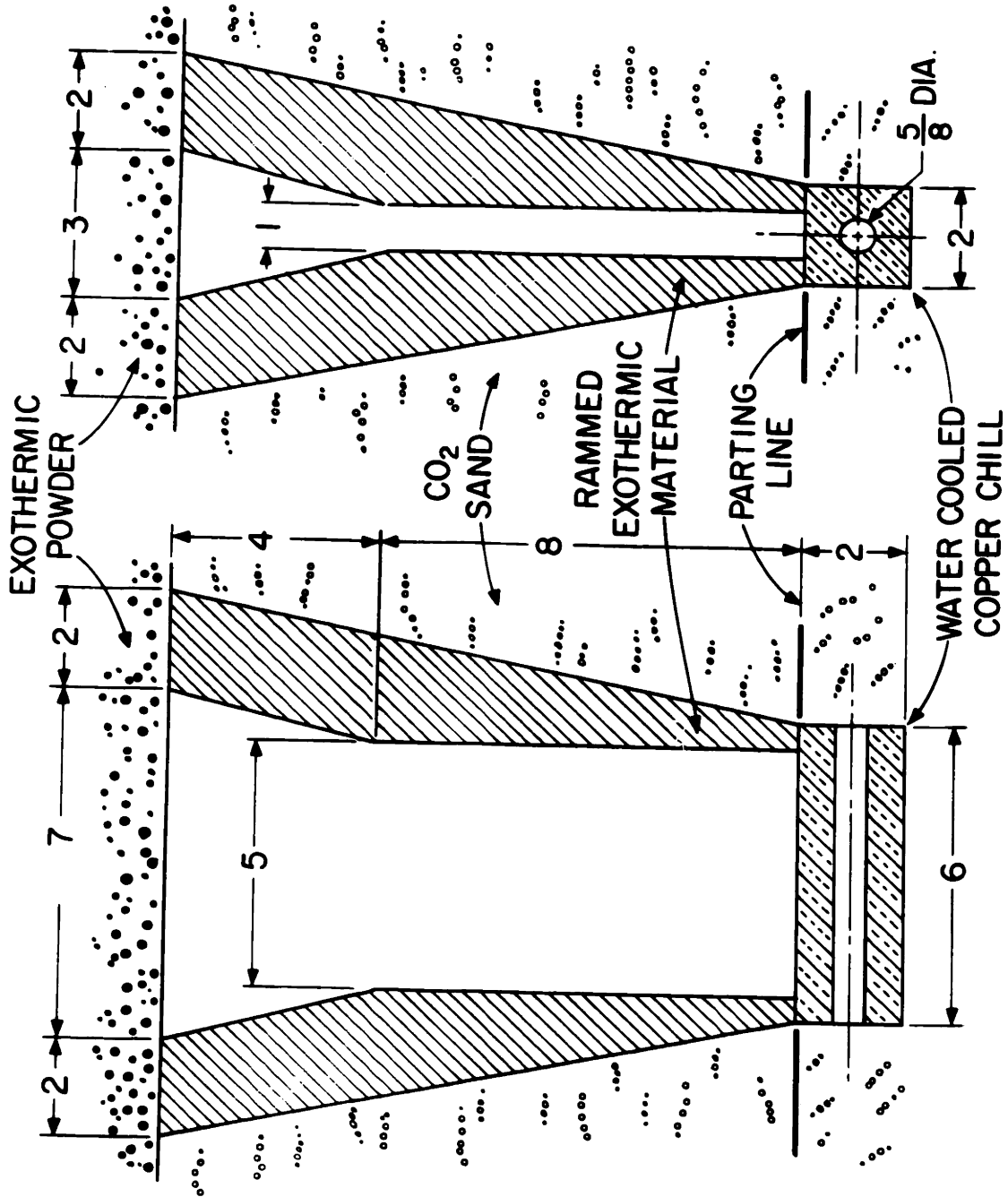


Figure 3-1. Schematic diagram of plate mold.

TABLE 3-1

Chemical Analyses of Ingots Studied

Heat Number	Nominal				Actual*				
	% Ni	% C	% Cu	% P	% Ni	% C	% Cu	% P	% Al
1	10.0	-	-	-	9.86	-	-	-	0.06
2	15.0	-	-	-	14.7	-	-	-	0.04
3	20.0	-	-	-	19.9	-	-	-	0.21
4	26.0	-	-	-	26.0	-	-	-	0.24
5	26.0	.12	-	-	25.0	0.12	-	-	0.14
6	26.0	.33	-	-	24.1	0.33	-	-	0.24
7	26.0	.42	-	-	24.6	0.42	-	-	0.18
8	26.0	-	-	-	25.8	-	-	-	0.47
9	-	-	-	4.0	-	-	-	3.1-4.1	-
10			25.0				25.0		0.005

*Chemical analyses were taken at approximately 1/2 inch from the chill. 0.5 per cent aluminum added as deoxidizer to all heats.

IV. THERMAL MEASUREMENTS

A. Introduction

Polich, Nereo and Flemings²⁸ have estimated from heat flow analysis the rate of advance of the dendrite tips in a unidirectionally solidified ingot with an exothermic sleeve. In addition, they experimentally measured the rate of advance of an isotherm in the solid-liquid zone (a) in a plate casting having an exothermic sleeve with a 7/32 in/in taper and (b) in a plate casting having an exothermic sleeve uniformly 1-1/2 inch thick. Their results comply with the following expressions:

$$7/32 \text{ in/in taper} \quad X = .20 \sqrt{\theta} - 1.80 \quad (47)$$

$$1-1/2 \text{ inch uniform} \quad X = .16 \sqrt{\theta} - 2.0 \quad (48)$$

where X = position of isotherm, inches

θ = time, seconds

Their experimental results are in good agreement with estimates made from heat flow analysis.

Thermal measurements were made for a unidirectionally solidified ingot of the design employed in this investigation for the following reasons:

- (1) The geometry of the exothermic sleeve used here was

slightly different than that used in the previous investigations²⁸.

- (2) A binary alloy, iron-26 per cent nickel, was used. The thermal properties of this alloy may not be much different from the 4340 alloy studied previously, however, in this instance, a reasonable value of the nonequilibrium solidus can be computed (using the equilibrium phase diagram and the computations discussed in Chapter II). Thus, a good estimate of the solidification time is possible.
- (3) Use of a thermocouple design capable of rapid response allowed measurement of cooling curves all the way to room temperature at positions relatively close to the chill.

B. Experimental Procedure

Thermal measurements were made during the solidification and cooling of an iron-26 per cent nickel ingot (ingot No. 8) cast in a mold of the design discussed in the previous section and drawn in Figure 3-1. Twenty mil platinum-platinum-10 per cent rhodium thermocouples were inserted horizontally through the exothermic sleeve in the 5-inch direction at distances from the chill of 1 inch, 2 inches, 3 inches, 4 inches, 5 inches and 6 inches. Each thermocouple was protected by 1/16-inch I.D. and 1/8-inch I.D. fused silica tubes. In addition, a 3/16-inch fused silica protection tube was used where the thermocouple penetrated the exothermic, and a layer of CO₂ sand about 1/4 inch thick separated each thermocouple ensemble from the exo-

thermic material. The thermocouple wire was brought out to an ice bath cold junction and connected to the recording instruments by copper lead wire. The output of the two thermocouples closest to the chill were recorded continuously on a Moseley model 1100A two pen strip chart recorder. The remaining four thermocouples were read at thirty second intervals on a Honeywell Elektronik 16 multipoint strip chart recorder. Prior to pouring of the ingot, recording channels were calibrated individually.

Inserting the thermocouples through the long horizontal direction of the plate and separating them from the exothermic material by a layer of CO_2 sand minimized both the effect of heat from the exothermic reaction on the temperature of the thermocouple junction and the effect of the thermocouple assembly on thermal conditions within the ingot. By using such thin protection tubes the volume occupied by the thermocouples was less than 4 per cent in the first six inches of the casting.

The response of the thermocouple ensemble was determined in a separate run by measuring the time for a cold thermocouple to reach the temperature of a steel bath poured around it. The thermocouple ensemble used here reached 1500°C in 8 seconds. This can be compared roughly with the thermocouple design used previously²⁸ which required 58 seconds to reach 1500°C in an analogous experiment.

After the run, the ingot was sectioned and the positions of the thermocouples were measured. These measured positions listed in Table 4-1 are used in the plots and calculations that follow.

C. Results of Thermal Measurements

Cooling curves measured for a unidirectionally solidified ingot are shown in Figure 4-1. The sharp change in slope of each curve indicates the time the dendrite tips reach the position of the thermocouple (due to the higher thermal conductivity of the solid). It is clear that the solidification front progresses unidirectionally from the chill. The breaks measured at thermocouples 3, 4, 5 and 6 occur at very close to the same temperature, namely 1468°C.

The position of the solidification front, X_L , identified by the thermal breaks is plotted as a function of the square root of time in Figure 4-2. Also plotted is position of the solidus, X_S (taken as liquidus minus 25°C).^{*} Using least squares analysis, straight lines were fit to the data. The following expressions result:

$$X_L = .153\sqrt{\theta_L} - .239 \quad (49)$$

$$X_S = .145\sqrt{\theta_S} - .238 \quad (50)$$

^{*}This solidification range was predicted as the difference between the liquidus and nonequilibrium solidus temperatures to yield a segregation ratio of 1.20.

with time expressed in seconds and distance in inches.

The solidification time, θ_f , as a function of distance from the chill may be derived from equations (49) and (50) as the difference between the arrival of the solidification front and the time to cool through the solidification range and reach the nonequilibrium solidus. The resulting expression is:

$$\theta_f = 4.84 X^2 + 2.22 X + 0.25 \quad (51)$$

The square root of the solidification time, θ_f , is plotted as a function of distance from the chill in Figure 4-3. Note that extrapolation of this curve to points close to the chill is not possible since here interface resistance governs heat flow and thus controls growth.

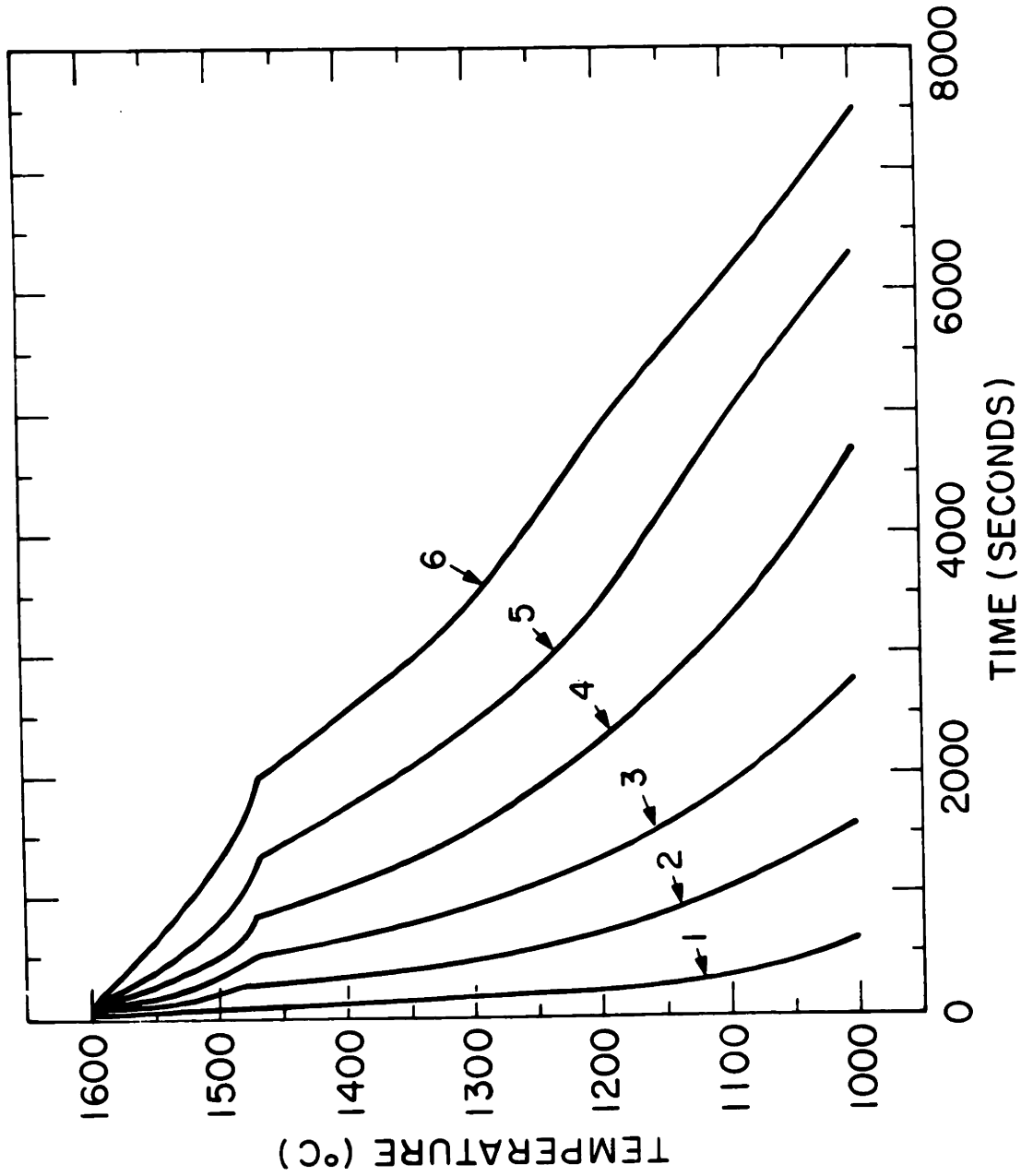


Figure 4-1. Cooling curves from the unidirectionally solidified ingot with thermocouples at 1.13, 2.17, 3.15, 4.17, 5.36, and 6.53 inches from the chill.

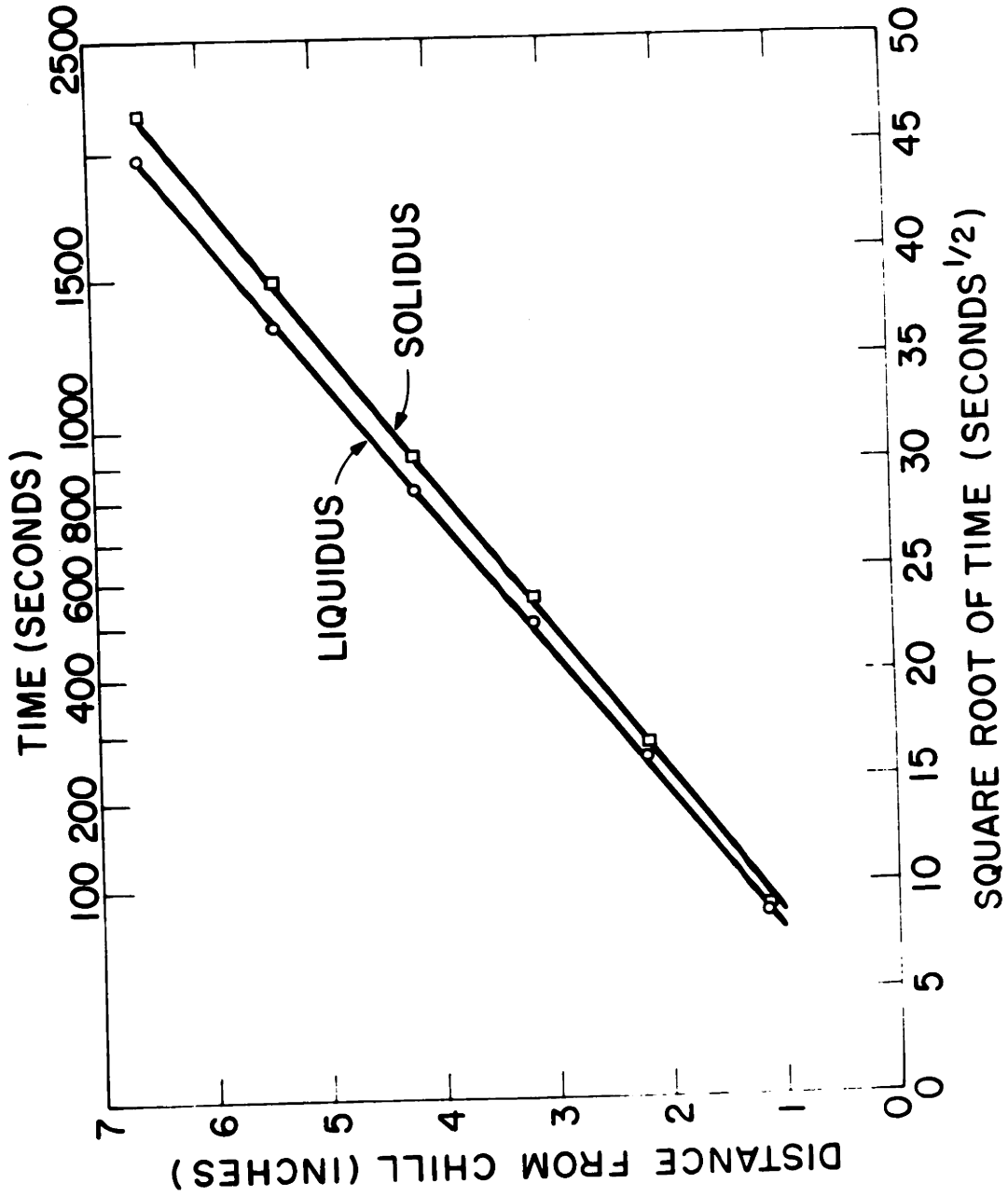


Figure 4-2. Positions of the liquidus and solidus isotherms as a function of the square root of time.

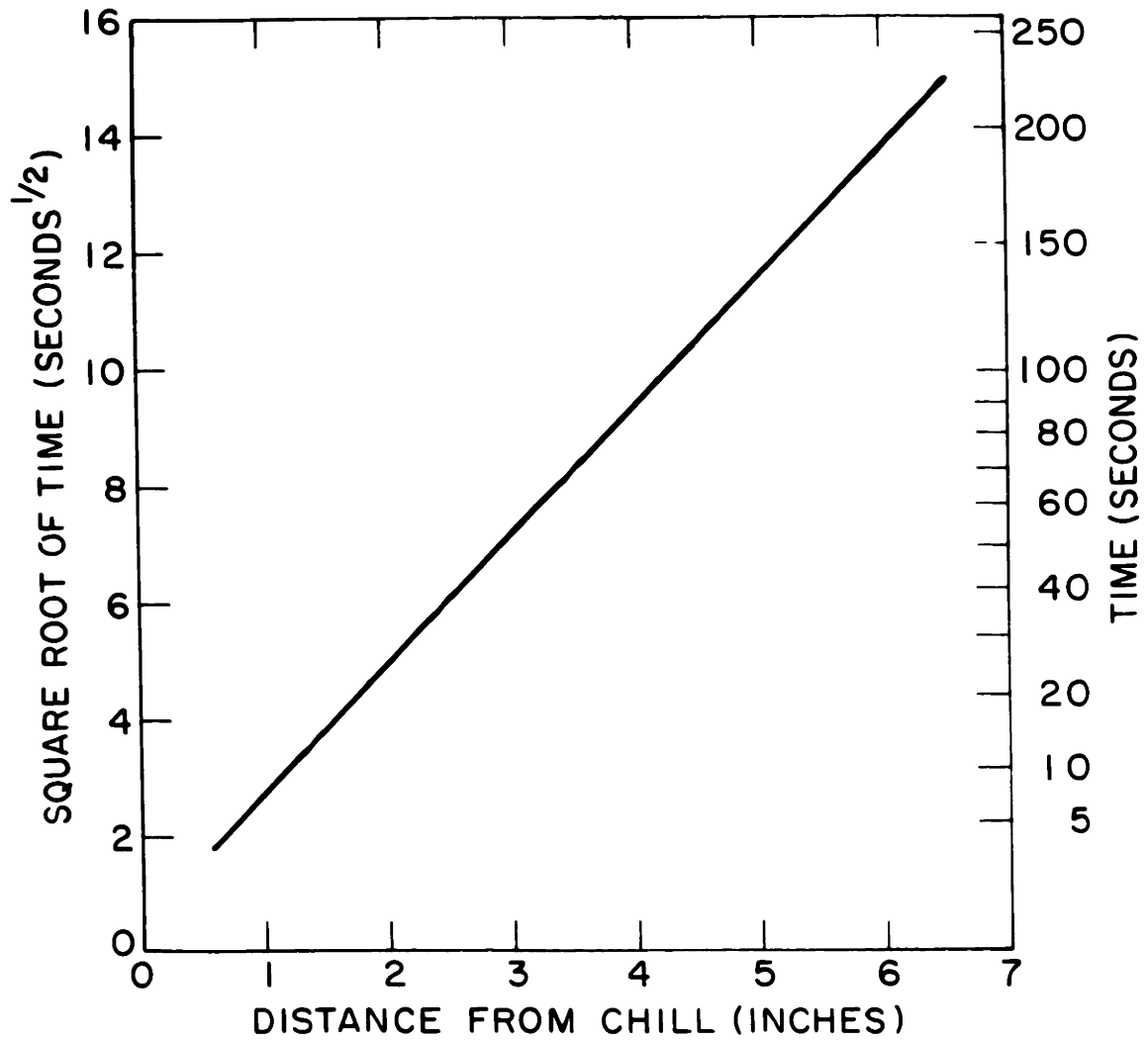


Figure 4-3. Square root of solidification time versus distance from the chill.

<u>Thermocouple Number</u>	<u>Distance from the Chill (inches)</u>
1	1.13
2	2.17
3	3.15
4	4.17
5	5.36
6	6.53

Table 4-1. Thermocouple locations with respect to the chill surface after solidification.

V. MORPHOLOGY

A. Introduction

The dendritic structure observed within cast grains (upon etching after solidification) results from microsegregation. Generally, the etch delineates lines of approximately equal concentration. In the absence of solid diffusion these isoconcentration lines (and hence the etched structure) are an accurate representation of the liquid-solid interface at various stages of solidification. Solid diffusion modifies the apparent dendrite morphology somewhat but the final apparent morphology remains an indication of the growth morphology.²⁴ The terminology used in this thesis follows that of Bower and Flemings¹² as follows. Classically, dendrites have been represented as "rods". Rods that form the primary axes of dendrite elements are termed primary growth forms (primary rods, primary dendrite arms). Rods which grow perpendicular to the primary rods are secondary growth forms (secondary rods, secondary dendrite arms). Tertiary and quaternary growth forms may also be present (see Figure 5-1).

In many systems at some stages of growth, dendrite morphology is at least partly plate-like or sheet-like. Interstices between primary and secondary "arms" tend to "fill in" at an early stage of solidification; the sheets which form in this (or other) way are termed primary plates or primary sheets. Sheets oriented parallel to secondary arms and perpendicular to primary sheets

are termed secondary sheets; sheets containing two tertiary arms and parallel to a primary sheet are tertiary sheets.

When no secondary branches at all occur the resulting structure is sometimes termed "cellular". Several researchers have indicated that cellular structures, instead of dendritic structures, are found when the value $G_L k / C_0 R_t^{1/2}$ is sufficiently low, where G_L is thermal gradient in the liquid, C_0 is initial alloy content, k is the equilibrium partition ratio, and R_t is growth rate of the dendrite (or cell) tips.³⁰

B. Procedure

The specimens for metallographic morphology studies were taken from the plates in one-half inch increments in planes parallel to the chill surface (transverse sections). Longitudinal sections were also taken from these same specimens across the one-inch dimension of the plate and near the center of the 5-inch dimension. The etch used for all iron nickel alloys was a dilute Marble's reagent; iron phosphorus and iron copper were etched with Stead's reagent two followed by a mixture of ammonia, hydrogen peroxide, and water to remove the copper precipitated from the Stead's etch.

Photomicrographs of areas 1, 2 and 4 inches from the chill surface and parallel to it and areas between 1 to 1-1/2, 2 to 2-1/2 and 4 to 4-1/2 inches from the chill surface and perpendicu-

lar to it are illustrated at both 7.6X and 34X magnification in Figures 5-2 to 5-15 for iron-nickel alloys; Figure 5-16 for iron-copper at 64X; and Figure 5-17 for iron-phosphorus at 34X.

C. Observations

In unidirectionally solidified castings, freezing time (time for a given location in the casting to go from liquidus to solidus temperature; note Figure 4-3) is approximately proportional to the square of the distance from the chill. Hence examination of such castings at different distances from the chill permits qualitative and quantitative correlation of structure with cooling rate.

A general observation from this work is that the dendrite structure tends to be more fully developed with increasing solidification time. In the iron-10 per cent nickel alloy (Figures 5-2, 5-3), for example, the structure appears fully cellular near the chill, with no evidence of side branching or preferential lateral growth in crystallographic directions. At distances removed from the chill, crystallographic effects begin to become evident with formation of the typical "cruciform" cross section; side branching also becomes evident.

The tendency to cell formation or minimal side growth at high cooling rates was noted in all of the alloys studied although the structure at any given cooling rate also depended on alloy content as discussed below.

The photomicrographs of ingots 1, 2, 3, and 4 (Figures 5-2 to 5-9) which contain 10, 15, 20 and 26 per cent nickel respectively, illustrate the effect of nickel content on solidification morphology. At a given cooling rate, increasing alloy content results in more completely formed dendritic structures. For example, the iron-10 per cent nickel alloy near the chill shows no apparent tendency toward preferential growth in crystallographic structure. As nickel content increases, the horizontal section near the chill shows a gradually more angular structure until at the 26 per cent nickel alloy, well developed cruciforms are seen, with side branching evident in the vertical section.

The ingots containing carbon (ingots 5 to 7) all exhibited larger grain sizes, dendrite spacings, and higher order growth forms than the ingot of equivalent alloy content (26 per cent nickel) that was free of carbon. Transverse sections nearest the chill contain practically no rounded cell type dendrite elements in the center of grains—even in the 0.12 per cent carbon alloy. Carbon also promotes tertiary growth. Within each casting the trend toward increasing dendrite complexity with increasing distance from the chill is evident.

In addition to the iron-nickel and iron-nickel-carbon systems the morphologies of iron-3.5 per cent phosphorus and iron-25 per cent copper were studied. Photomicrographs of these are shown in Figures 5-16 and 5-17. Both binary systems exhibit

stronger tendencies to form cruciform shapes at equivalent cooling rates than the iron-nickel alloys, although the phosphorus alloy contains less than one half the solute content of the lowest iron-nickel alloy.

The iron-copper alloy resembled the iron-nickel alloys as areas perpendicular to the heat flow direction exhibited a well defined cruciform structure and few noticeable tertiary arms. The iron-copper alloy exhibits clover leaf shaped crosses which grow larger rather than branch as the distance from the chill increases (decreased cooling rate); the most favorably growth oriented dendrites growing and stifling the others. In contrast, the iron phosphorus alloys show considerable elongation of the arms of the original cruciform and branching from these arms. Extensions appeared random in that cruciforms with one, two, three, or all four arms extended were observed in horizontal sections. Because of this the dendrite structure was quite complex and primary dendrites difficult to distinguish—especially at slower cooling rates.

D. Dendrite Arm Spacing Measurements

Two methods were used to obtain primary dendrite arm spacing measurements from transverse 12X magnification photomicrographs of samples taken at one-half inch increments from the chill.

The linear method involved finding representative areas and

measuring the average distance between cross centers of adjacent dendrite elements whose arms were aligned. Cellular areas were measured by averaging the distance between cell centers. For regions consisting of complex, higher-order growth forms, and larger spacings, where primary dendrite crosses were not easily distinguished and usually unaligned, the area method was used.

The area method consisted of counting the number of primary arms contained in a given area (2 centimeters square) and calculating the spacing by assuming a simple cubic array.

Secondary dendrite arm spacing measurements were made on 12X magnification photomicrographs of longitudinal sections which exhibited regions passing through a primary dendrite core at a slight angle or those which showed the secondary arm attachment to the primary stalk. The spacing taken was that adjacent to the primary stalk.

Results of the dendrite arm spacing measurements are plotted in Figures 5-18 to 5-20 and given in Appendix B. The primary dendrite arm spacing for the 10, 15 and 20 per cent nickel alloys were very nearly the same at corresponding distances from the chill. The 26 per cent nickel alloy exhibited an increase of approximately 1.5 times the spacing of the first group. The addition of carbon generally increased the primary spacings.

Not all castings made possessed measurable secondary arms.

In those that did, alloy content had little effect on spacing at locations in the first several inches from the chill. Addition of carbon tended to increase the secondary arm spacing, particularly at distances removed from the chill, Figure 5-18. The secondary spacing was not affected by cooling rate as much as was the primary arm spacing.

The iron-25 per cent copper alloy exhibited a finer dendritic structure than any other alloy while the phosphorus primary spacing was largest of the binary alloys examined.

E. The Power Law

Based on the dendrite arm spacing measurements, solidification times and equation (12) $\lambda = \gamma\theta_f^n$, the effect of cooling rate on microsegregation can be predicted qualitatively. The exponent n in the case of iron-26 per cent nickel alloy was found to be approximately 0.4 by plotting $\log d$ versus $\log \theta_f$ where d is the measured dendrite arm spacing. Since n is less than .5 less segregation would be expected at slower cooling rates, i.e., farther from the chill.

The iron-phosphorus alloy data could not be plotted directly as the solidification times were not measured for this alloy. This may be surmounted by using the relation:

$$X_1 = C_1 \sqrt{\theta} + C_2 \quad (52)$$

where C_1 and C_2 are constants. Combining equations (12) and (52) results in:

$$d = C_3 (X - C_4)^{2n} \quad (53)$$

where C_4 and C_5 are constants. Thus if $\log (d - C_5)$ is plotted versus $\log X$ the slope will be $2n$. Plots of $\log d$ versus $\log X$ were not linear but if X was shifted by altering corresponding to C_4 then linearly improved X by a constant. The resulting loci of points could all be approximated by lines whose slopes were between 0.8 and 1.1. Thus, n , the exponent in all cases was very nearly 0.5. This predicts little change if any in microsegregation with cooling rate, i.e., distance from the chill. The validity of this prediction is compared with actual microprobe segregation measurements in Chapter VI for iron-nickel and iron-phosphorus alloys.

F. Summary

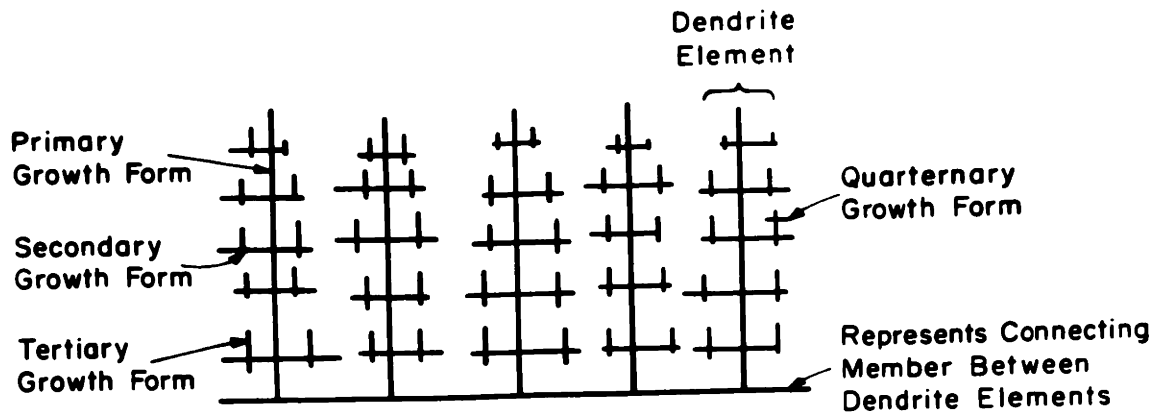
The foregoing morphological study shows that the structure found in the iron-nickel iron-phosphorus, iron-copper and iron-nickel-carbon alloys is considerably more complex than the simple flat plate growth assumed in Section II for microsegregation analyses. The structure of the binary iron-nickel alloys tends to be cellular at low nickel contents and at rapid solidification rates (near the chill). At higher alloy contents and greater distances from the chill crystallographic effects become apparent with formation of the typical "cruciform" cross section,

and dendritic side branching. Dendrite arm spacing generally increased with increasing alloy content.

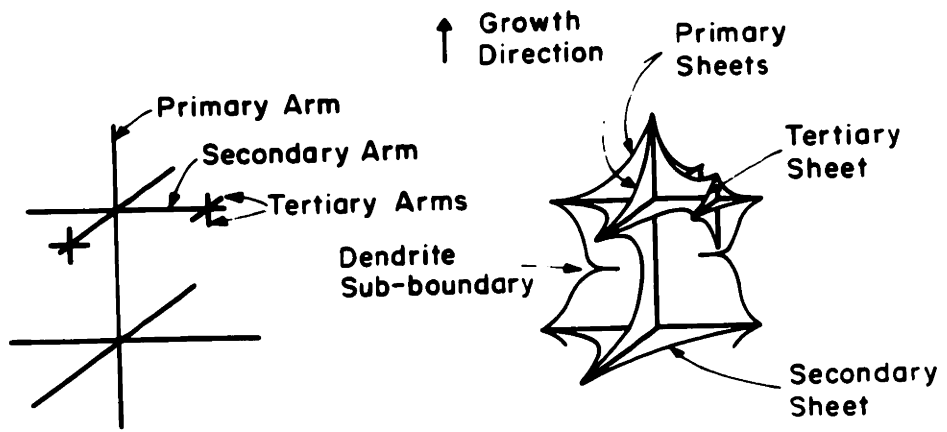
Addition of carbon (.12 per cent to .42 per cent) strongly influenced the dendritic structure. The carbon increased the primary and secondary dendrite arm spacings appreciably and resulted in dendrites with higher-order growth forms at a given cooling rate than in the carbon free alloy.

Iron-phosphorus alloys have strong dendrite forming tendencies as secondary growth was observed adjacent to the chill surface. The iron-phosphorus alloy more closely resembled the iron-nickel-carbon alloys in forming higher-order growth forms while the iron-copper alloy was similar to the iron-nickel group.

Results of the dendrite arm spacing data, d , and solidification times, θ_f , and/or distance from the chill, X , indicate that values of n are close to 0.5 so that little variation in microsegregation is predicted with varying cooling rate—distance from the chill.



(a)



(b)

Figure 5-1. Schematic diagram of growth forms and their terminology.

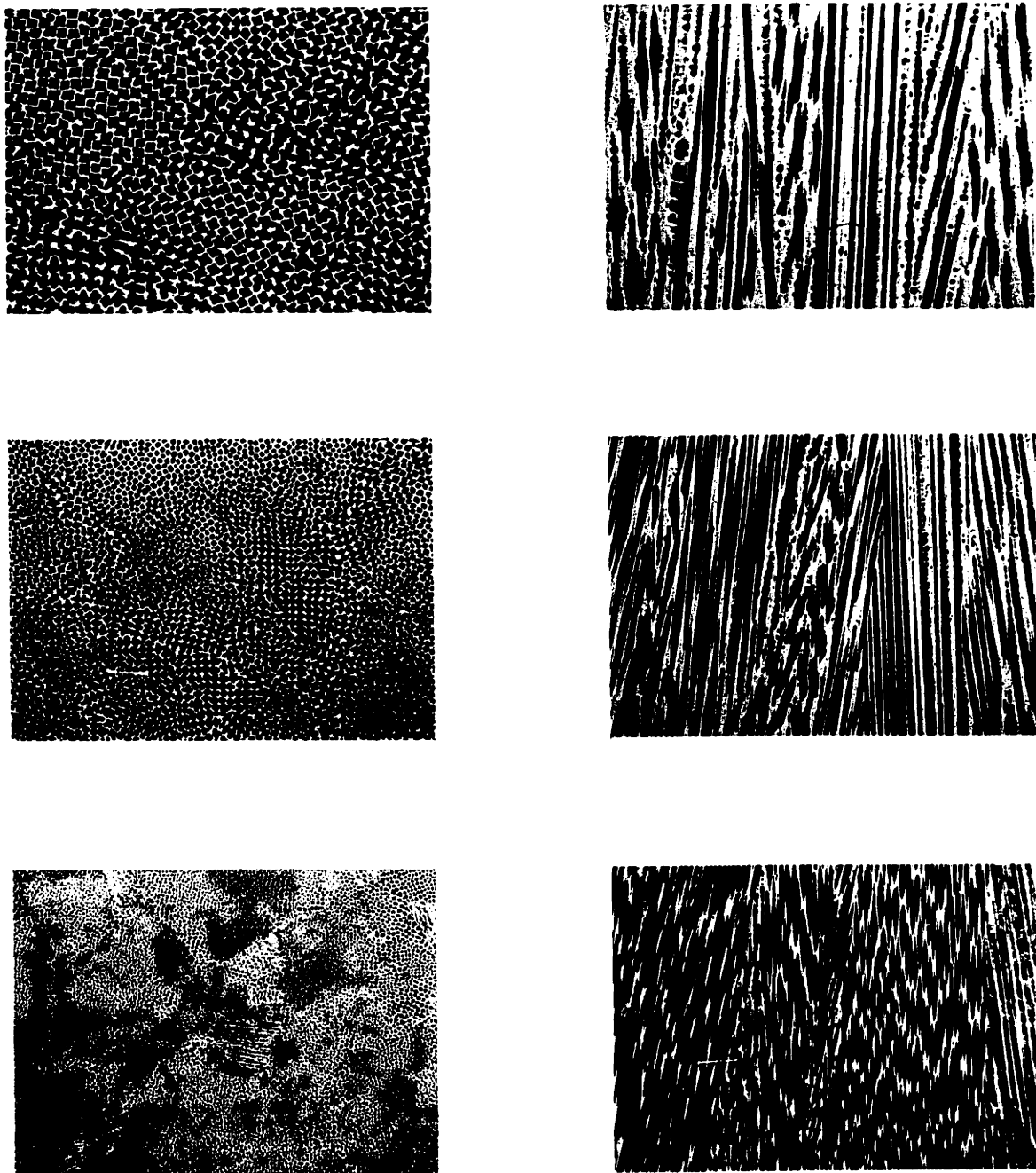


Figure 5-2 Iron-10 per cent nickel alloy. Photomicrographs at 1", 2", and 4" from the chill. Casting 1, 7.6X.

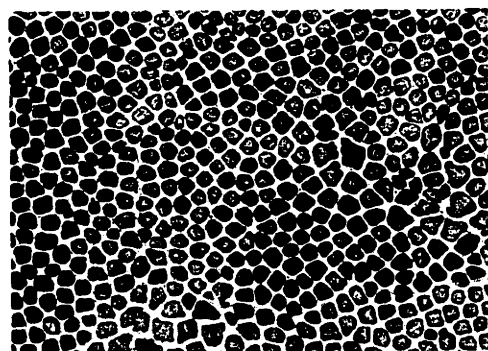
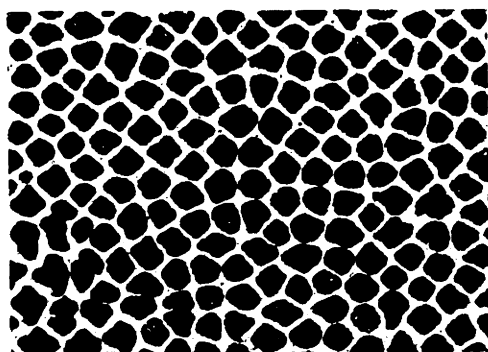


Figure 5-3 Iron-10 per cent nickel alloy. Photomicrographs at 1", 2", and 4" from the chill. Casting 1, 34X.

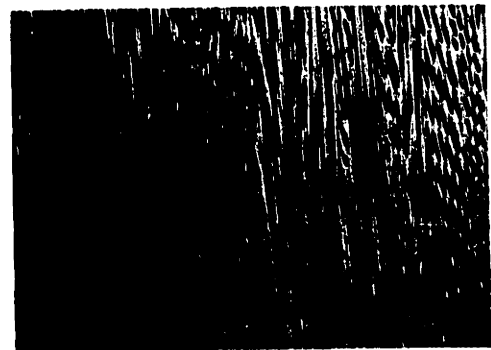
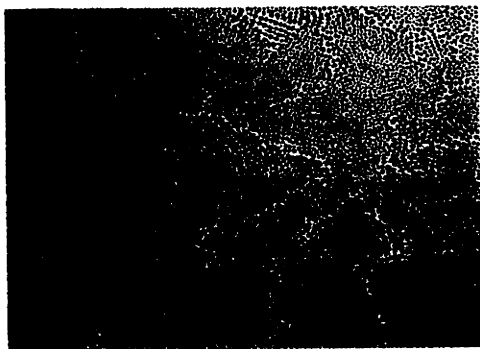
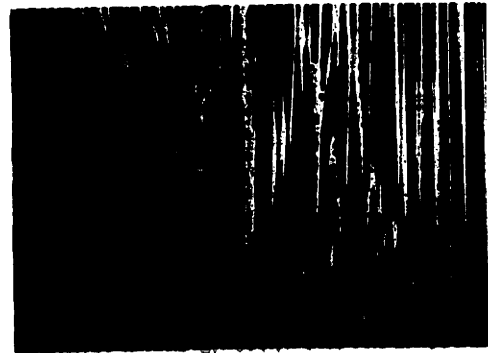
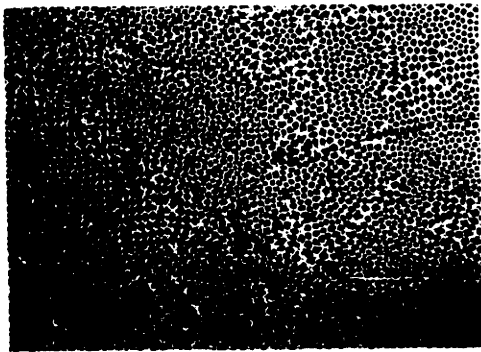
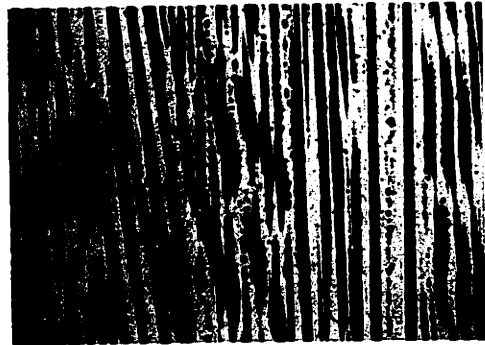
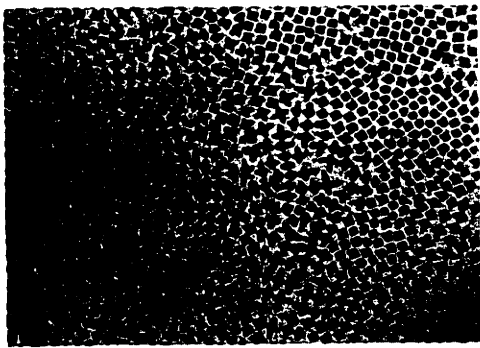


Figure 5-4 Iron-15 per cent nickel alloy. Photomicrographs at 1", 2", and 4" from the chill. Casting 2, 7.6X.

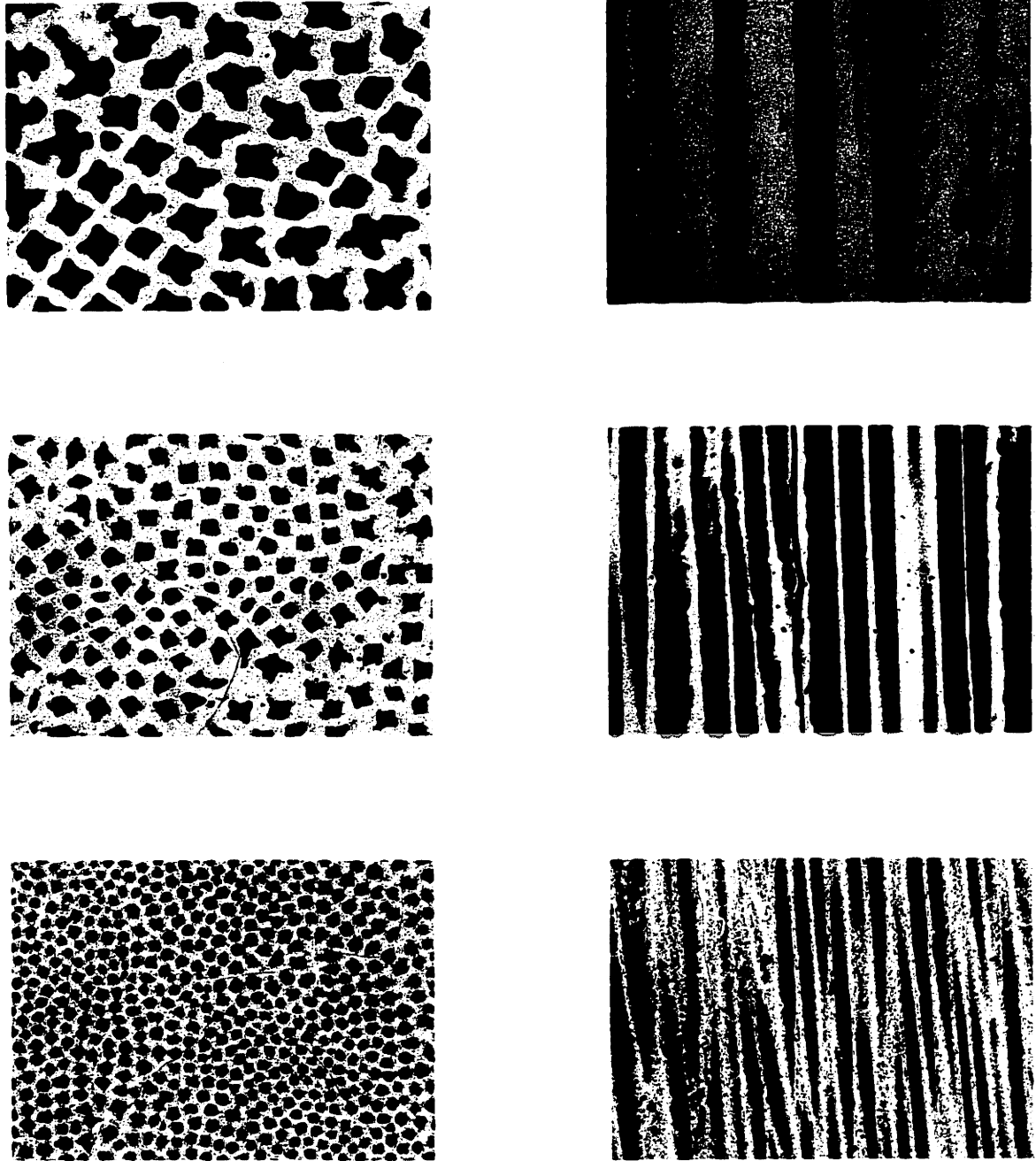


Figure 5-5 Iron-15 per cent nickel alloy. Photomicrographs at 1", 2", and 4" from the chill. Casting 2, 34X.

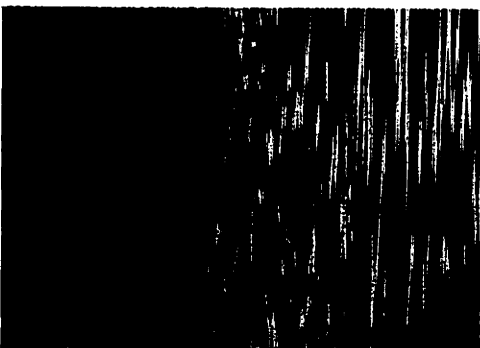
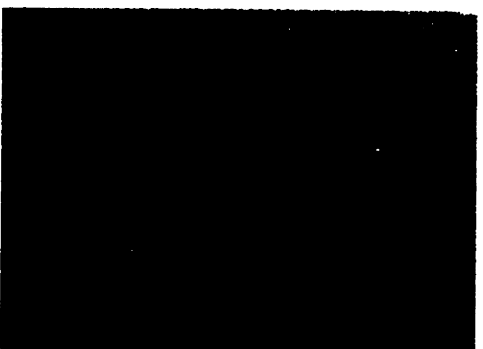
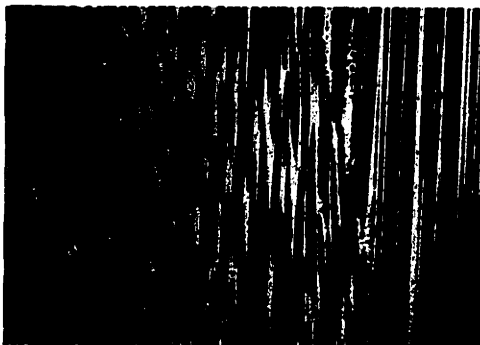
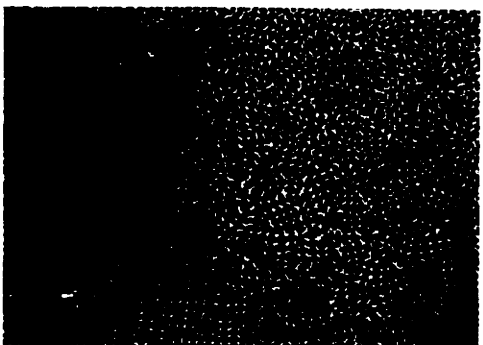
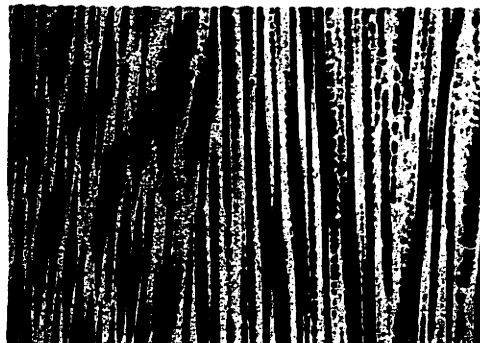
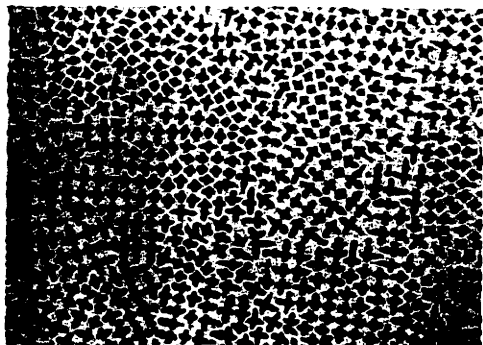


Figure 5-6 Iron-20 per cent nickel alloy. Photomicrographs at 1", 2", and 4" from the chill. Casting 3, 7.6X.

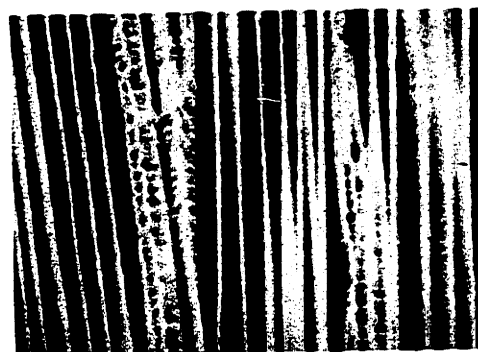
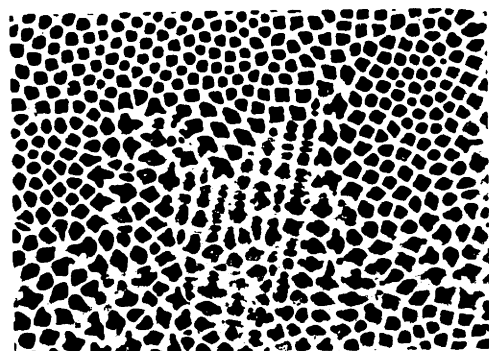
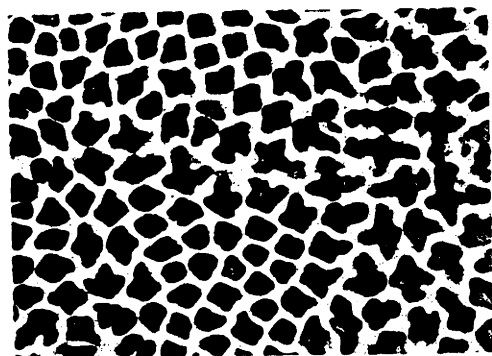
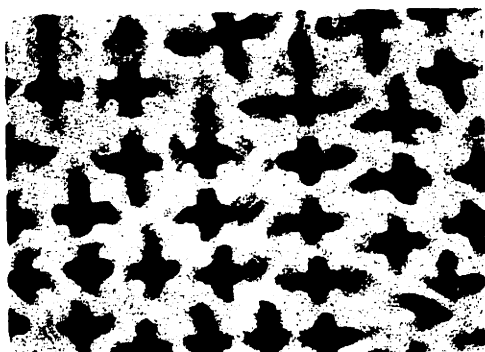


Figure 5-7 Iron-20 per cent nickel alloy. Photomicrographs at 1", 2", and 4" from the chill. Casting 3, 34X.

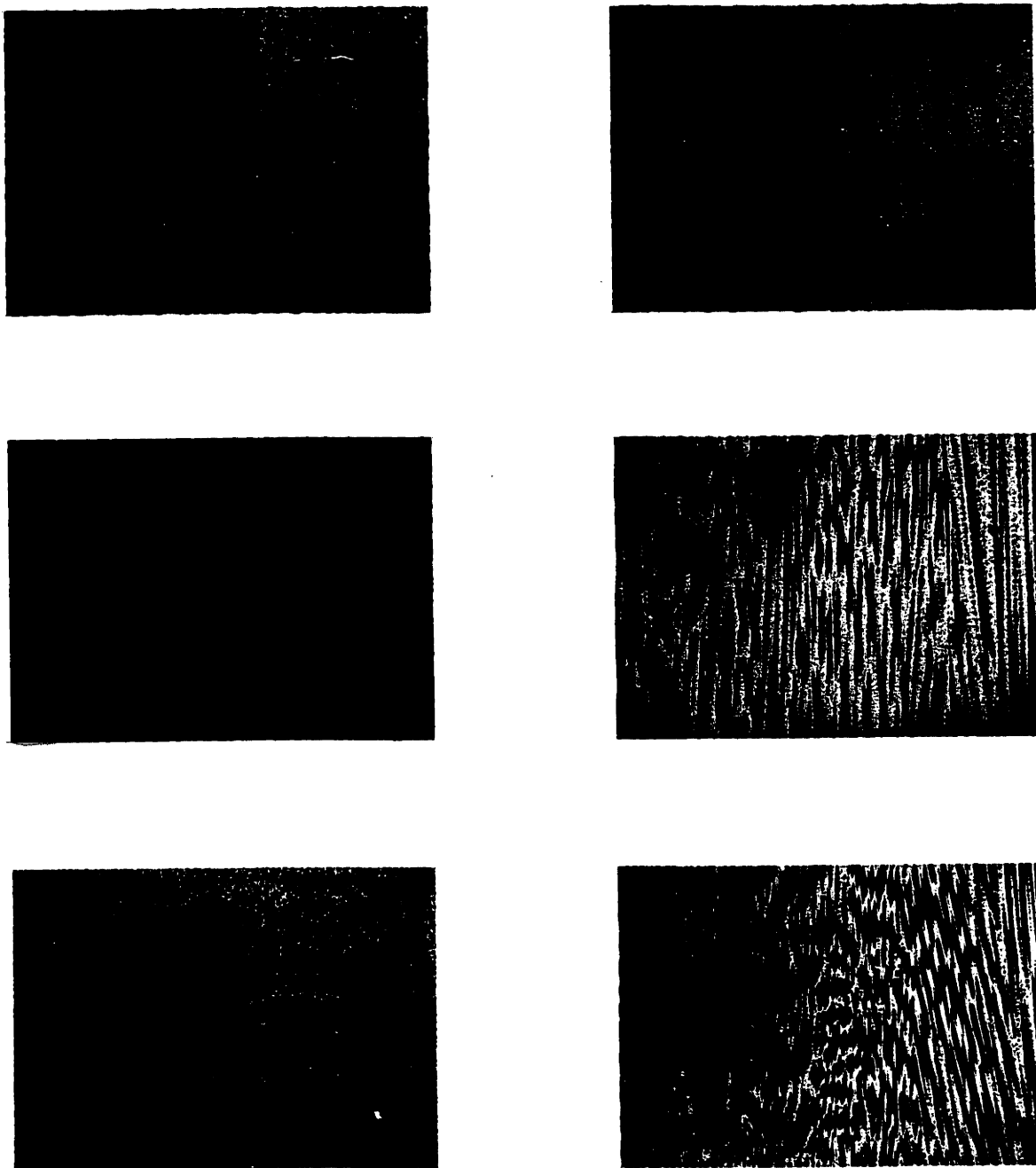


Figure 5-8 Iron-26 per cent nickel alloy. Photomicrographs at 1", 2", and 4" from the chill. Casting 4, 7.6X.

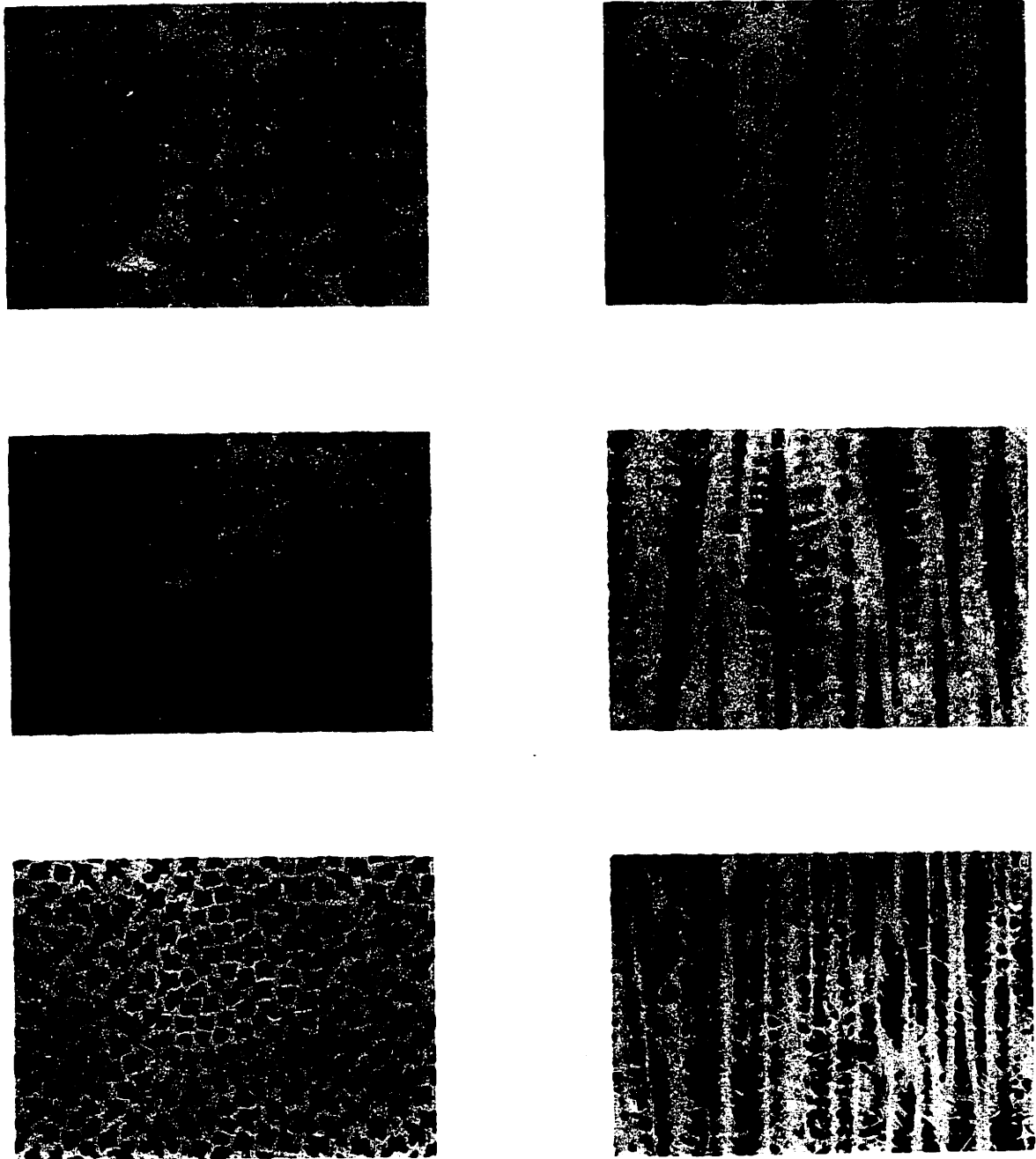


Figure 5-9 Iron-25 per cent nickel alloy. Photomicrographs at 1", 2", and 4" from the chill. Casting 4, 34X.

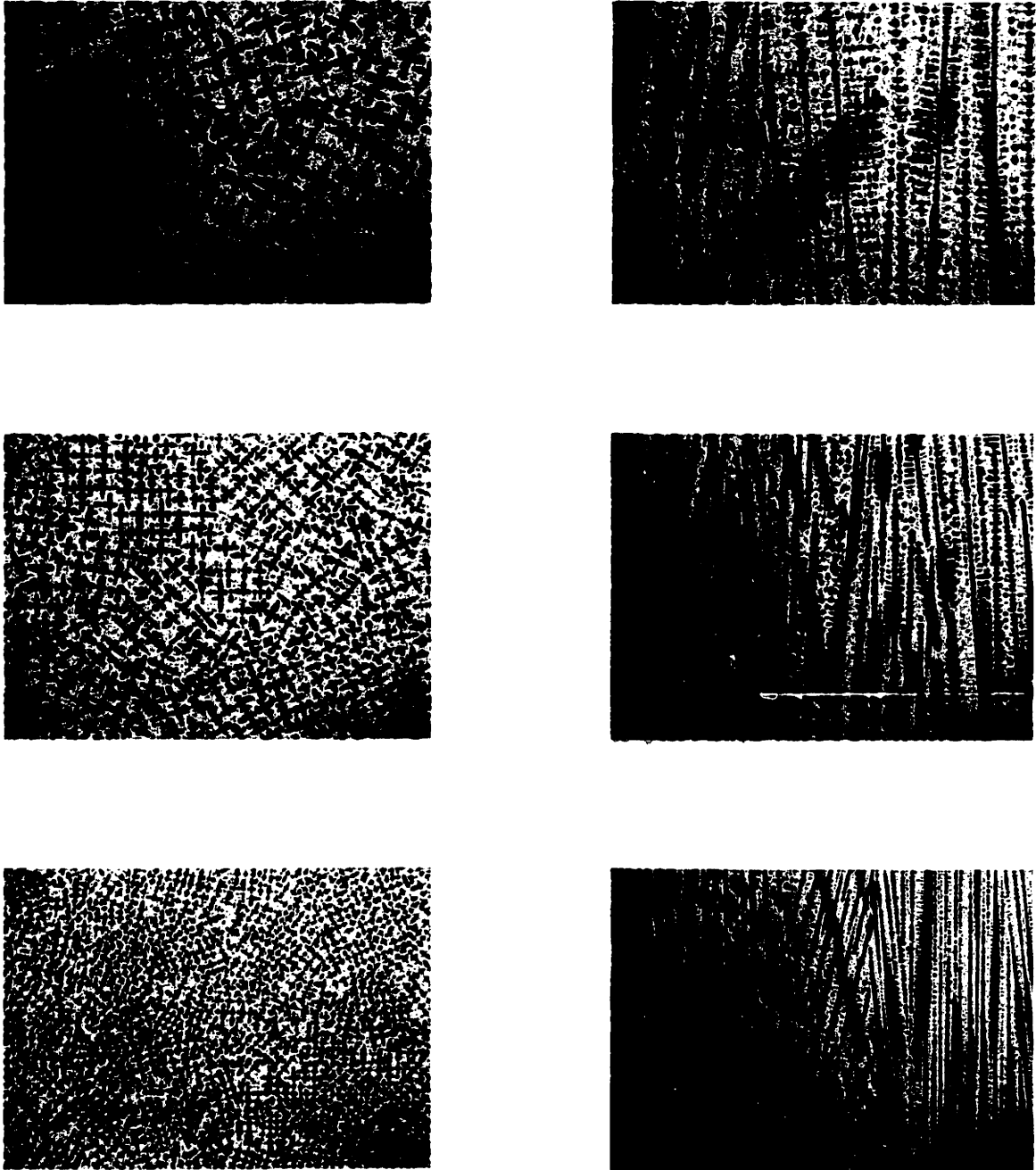


Figure 5-10 Iron-26 per cent nickel-0.12 per cent carbon alloy. Photomicrographs at 1", 2", and 4" from the chill. Casting 5, 7.6X.

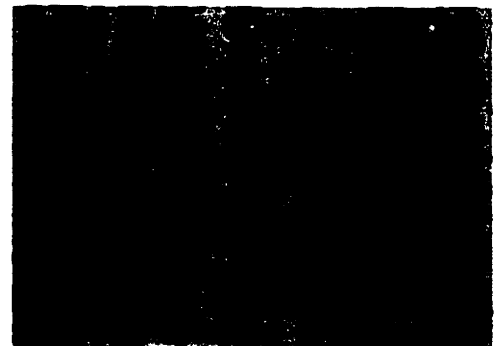
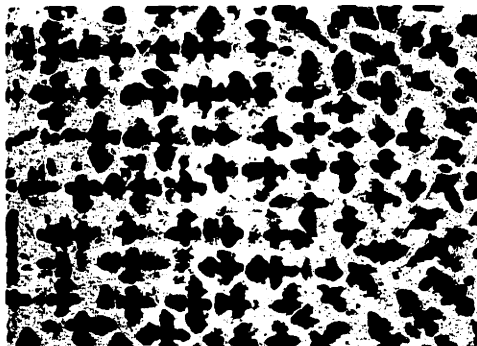
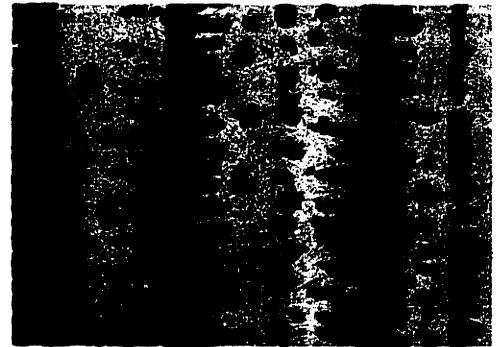
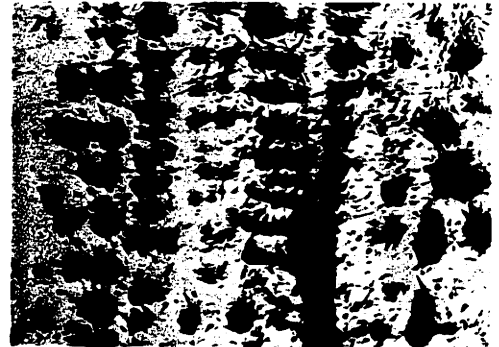


Figure 5-11 Iron-26 per cent nickel-0.12 per cent carbon alloy. Photomicrographs at 1", 2", and 4" from the chill. Casting 5, 34X.

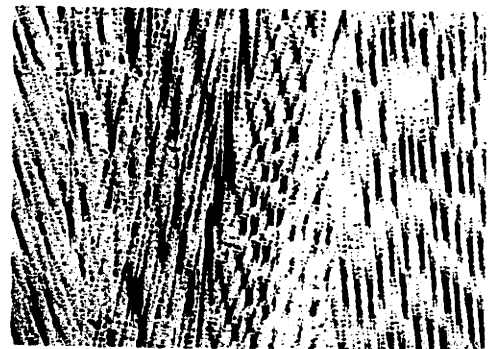
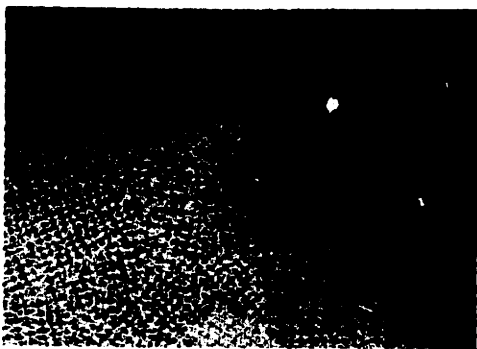
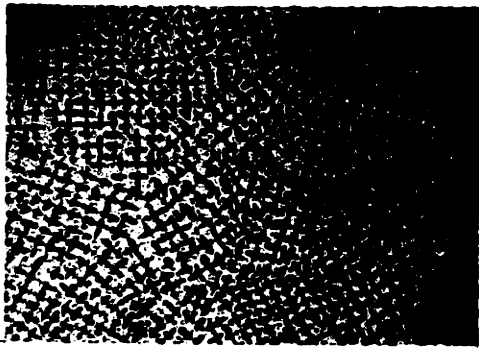
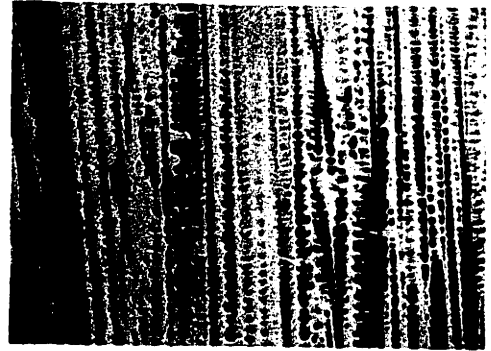
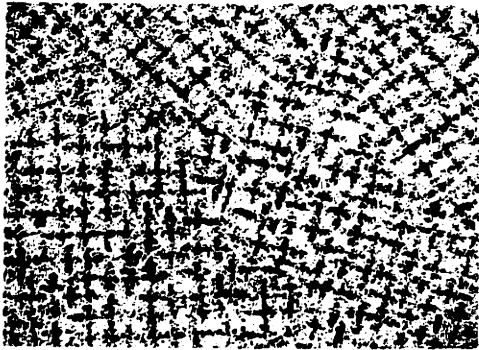


Figure 5-12 Iron-26 per cent nickel-0.33 per cent carbon alloy. Photomicrographs at 1", 2", and 4" from the chill. Casting 6, 7.6X.

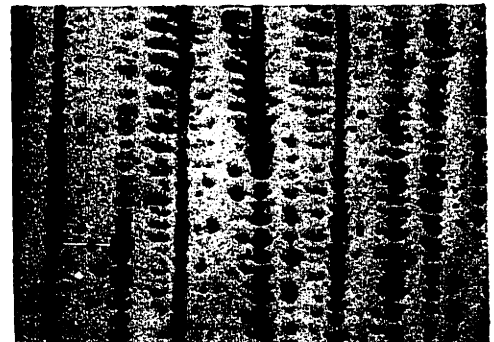
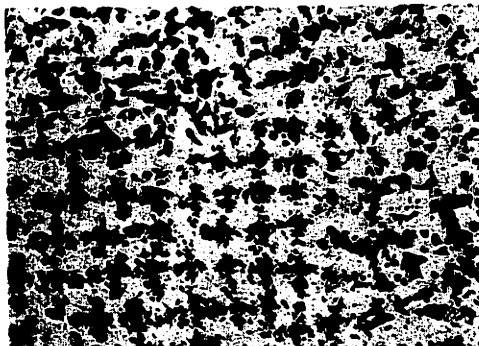
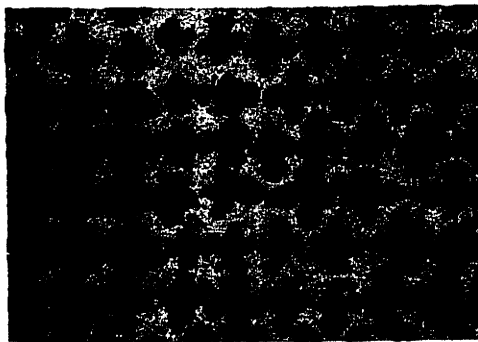
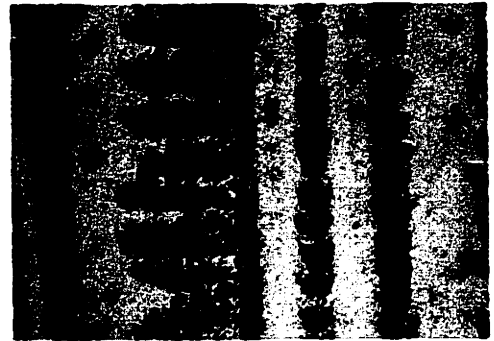
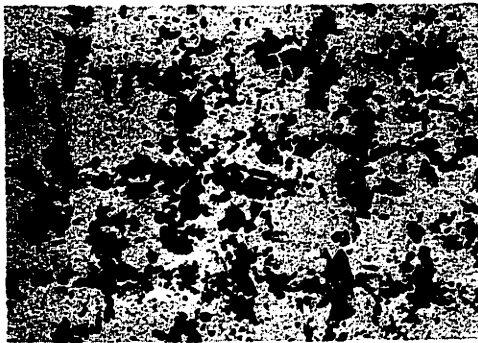


Figure 5-13 Iron-26 per cent nickel-0.33 per cent carbon alloy. Photomicrographs at 1", 2", and 4" from the chill. Casting 6, 34X.

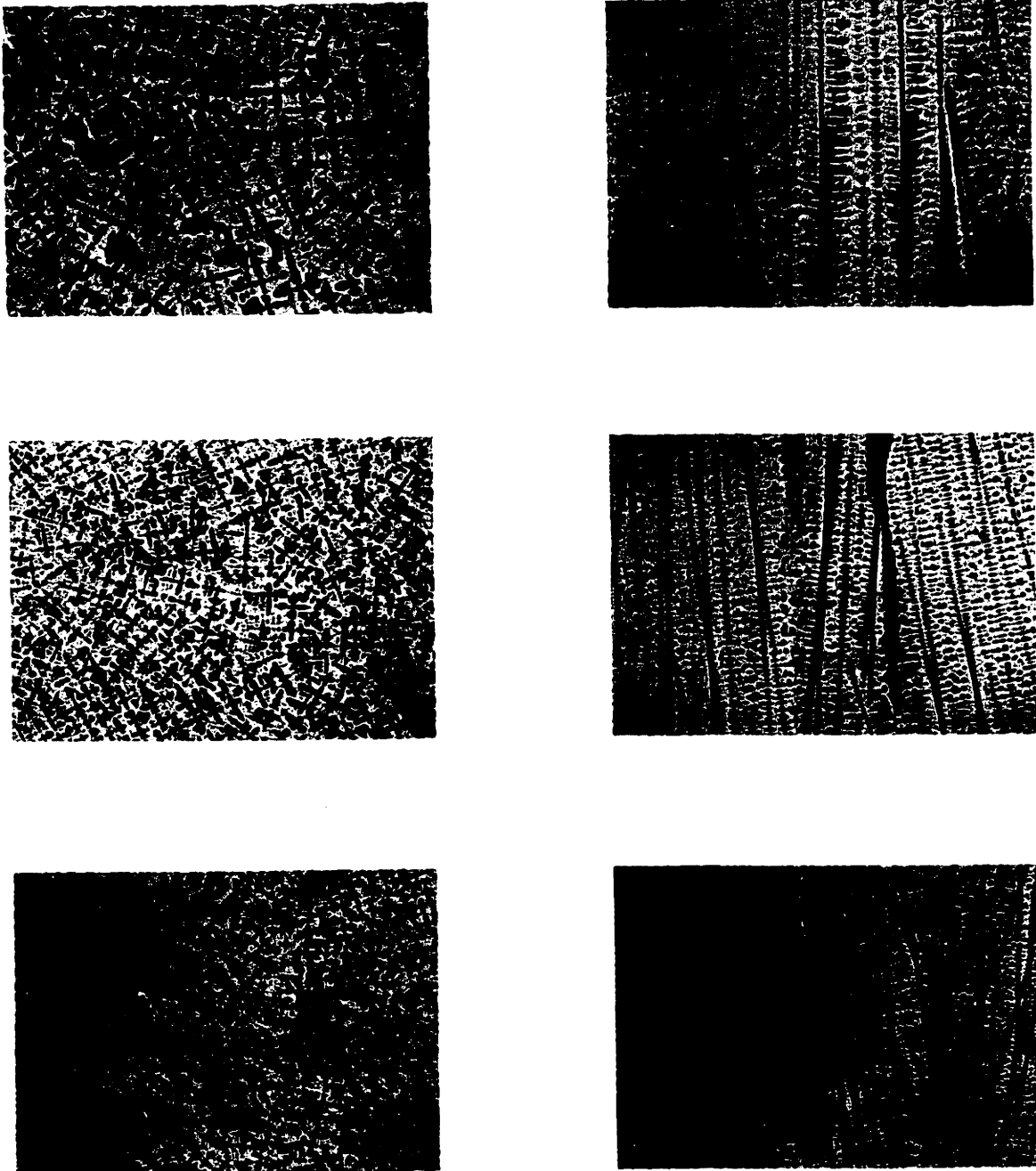


Figure 5-14 Iron-26 per cent nickel-0.42 per cent carbon alloy. Photomicrographs at 1", 2", and 4" from the chill. Casting 7, 7.6X.

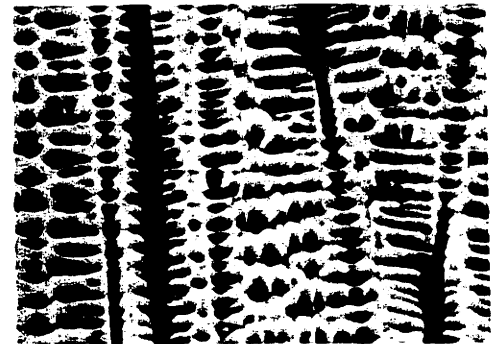
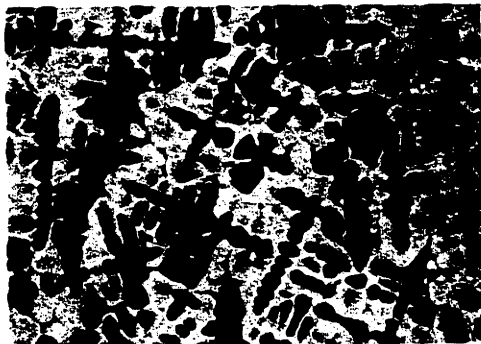
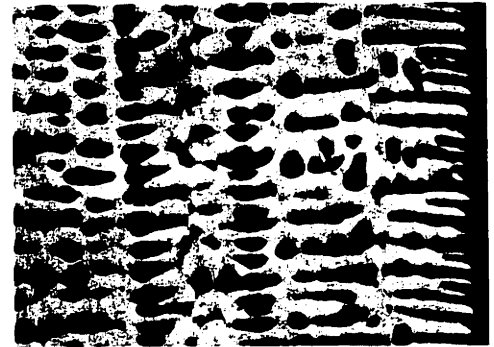
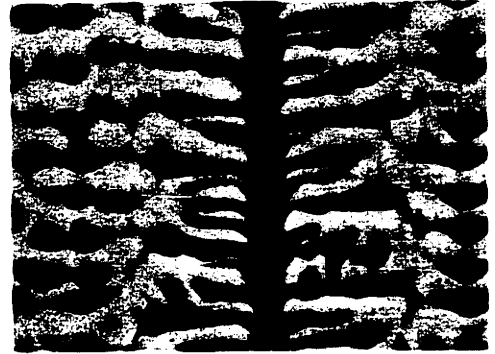


Figure 5-15 Iron-26 per cent nickel-0.42 per cent carbon alloy. Photomicrographs at 1", 2", and 4" from the chill. Casting 7, 34X.

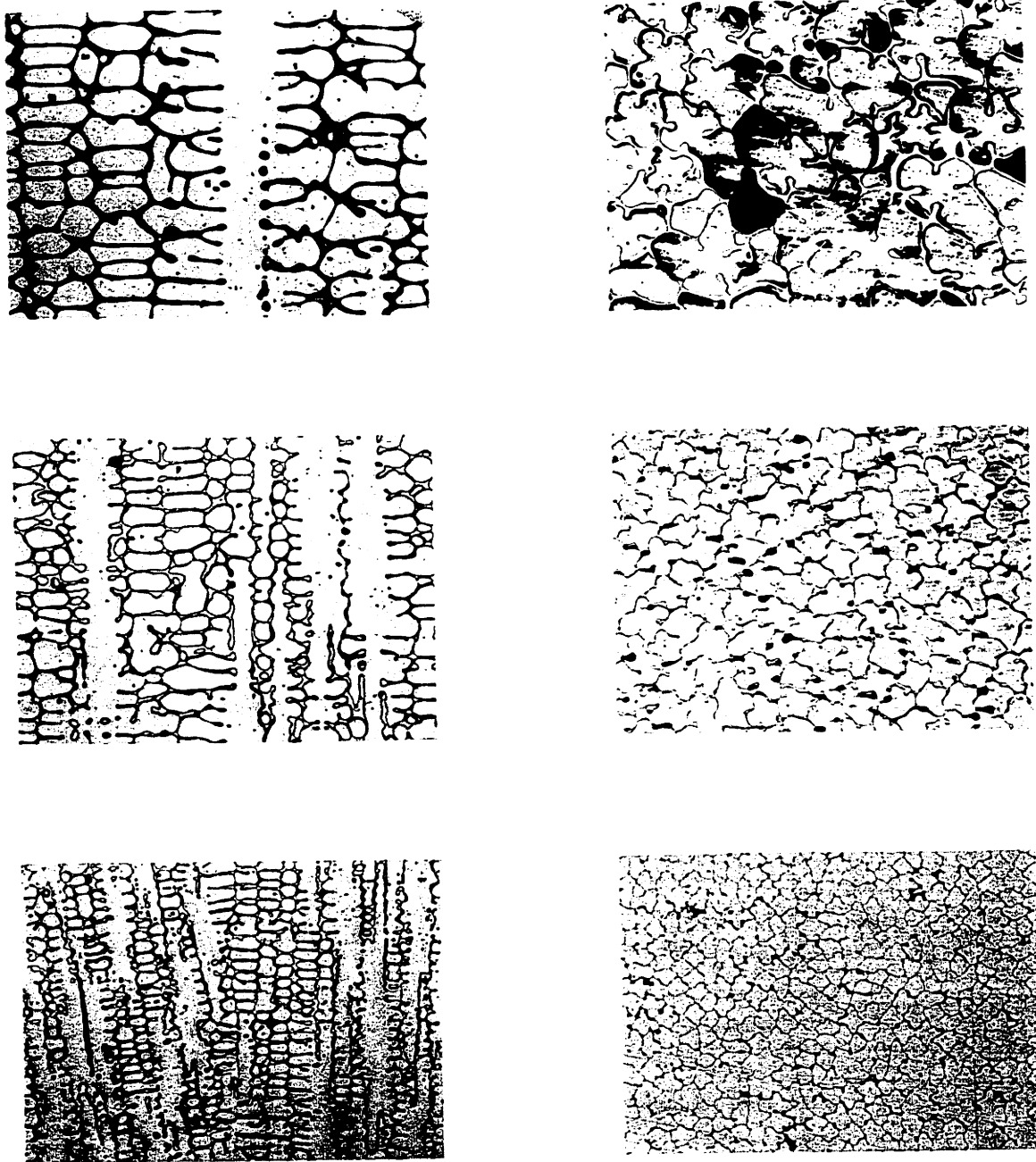


Figure 5-16 Iron-25 per cent copper alloy. Photomicrographs at 1", 2" and 4" from the chill. Casting 9, 64X.

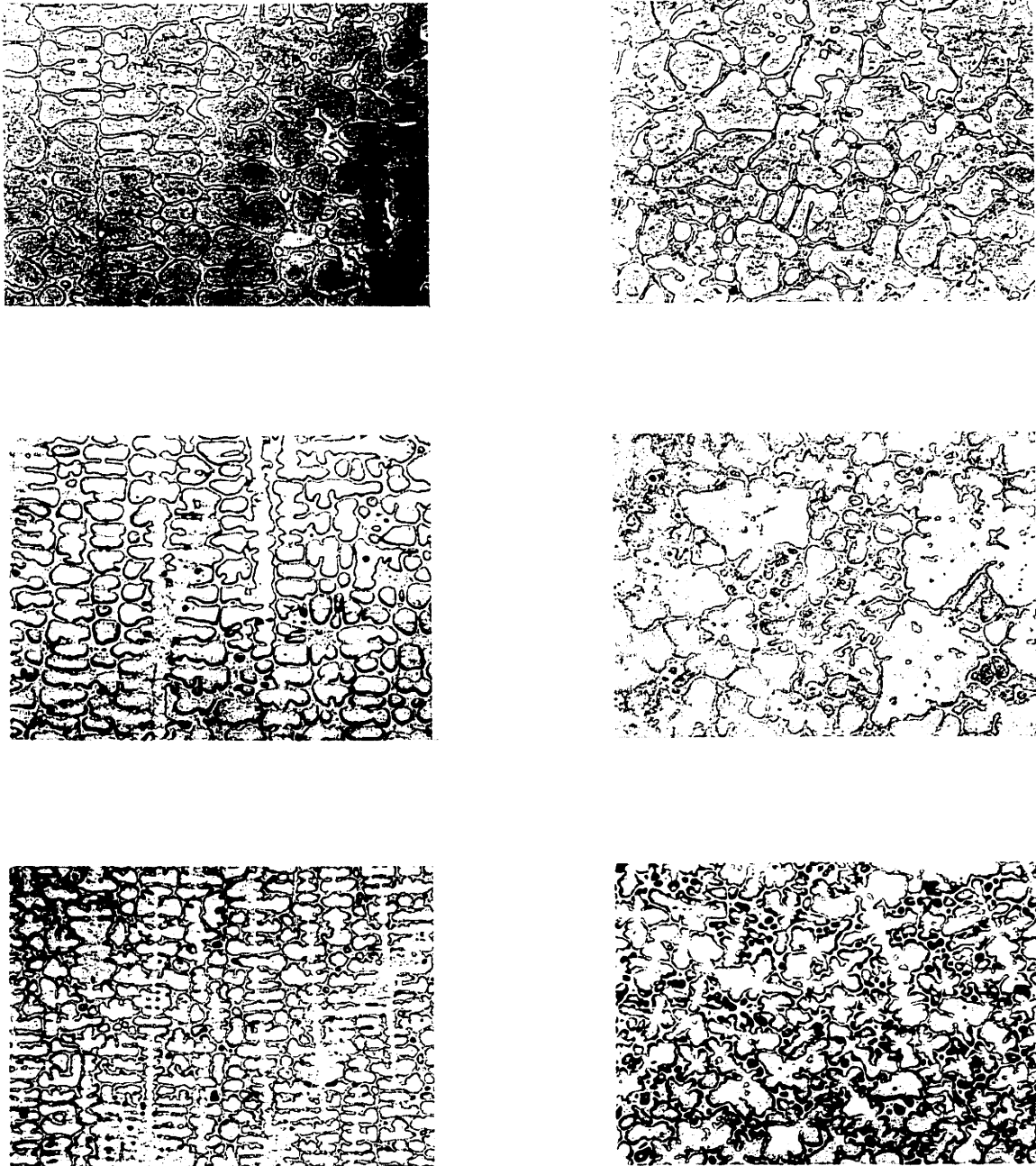


Figure 5-17 Iron-4 per cent phosphorus alloy. Photomicrographs at 1", 2" and 4" from the chill. Casting 10, 34X.

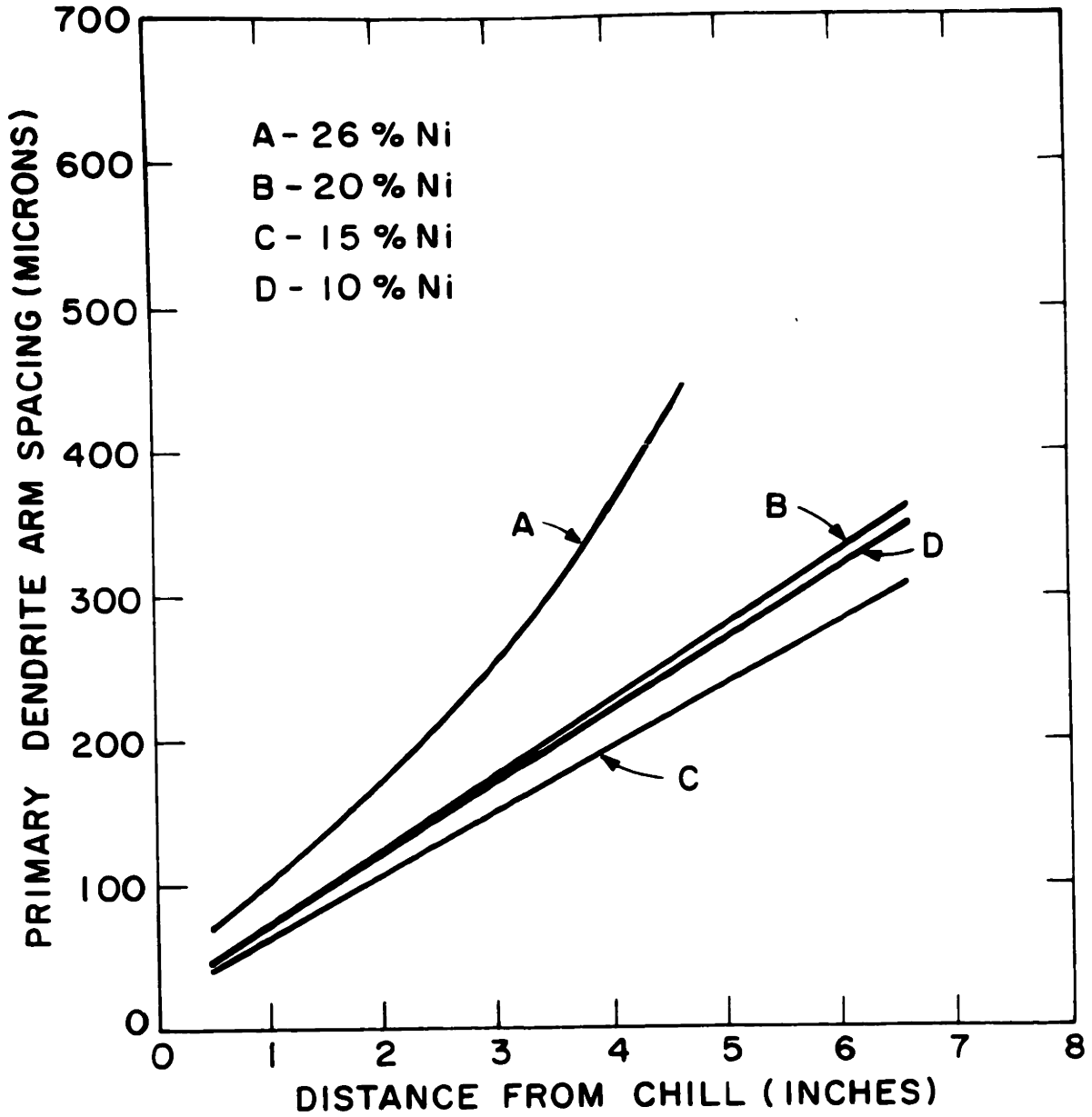


Figure 5-18. Primary dendrite arm spacing versus distance from the chill for binary iron-nickel alloys containing from 10 to 26 per cent nickel.

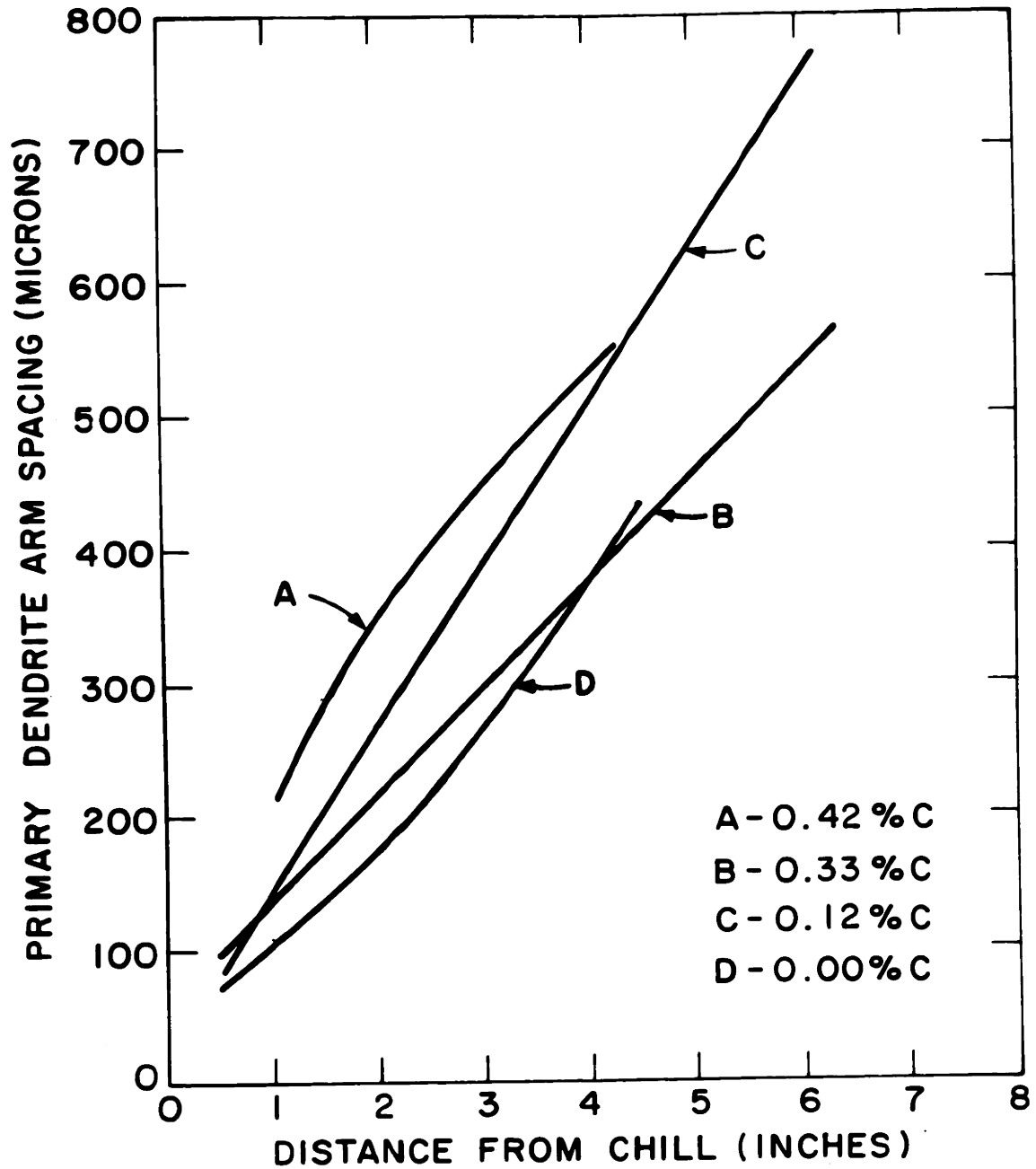


Figure 5-19. Primary dendrite arm spacing versus distance from the chill for ternary iron-nickel-carbon alloys containing 26 per cent nickel and from 0 to .42 per cent carbon.

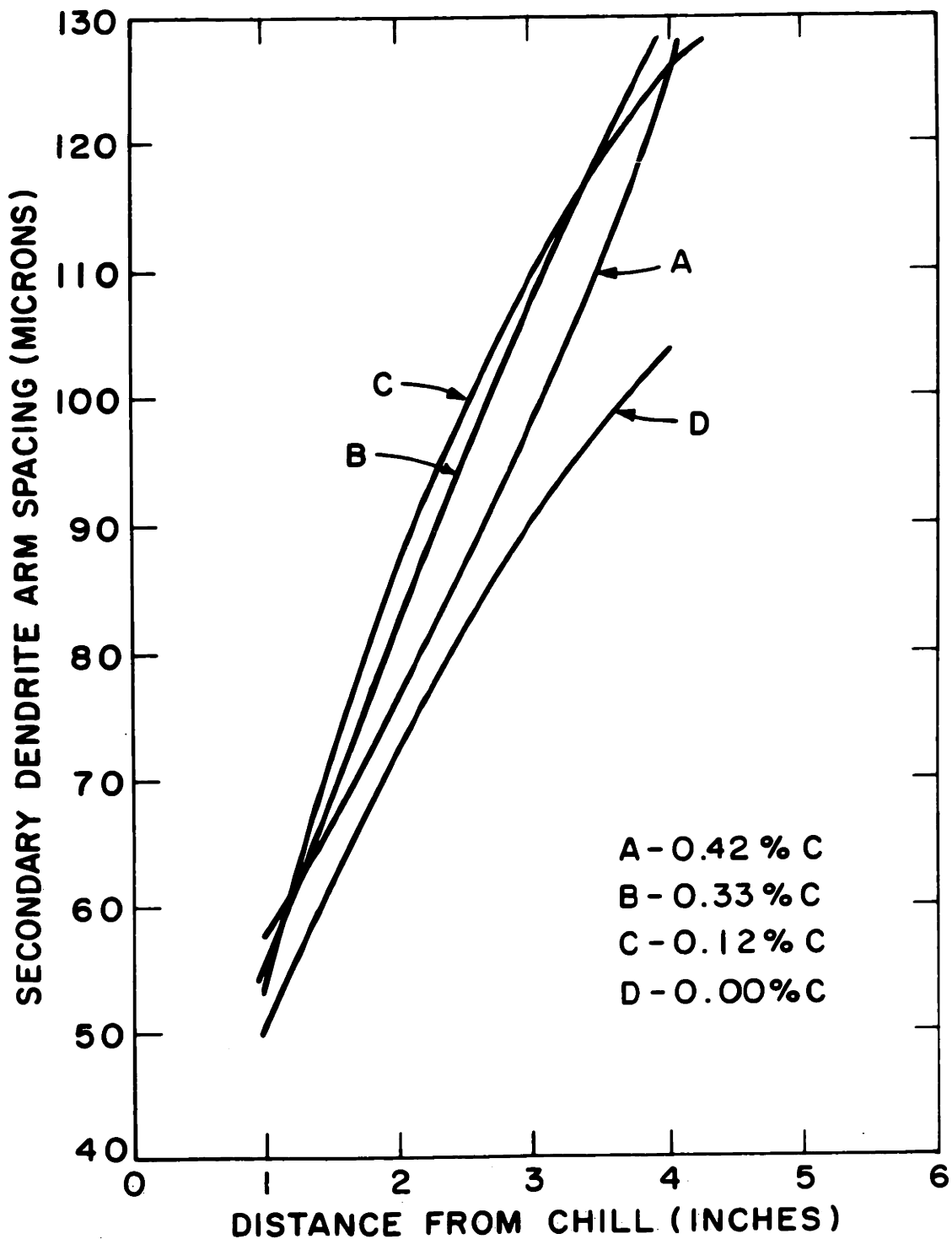


Figure 5-20 Secondary dendrite arm spacing versus distance from the chill for iron-nickel-carbon alloys, containing nominally 26 per cent nickel and from 0 to .42 per cent carbon.

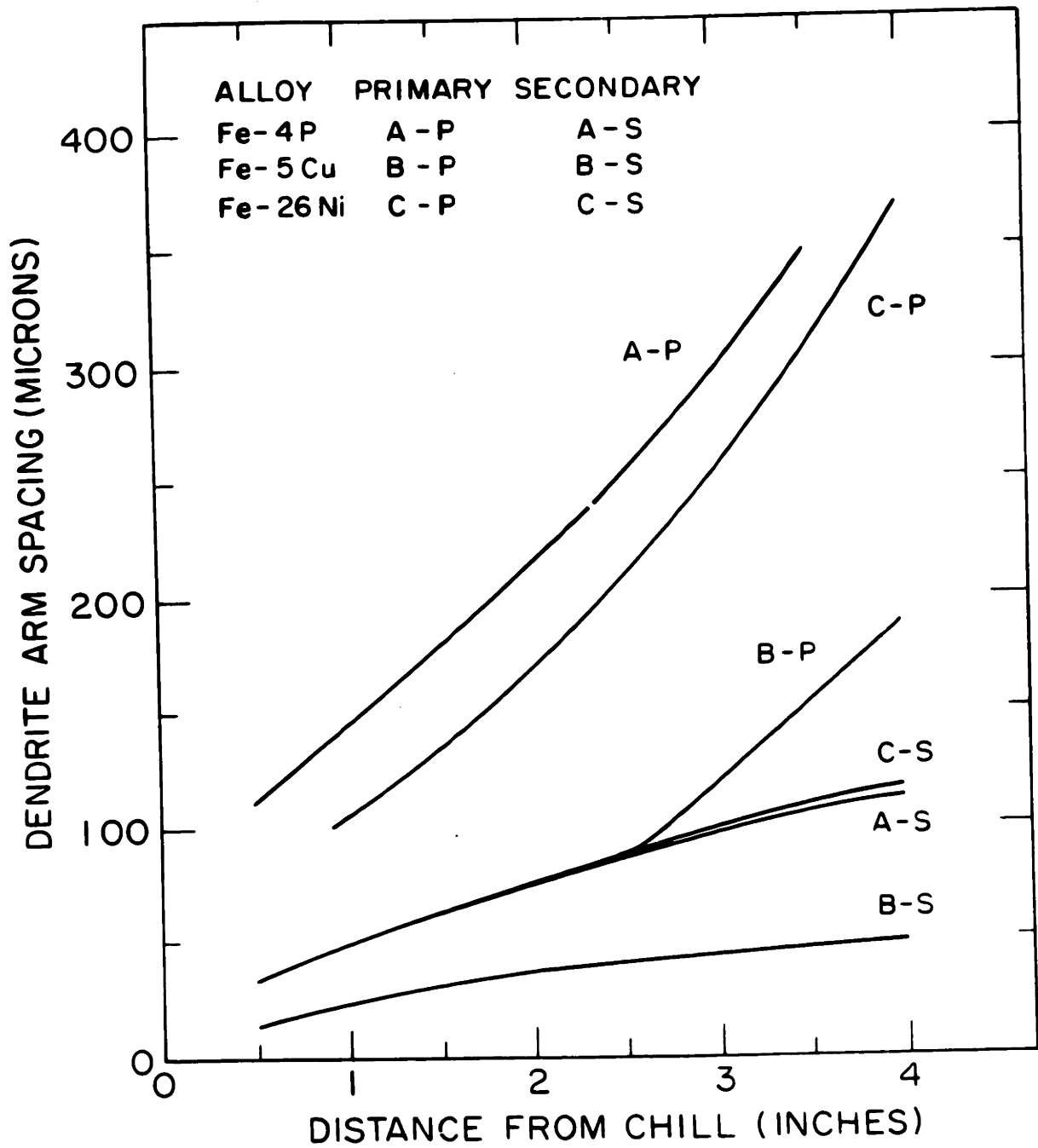


Figure 5-21. Primary and secondary dendrite arm spacing versus distance from the chill for binary iron-4.0 per cent phosphorus, iron-25 per cent copper and iron-26 per cent nickel.

VI. MEASUREMENTS OF MICROSEGREGATION IN IRON-BASE ALLOYS

A. Procedure

The chemical segregation existing in the binary iron-26 per cent nickel casting, iron-10 per cent nickel, and iron-phosphorus alloys was determined experimentally by electron microprobe analysis. Microprobe traces were made on samples taken in a plane perpendicular to the primary growth direction (parallel to the chill surface). The maximum and minimum solute values were measured, the segregation ratios calculated, and a number of composition deviation indices measured.

1. Electron microprobe measurements

Microscopic chemical analyses were performed on either of the following commercial electron microprobe units:

- (a) Applied Research Electron Microprobe Analyzer with two 52.5° take-off angle spectrometers.
- (b) North American Phillips Microprobe with a single 15° take-off angle spectrometer.

To obtain values of C_M^0 and C_m^0 metallographic samples were etched and microhardness marks made as references. The samples were lightly polished to remove the etched surface and then probed. Probe paths were chosen parallel to the cross arms forming the central portion of the dendrite. Since the maxi-

mum solute content may deviate from the center of the interdendritic region, the initial path was hand scanned until a maximum was reached; then at this point a path perpendicular to the original was run to find a maximum in this path. Orthogonal paths were continually made at each maximum until the actual maximum was determined. A similar scanning process was used for obtaining C'_m . This procedure is identical to that used by Kattamis.¹¹

For the 26 per cent nickel series, iron and nickel contents were determined simultaneously on the ARL probe, thus providing a means of distinguishing the true minimum nickel values from low nickel readings caused by pores or inclusions. A set of standards of known chemical compositions including samples of pure iron and pure nickel were run prior to probing each specimen. A check for probe stability was made by at least running the pure nickel and pure iron after each specimen and allowing no more than a 5 per cent drift in intensity. When two or more specimens were run, the standards were run alternately to provide good working curves in addition to checking for probe stability.

A fixed 30 second accumulation time, which amassed a total of between 20,000 and 40,000 counts for the unknown, was used in combination with scanning steps varying from 2 to 8 microns depending on the concentration gradient. The minimums in all cases had more shallow gradients than the maximums, permitting

the use of larger scanning steps. Maximum and minimum values were determined in several positions within the sample.

The iron-10 per cent nickel and iron-phosphorus alloys were run on the Norelco probe. The intensity of the Ni $K\alpha$ line was both point counted and recorded continuously while traversing the specimen to obtain maxima and minima. The intensity ratios measured were converted to weight fractions using the empirical technique developed by Ziebold.³¹

The iron phosphorus measurements were obtained by measuring the intensity of the P $K\alpha$ line following the same experimental procedure used for iron-10 per cent nickel alloy, of point counting and continuous recording. The intensity readings for the iron phosphorus alloy were converted to weight fraction based on the intensity of an iron-nickel-15 weight per cent standard and a linear relationship between intensity ratio and composition.

The composition deviation index, σ_m^0 , was measured for all samples on the Norelco probe. Several long scans across the sample were made, plotting on the chart paper composition (intensity) versus distance. Then isoconcentration lines were drawn on the chart, the fraction of the distance with a composition on or below the isoconcentration line was recorded, and a cumulative frequency plot made, composition versus volume fraction. The composition deviation index was defined, accord-

ing to equation (10), as $\frac{2}{C_0}$ times the area enveloped by the isoconcentration line at C_0 and the distribution curve between the ordinate and the point where the distribution curve reached C_0 .

2. Quantitative Metallography

The volume per cent eutectic in the iron-phosphorus system was found metallographically using a Two Dimensional Systematic Point Count Analysis. Using this method a polished and etched surface was projected on the ground glass screen of a metallograph at 50X. A grid of 63 points was placed over the field of view, and the number of points that fell on the eutectic phase were counted. Between 30 to 60 grid positions were counted for each sample so that between 2000 to 4000 counts were amassed. The ratio of points falling on eutectic to the total number of points yields the volume fraction eutectic. Error was approximated using the technique of Hilliard and Cahn²⁹ and is included with the results.

B. Microprobe Results and Comparison with Theory

Iron-Nickel System

Segregation Ratios

Results of the electron microprobe analysis are listed in Table 6-1. Minima (at the center of dendrite arms) were essentially constant at locations from 1/2 inch to 4 inches from the chill. In the 26 per cent nickel alloy maxima (at interdendritic

regions) decreased slightly with increasing distance from the chill and so segregation ratio, S° , decreased also.

The minimum nickel values in Table 6-1 are significantly higher than those estimated by the equilibrium phase diagram for alloys of 10 per cent nickel ($C_m^{\circ} = 5.7$ per cent nickel) or 26 per cent nickel ($C_m^{\circ} = 19.3$ per cent nickel). This deviation must be due to solid state diffusion which occurs both during solidification and while cooling to room temperature. Comparing segregation ratios rather than maximum and minimum compositions minimizes overall chemistry variations (C'_s) from the different heats. Specifically, comparison is made of measured segregation ratios, S_e° , with calculated segregation ratios, S_c° , as determined from Figure 2-19 and 2-20. As in the previous ASFD analysis⁶ the MBT method provides qualitative agreement with the experimental results but a correction factor, g , is necessary to obtain quantitative agreement. This factor compensates for factors such as kinetics, data inaccuracy, multi-dimensional diffusion, and model geometry.

Correction factors were first calculated for the iron-26 per cent nickel and the iron-10 per cent nickel alloys individually for both plate and cylinder models. The resulting correction factors are listed in Table 6-2. Because of the excellent agreement between the correction factors, an average value was used for each geometry in calculating the segregation ratios. Results for two cases are listed in Table 6-3 for an

iron-26 per cent nickel alloy using the Mass Balance Technique - plate model, and Table 6-4 for an iron-10 per cent nickel alloy using the Mass Balance Technique - cylinder model. The original development of a cylinder model was prompted by the rod-like cellular morphology exhibited in the iron-10 per cent nickel alloy and discussed in Chapter V.

In spite of the radical difference in morphology, the correction factors for the 26 per cent and 10 per cent nickel alloys were in excellent agreement. Three possible explanations are (a) that other characteristics of the material besides diffusivity, phase relationships, dendrite arm spacing, and solidification time play an important role in determining solute redistribution, (b) that these variables may need to be measured more accurately, and (c) that geometry does not play a major role in solute redistribution.

The reason for the necessity of any correction factor is probably due to data inaccuracy. For example, the high temperature diffusion data, which is an extrapolation of data measured at temperatures below the solidification range, might not be valid. This would be so if many vacancies were quenched into the solid during the transformation and resulted in a high diffusivity until the excess vacancies were eliminated. Any phenomena such as this would necessitate the introduction of a correction factor to obtain quantitative agreement.

For both the iron-26 per cent nickel and iron-10 per cent nickel alloys, the dendrite spacing is very nearly proportional to solidification time to the 0.5 power and, in agreement with theory, the segregation ratio changes only slowly with distance from the chill.

The Effect of Carbon on the Segregation Ratio of Iron-Nickel.

Measurements of segregation ratios were made on two iron-26 per cent nickel alloys to which additions of .33 and .42 carbon had been made. Specimens were taken 2 inches from the chill, to determine the effect of carbon on the nickel distribution. The results are listed in Table 6-5 and show a decrease in the segregation ratio with increasing carbon content. Thus the addition of carbon enhanced homogeneity in the samples tested.

Composition Deviation Index

The composition deviation index was measured for three of the iron-10 per cent nickel specimens taken 1/2, 1, and 2 inches from the chill and the iron-26 per cent nickel which was 2 inches from the chill. The results of the measurements and those predicted theoretically for the MBT plate are listed in Table 6-5. Plots of the composition deviation index as a function of n as calculated by the Mass Balance Technique are shown for the 26 per cent nickel alloy in Figure 2-21 and for a 10 per cent nickel alloy in Figure 2-22.

The calculated values for the composition deviation index at n/c (where n is the value of n that gives the experimental value of the segregation ratio), are larger in each case. The reason for this is that the correction factor is based on the segregation ratio which is determined only by the maximum and minimum solute contents and not the shape of the curve. The measured shape and that predicted at room temperature are different. A typical measured curve, Figure 6-1, does not exhibit the same shallow slope predicted by the analyses at either high or low volume fractions, thus the discrepancy in σ_m^0 s for identical segregation ratios.

The results suggest that further work would be useful in the development of this parameter and to determine the reasons for the shape of the observed curve.

Iron-Phosphorus System

The amount of eutectic in the iron phosphorus alloy was measured at various distances from the chill and the results listed in Table 6-6.

In agreement with theory, the eutectic measurements at different distances from the chill do not vary significantly. The minimum alloy content values, C_m^0 , were also measured and are listed in Table 6-7. Again, these do not vary significantly, agreeing with the theory

The wet chemical analyses of the iron-phosphorus alloy, listed in Table 6-8, are not as consistent as one would expect. The explanation for this variation was not obvious metallographically, e.g., as segregation in the form of nonuniformly distributed eutectic. For this reason the computer programs were run for both 3.5, Figure 2-23, and 4.0, Figure 2-24, per cent phosphorus. The amount of eutectic measured metallographically, when combined with the Mass Balance Technique - plate model predictions of n versus weight per cent eutectic for the 4.0 per cent phosphorus alloy, predict an n of 6×10^6 sec/cm² for an alloy containing 28 volume per cent (26 weight per cent) eutectic. For the 3.5 per cent alloy MBT results predict less than 26 weight per cent eutectic even for nonequilibrium solidification - no diffusion in the solid. Based on this, the wet chemical results, and overall chemical analyses made with the electron microprobe, the alloy will be assumed to contain 4 per cent

phosphorus. The minimum solute content predicted by the Mass Balance Technique - plate model for an n of 6×10^6 sec/cm² is 1.36 weight per cent phosphorus. This is lower than the experimentally measured values listed in Table 6-8. Taking into account the fact that the overall estimates of alloy composition found on the probe are higher than the wet chemical analyses and the possible experimental error which may be encountered in electron beam microprobe analysis, the experimental measurement is not too different from that predicted by the computer analysis. Conversely for a 4 per cent phosphorus alloy the n for C_m^0 equals 2.0 is 4×10^7 . This n in turn predicts that 21 weight per cent or about 22.5 volume per cent eutectic will be found in the alloy.

The measured C_m^0 is considerably higher than the 0.67 weight per cent phosphorus content which is the composition of the solid which first forms from the liquid according to the phase diagram. It is in fact fairly close to the room temperature solid solubility of 1.9 per cent phosphorus given in the phase diagram. The corresponding fraction eutectic is not in agreement as 15.3 weight per cent eutectic would be expected for equilibrium conditions. This discrepancy indicates that solid state diffusion should be taken into account in order to predict more accurately the solute redistribution in this iron phosphorus alloy. It would be expected to be necessary for other alloys in this system as well.

Based on the dendrite arm spacing measurements made and the solidification times measured in the iron-nickel alloys which may be assumed proportional to the actual solidification times in the iron-phosphorus system, a comparison of calculated and experimental data is listed in Table 6-9. The resulting correction factors for the iron-phosphorus alloy were 0.193 based on primary dendrite arm spacing and 0.556 based on secondary dendrite arm spacing. Correlation should improve if actual solidification times are measured for this alloy because of its large solidification range compared to the iron-nickel alloys.

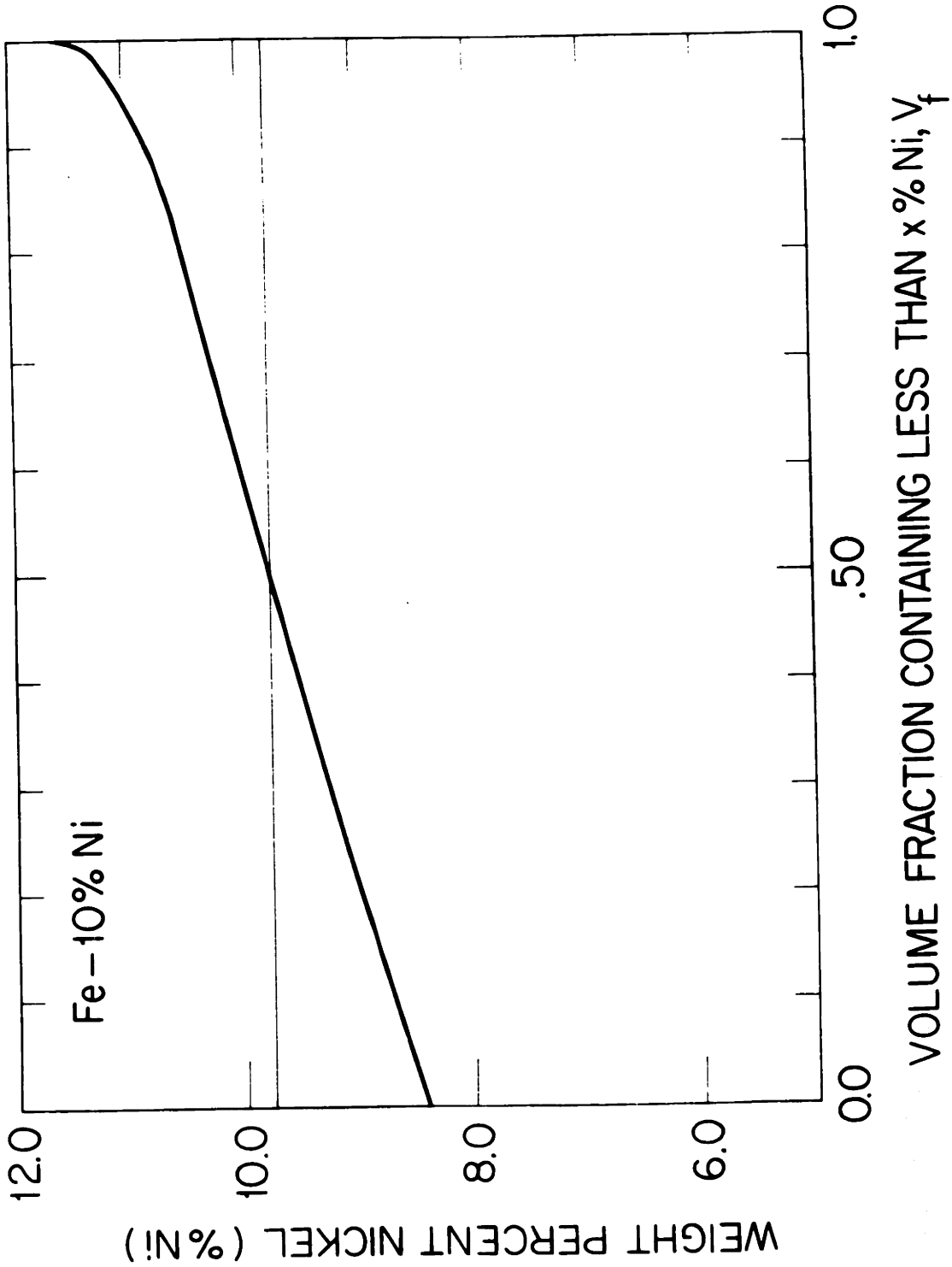


Figure 6-1. Typical cumulative composition curve. Iron-10 per cent nickel
2 inches from the chill.

TABLE 6-1

Electron Probe Microanalyzer Results

Distance from chill, inches	C_M^o (% Ni)	C_m^o (% Ni)	$\frac{S_e^o}{C_M^o/C_m^o}$
Iron-10 % Nickel			
1/2	11.6	8.59	1.35*
1	11.3	8.58	1.32*
2	11.6	8.40	1.38*
4	11.6	8.40	1.38*
Iron-26 % Nickel			
1/2	32.6	25.5	1.28**
1	30.0	24.5	1.26**
2	29.5	25.2	1.17**
4	29.8	25.2	1.18**

*Measured on the Norelco Microprobe Analyzer.

**Measured on the Applied Research Laboratory Microprobe Analyzer.

TABLE 6-2

Comparison of the Correction Factors for primary dendrite arm spacings calculated for the Iron-26 per cent nickel alloy and iron-10 per cent nickel alloy with the Mass Balance Technique:

<u>Alloy</u>	<u>Plate Model</u>	<u>Cylinder Model</u>
Iron-26 per cent nickel	0.125	0.164
Iron-10 per cent nickel	0.129	0.167

TABLE 6-3

Comparison of Measured and Theoretical Segregation Ratios, Iron-26 Per Cent Nickel Alloy - Mass Balance Technique - Plate Model

Calculations Based on Primary Arm Spacing:

Location X (in.)	Solidification Time, θ_f (seconds)	Dendrite Arm Spacing, 2λ (cm x 10^4)	η_e (sec $\text{cm}^{-2} \times 10^{-5}$)	η_c (sec $\text{cm}^{-2} \times 10^{-6}$)	S'_e	S^0_c
(a)	(b)	(c)	(d)			
1/2	2.6	73	.195	12.1	1.28	1.29
1	7.3	110	.257	15.9	1.22	1.23
2	24.1	160	.374	23.1	1.17	1.15
4	86.6	350	.278	17.2	1.18	1.21

Calculations Based on Secondary Arm Spacing:

(a)	(b)	(c)	(d)	(e)
1/2	2.6	40	6.55	71.8
1	7.3	51	11.20	12.3
2	24.1	72	18.10	19.9
4	86.6	104	30.80	33.7

(a) Taken from Figure 4-3.

(b) Measured Primary Arm Spacing, Figure 5-18.

(c) $\eta_e = \frac{\theta_f}{\lambda^2}$

(d) $\eta_c = \frac{\theta_f}{(g\lambda)^2}$, g is a correction factor found to be 0.127 for primary arms and 0.303 for secondary arms.

(e) Measured Secondary Arm Spacing, Figure 5-20.

TABLE 6-4

Comparison of Measured and Theoretical Segregation Ratios, Iron-10 Per cent Nickel - Mass Balance Technique - Cylinder Model (Calculations based on primary arm spacing.*)

Location X (in.)	Solidification Time, θ_f (seconds)	Dendrite Arm Spacing, 2λ (cm x 10^4)	η_e (sec/cm ² x10 ⁻⁶)	η_c (sec/cm ² x10 ⁻⁶)	S_e	S_c
	(a)	(b)	(c)	(d)		
1/2	2.6	49	.433	15.5	1.35	1.53
1	7.3	73	.548	19.6	1.32	1.37
2	24.1	127	.596	20.3	1.38	1.35
4	86.6	233	.635	22.7	1.38	1.27

* Calculations were made based on primary arm spacings only as secondary arms were not measurable.

(a) Taken from Figure 4-3.

(b) Measured primary arm spacing, Figure 5-18.

(c) $\eta_e = \frac{\theta_f}{\lambda^2}$

(d) $\eta_c = \frac{\theta_f}{(g\lambda)^2} = \frac{\eta_e}{g^2}$, g is an average correction factor found to be 0.165 for primary arms

using the Mass Balance Technique - cylinder model for the alloys tested.

TABLE 6-5

The Effect of Carbon on Microsegregation in an
Iron-26 Per Cent Nickel Alloy - 2 Inches from the Chill

Chemical Analysis	C_M^O	C_m^O	S_e^O
Wt.% C	Wt.% Ni	Wt.% Ni	
-	29.2	23.9	1.22
.33	26.8	22.4	1.19
.42	26.4	22.7	1.16

TABLE 6-6

Measurements of the Composition Deviation Index, σ_m^o and Results Predicted by the Mass Balance Technique - Plate Model Based on Primary Dendrite Arm Spacings

Alloy	Position	σ_{mc}^o	σ_{me}^o	n_c
		(a)	(b)	
Fe-10% Ni	1/2 in.	0.32	0.052	3.2
Fe-10% Ni	1 in.	0.32	0.056	4.0
Fe-10% Ni	2 in.	0.32	0.067	4.3
Fe-16% Ni	2 in.	0.064	0.042	2.38

-
- (a) Obtained from plots of σ_m^o versus n by using n_c values where $n_c = \theta_f / (g^l)^2$.
- (b) Calculated by graphical integration of composition distribution curves.

TABLE 6-7

Volume Per Cent Eutectic Measured Metallographically at
different distances from the chill.

<u>Distance from the Chill</u>	<u>Volume Per Cent</u>	<u>Weight Per Cent</u>
1"	28.3 \pm 1.5*	26.4
2"	28.5 \pm 1.5*	26.5
3"	27.5 \pm 1.5*	25.7
4"	27.0 \pm 1.5*	25.2

* Estimate of statistical error for a coarse mesh two
dimensional systematic point count analysis.

TABLE 6-8

Electron Microprobe Analysis for Minimum Phosphorus Contents at Different Distances from the Chill

<u>Distance from the chill X, (inches)</u>	<u>Minimum Solute Content C_m (wt. % P)</u>
1/2	2.2
2	2.1
4	2.0

TABLE 6-9

Results of Wet Chemical Analysis on the Iron Phosphorus Ingot

Distance from the Chill X(inches)	Analysis	Analysis	Analysis	Analysis	Analysis
	1* wt. % P	2* wt. % P	3** wt. % P	4** wt. % P	5*** wt. % P
1/2	3.30	3.14	4.04	4.08	4.3
4	-	3.59	3.93		4.1
7-1/2	3.70	3.01 3.20	3.80		

*Analyses performed at the M.I.T. Analytical Laboratory by the same analyst.

**Analyses performed at the Arnold Greene Testing Laboratories by different analysts.

***Analyses performed on an electron beam microprobe analyzer.

TABLE 6-10

Comparison of the Weight Per Cent Eutectic Predicted by the Mass Balance Technique - Plate Model with that Measured Experimentally for the Iron-4.0 Per Cent Phosphorus Alloy.

Position X(inches)	Solidification Time θ_f (seconds)	Dendrite Arm Spacing, 2λ (cm $\times 10^4$)	η_e		η_c	f_{E_e} wt %	f_{E_c} wt %
			(a)	(b)			
1	7.3	122	.196	.196	5.27	26.4	26.3
2	24.1	220	.199	.199	5.33	26.5	26.2
3	50.5	300	.224	.224	6.03	25.7	26.0
4	86.6	380	.240	.240	6.45	25.2	25.7

Based on Secondary Arm Spacing

Position X(inches)	η_e		η_c	f_{E_e} wt %	f_{E_c} wt %	
	(a)	(b)				
1	2.6	50	1.16	3.75	26.4	26.8
2	7.3	73	1.80	5.82	26.5	26.1
3	24.1	100	2.02	6.52	25.7	25.8
4	86.6	108	2.98	9.64	25.2	25.0

- (a) Taken from Figure 4-3.
- (b) Measured Dendrite Arm Spacing taken from Figure 5-21.
- (c) $\eta_e = \frac{\theta_f}{\lambda^2}$
- (d) $\eta_c = \frac{\theta_f}{g \lambda^2} = \frac{\eta_e}{g^2}$, g is a correction factor found to be 0.193 based on primary arm spacings and .556 for secondary arm spacings.

VII. Summary and Conclusions

- (1) A new computer program, the Mass Balance Technique, was written to simulate solidification and post-solidification heat treatments by using numerical analysis techniques. The program may be applied to eutectic alloys as well as those in which (a) the final solidification temperature and composition are variable; and (b) substantial diffusion occurs in the solid both during and after solidification. Featured are the options of a cylinder or plate model, a growth rate in the solidification range which may be linear, parabolic, or determined by a cooling curve, or cooling expression, and the use of any desired cooling curve or cooling expression from the solidus temperature to room temperature.
- (2) The amount of microsegregation measured in iron-nickel alloys and the iron-phosphorus alloy, did not conform to calculations for equilibrium solidification or normal non-equilibrium solidification. The discrepancy occurs because diffusion in the solid state is neither perfect nor non-existent during solidification and cooling to room temperature. Solid state diffusion occurs on a limited basis and must be taken into account to obtain a more accurate result in an analysis of solute redistribution.
- (3) In the iron-nickel system the segregation ratio varied from 1.15 to 1.38 depending on solidification conditions and alloy content. Segregation ratios for the iron-10 per

cent alloy ranged from 1.32 to 1.38 while for the 26 per cent nickel alloy, they varied from 1.15 to 1.28, exhibiting a slight increase with increasing cooling rate.

- (4) The effect of adding carbon to iron-nickel binary alloys was to decrease the nickel segregation slightly. S^0 averaged approximately 1.22 for iron-26 per cent nickel alloy containing no carbon, and this decreased to about 1.16 with addition of 0.42 per cent carbon.
- (5) The computer results and the experimental measurements in the iron-nickel and iron-phosphorus alloys studied are in good qualitative agreement as the predicted and measured microsegregation varied only slightly with cooling rate (distance from the chill). To obtain quantitative agreement the measured dendrite arm spacing must be multiplied by a correction factor. In the iron-nickel alloy system based on primary dendrite arm spacing for the Mass Balance Technique a factor of 0.127 must be used for the plate model and 0.165 for the cylinder model. Based on secondary arm spacings measured in the iron-26 per cent nickel alloy, the correction factor is 0.303 for the plate model and 0.378 for the cylinder model. For the iron-phosphorus alloy, to obtain the correct fraction eutectic, the primary arm spacing must be multiplied by 0.193 and the secondary arm spacing by 0.556.
- (6) Computer analysis shows that the effect of parabolic growth, as compared to linear, is to lower the segregation slightly for equivalent solidification time. This is because

longer diffusion periods are allowed at the end of solidification when the concentration gradients are steepest, and hence diffusion greatest.

- (7) More diffusion is predicted for a cylindrical model than for a plate.
- (8) Dendrite morphology was examined in iron-nickel alloys containing 10 to 26 per cent nickel, iron-nickel-carbon alloys containing approximately 26 per cent nickel and up to 0.42 per cent carbon and iron-4.0 per cent phosphorus, and iron-25.0 per cent copper. "Cellular" structures resulted in the iron-nickel alloys studied which were of low alloy content and solidified under conditions of high cooling rates. Lower cooling rates and higher solute contents produce more complex dendrite structure including secondary, tertiary, and even quaternary branching. The phosphorus had a strong tendency to form higher order growth forms even adjacent to the chill. The iron-25 per cent copper alloy exhibited branching and a cruciform structure in planes parallel and adjacent to the chill surface. Rather than forming higher order growth forms, these cruciforms enlarged as the distance from the chill increased retaining a clover-leaf shape. The alloy structure in the iron-nickel and iron-phosphorus alloys increased in complexity as the cooling rate decrease.
- (9) Primary dendrite arm spacing in the ingots studied ranged from about 40 to 700 microns, depending on the alloy analysis and cooling rate. Dendrite arm spacing was found

to increase with (a) decreasing cooling rate in the iron-nickel, iron-nickel-carbon, iron-phosphorus, and iron-copper alloys studied, and in addition in the iron-nickel system with (b) increasing nickel content (at least in the range 15 to 26 per cent nickel), and (c) carbon additions.

- (10) Secondary arms in the alloys examined ranged from unobservable for the cellular structure found near the chill in the iron-10 per cent nickel alloy to those well formed. The latter were found to be promoted by (a) higher alloy contents, (b) carbon additions, and (c) slower cooling rates. The well formed secondaries within each casting always had a smaller spacing than the primary measurements in equivalent positions with respect to the chill.
- (11) The secondary dendrite arm spacings measured, all of which fell within the 40 to 200 micron range, were not affected by the cooling rate as much as the primary arm spacings. This was shown by the flatter curve obtained by plotting secondary dendrite arm spacing versus distance from the chill compared to a plot of primary spacings.

VIII Suggestions for Further Work:

- (1) Compilation of data by electron beam microprobe analysis of other ferrous and nonferrous binary alloys including several eutectics, such as magnesium-zinc, and application of the Mass Balance Technique computer program to predict the proper segregation parameters.
- (2) Development of the Mass Balance Technique to include ternary systems:
 - (a) For systems in which one solute component retains the solid distribution that it had at the solidus temperature while the other diffuses in the solid, i.e., iron chromium carbon.
 - (b) For systems in which both solute components diffuse in the solid.
- (3) Investigation into the significance of the shape of the measured composition deviation index including a statistical interpretation of the electron beam microprobe analyzer data.
- (4) Work on the high temperature properties of the systems studied including diffusion, and solidification ranges and times, to attempt to explain the reason for the necessity of a correction factor so that it may be eliminated.
- (5) Insertion of steps into the computer program which will account for solidification shrinkage.

BIBLIOGRAPHY

1. Rosenberg, R.A., Flemings, M.C., and Taylor, H.F., Hot Tearing in Nonferrous Binary Alloys, Trans. AFS, 68, 1960, p. 518.
2. Flemings, M.C. "Fluidity of Metals," Transactions 30th International Foundry Congress, Prague, 1963, p. 61.
3. Smith, T.B., Thomas, J.S., and Goodall, R., Banding in a 1 1/2 Per Cent Nickel Chromium Steel, JISI, 209, 1963, p. 602.
4. Poirier, D.R., Polich, R.F., and Flemings, M.C., "Development of Superior Steels for Precision Gyro Spin Bearings," MIT, Contract No. AF33(615)-1030, Wright-Patterson Air Force Base, Ohio, 1964.
5. Uhlig, H., Corrosion and Corrosion Control, John Wiley and Sons Inc., New York, 1961, pp. 15, 105-109.
6. Flemings, M.C., "Controlled Solidification" Presented at Twelfth Sagamore Army Materials Research Conference, August 24-27, 1965.
7. Flemings, M.C. "Microsegregation in Castings and Ingots," Hoyt Memorial Lecture, Trans. AFS 72, 1964.
8. Pfann, W.G., Zone Melting, John Wiley and Sons, Inc., New York, 1958, p. 10.
9. Scheil, E., Zeit. fur Metallkunde, 1942, 34, pp. 70-72.
10. Investigation of Solidification of High Strength Steel Castings, M.I.T. Interim Report, Contract No. DA-19-020-ORD-5443(X), Army Materials Research Agency, October 1963.
11. Kattamis, T.Z., Flemings, M.C., "Dendrite Morphology, Microsegregation, and Homogenization of Low Alloy Steel," Trans. AIME, 223, 1965, pp. 992-999.

BIBLIOGRAPHY (Continued)

12. Bower, T.F., Brody, H.D., and Flemings, M.C., "Measurement of Solute Redistribution in Dendritic Solidification," Accepted for Publication, Trans. AIME.
13. Kattamis, T.Z., Flemings, M.C., Dendrite Morphology, Microsegregation, and Homogenization of Low Alloy Steel, Trans AIME, 233, 1965, pp. 992-999.
14. Poirier, D.R., Master of Science Thesis, Department of Metallurgy, M.I.T. 1963.
15. Quigley, F.C., Ahearn, P.J., "Homogenization of Steel Castings at 2500°F," Trans, AFS, 72, 1964, pp 813-817.
16. Brody, H.D., "Solute Redistribution in Dendritic Solidification," Doctor of Science Thesis, Department of Metallurgy, MIT, 1965.
17. Brody, H.D., Flemings, M.C., Investigation of Parameters Influencing Solidification of Aluminum Base Alloys," Annual Report, M.I.T. Contract No. DA-19-020-ORD-5706(A), Frankford Arsenal, July, 1963.
18. Bower, T.F., Brody, H.D., Flemings, M.C., Effect of Solidification Variables on the Structure of Aluminum Base Alloys," Annual Report Contract No. DA-19-020-ORD-5706(A), Frankford Arsenal, June, 1964.
19. Floyd, R.W., "The Equilibrium Diagram of the System Iron Nickel," Annotated Equilibrium Diagrams, No. 11, The Institute of Metals, 1955.
20. Metal's Handbook, A.S.M., 1948, p. 1213.

BIBLIOGRAPHY (Continued)

21. Goldstein, J.I., Doctor of Science Thesis, Department of Metallurgy, MIT, 1964.
22. Seibel, G., "Diffusion du Soufre et du Phosphore dans le Fer à l'état solid," Mémoires Scientifiques Rev. Metallurg, LXI, N^o 6, 1964, p. 432.
23. Brown, P.A., Adams, C.M., Trans. AFS, 69, 1961, p. 879.
24. Bardes, B.P., Sc.D. Thesis, Department of Metallurgy, M.I.T., 1965.
25. "Investigation of Solidification of High Strength Steel Castings" MIT Interim Report, Contract No. DA-19-020-ORD-5443, Army Materials Research Agency, October, 1962.
26. Brody, H.D., Flemings, M.C., Solute Redistribution in Dendritic Solidification, Accepted for publication Trans. AIME.
27. Carslaw, H.S., Jaeger, J.C., Conduction of Heat in Solids, Clarendon Press, Oxford, 1959, p. 466.
28. Polich, R.F., Nereo, G.E., Flemings, M.C., "Directional Solidification Studies," Final Report, Foundry Section, Metals Processing Division, Department of Metallurgy, MIT, Department of the Army Ordnance Corps, Contract No. DA-19-020-AMC-5753(Z).
29. Hilliard, T.E., Cahn, J.W., An Evaluation of Procedures in Quantitative Metallography for Volume—Fraction Analysis, Trans.AIME , 221, April 1961, pp. 344-352.
30. Plaskett, T.S. and Winegard, W.C., Canadian Journal of Physics, 37, 1959, p. 1555.
31. Ziebold, T.O., Ogilvie, R.E., "An Empirical Method for Electron Microanalysis," Anal.Chemistry, 36, 1964, p. 322.

APPENDIX A

List of Symbols

A	Liquid solid interface area
(ASFD)	Analytic Solution Finite Difference Analysis
(ASFD)-(SC)	Analytic Solution Finite Difference analysis using a solute corrected envelope
b	$\frac{G_L D_L}{R_t m_L}$
C	Cylinder
C_m, C_m^i, C_m^o	Minimum solute concentration in solid dendrite at any temperature the nonequilibrium solidus and room temperature, respectively
C_M, C_M^i, C_M^o	Maximum solute concentration in solid dendrite at any temperature the nonequilibrium solidus and at room temperature, respectively
C_L^*, C_S^*	Concentration of solute at the interface in the liquid and solid, respectively
C_o	Initial alloy content
C_p	Heat capacity of solid
C_S	Composition at some point within the solid phase
\bar{C}_S	Average composition of the solid phase
d	Dendrite arm spacing
D_S, D_L	Diffusion coefficient of solute in solid and liquid phases, respectively
f_E	Fraction eutectic present
f_S, f_L	Weight fraction of solid and liquid phase, respec- tively

List of Symbols (Continued)

g	Geometric correction factor
G_L	Temperature gradient in the liquid at the dendrite tips
h	Exponent in the evolved time relationship involving λ , ℓ , and Θ_f
H'	Average heat released per unit weight of material solidified
j subscript	steps in distance
k subscript	steps in time
k	Equilibrium partition ratio
ℓ	One half the plate spacing
M	$\frac{\Delta\lambda^2}{D(T, C_S)\Delta\Theta}$
m_L	Slope of the liquidus line
(MBT)	Mass Balance Technique
n	Exponent in the dendrite arm spacing solidification time relationship
N_U, N_S	Total number of counts taken on the electron micro- probe analyses from sample and standard, respectively
p	Number of incremental time periods to keep $M \gg 4$ (Finite difference solution)
P	Plate
r_i	Position the liquid-solid interface along the radius of a cylinder growth model
R_T	Rate of advance of the dendrite tips
S, S', S^0	Segregation ratio at any temperature nonequilibrium solidus, and room temperature, respectively
T_E	Eutectic temperature

List of Symbols (continued)

T_K	Temperature, degrees Kelvin
T_L	Liquidus temperature
T_S, T'_S	Equilibrium solidus temperature and nonequilibrium solidus temperature, respectively
u	Rate of growth of dendrite plate
V	Volume
V_f, V_f^*	Volume fraction, volume fraction at which C equals C_0
X	Distance from chill
X_i	Position of metal interface
X_L	Position of liquidus isotherm
X_{Ni}	Mole per cent nickel
X_S	Position of nonequilibrium solidus isotherm
X_t	Position of dendrite tips measured from chill
w	Relative change in the concentration gradient in the solid at the interface due to diffusion
α	$\frac{D_S \theta_f}{2}$
n	θ_f / ℓ^2
θ	Time from the initiation of solidification
θ_f	Solidification time
θ_E	Elapsed solidification time until the liquid reaches eutectic composition
λ	Distance from centerline of plate
λ_E	Distance to the eutectic interface
E	Position of the liquid solid interface
i	

List of Symbols (Continued)

141

ρ_L, ρ_S Density of the solid and liquid respectively
 $\sigma_m, \sigma'_m, \sigma_m^0$ Composition deviation index at any temperature at the nonequilibrium solidus, and at room temperature, respectively

APPENDIX B - Primary Dendrite Arm Spacings*

Casting Distance from Chill	1 10 % Ni	2 15 % Ni	3 20 % Ni	4 26 % Ni	5 26 % Ni .1 % C	6 26 % Ni .3 % C	7 26 % Ni .4 % C	9 4 % P	10 25 % Cu
1/2	47		50	72 64	90	94 97	117	111	35
1	72	64	66	110 100 99	138 144	141 136 136	214 219	148	47
1-1/2		98	97	114 135	208	177 188		177	67
2	114 124	107	126	172 183 162 180	309 333	228 245 236	366	221	73
2-1/2	165 171	132 144	157 150	221 208	378 364	252 245		249	85
3	194 196			255 282	415 415	278 294		297	124
3-1/2		189	219	339	476 424	347 342		351	152
4	250 231 236	206	236	368 364	474 555 578	391 387 367	551		188
4-1/2	260 262	225	273	460 450	617 624	406 385			
5	268			680 610 730	642 730	426			
5-1/2	298 314	287	333 332		757 737				
6	334				795 802				

* Values in left of block obtained by Area Method; on right, Linear Method. See page 82 for explanation.

APPENDIX B - Secondary Dendrite Arm Spacing

Casting Distance from Chill	1	2	3	4	5	6	7	9	10
	10 % Ni	15 % Ni	20 % Ni	25 % Ni	25 % Ni .1 % C	25 % Ni .3 % C	25 % Ni .4 % C	4 % P	25 % Cu
1 in.	cells	cells	45	50	54	64 55	62 58	51	23
2 in.	88	89	78	73	80 87	80 83	82 77	72	37
4 in.	88	110	106	104	126	131	126	113	50

BIOGRAPHICAL NOTE

RICHARD VINCENT BARONE was born on January 4, 1937 in Arlington, Massachusetts. He received his secondary school education in the Belmont Massachusetts School System, graduating from Belmont High in June 1954. He was employed at the Massachusetts Institute of Technology Foundry Laboratory the summer prior to entering M.I.T. in September. He majored in Metallurgy as an undergraduate and did a thesis concerning the high temperature properties of a cobalt based super alloy. He participated and held office in numerous extracurricula activities which include: President of the American Foundrymen's Society Student Chapter, Vice President of the Student Metallurgical Society, Foreman of the Experimental Foundry Group, the Athletic Association, and the fraternal organization Phi Sigma Kappa. Following receipt of a Bachelor of Science Degree in June of 1958, Mr. Barone started work towards a Master's Degree at M.I.T. in the Solidification Group. During this period he received the American Brakeshoe Fellowship and a Foundry Educational Foundation Fellowship from the Wheelabrator Corporation. His thesis involved the development of high strength low alloy steels by controlled solidification. His Master's degree requirements were completed in June 1960 while working on the Walworth Company's Research and Engineering Staff as a Research Metallurgist, where he began in September of 1959. He continued at Walworth working on projects involving:

Biographical Note (continued)

high temperature creep rupture properties, x-ray analysis, radiography, gating and casting design, wear and abrasion studies, product failure analysis, corrosion, heat treating, joining materials by brazing and welding, electroplating, shell and green sand molding, and nondestructive testing.

In September of 1962 he returned to the M.I T. Solidification Group as a staff member in pursuit of a Doctor of Science Degree. His minor was in Business Administration which was taken at the Harvard Business School.

The author is a member of The American Society for Metals, American Institute for Metallurgical, Mining, and Petroleum Engineers, American Welding Society, American Foundrymen's Society, Society of the Sigma Xi, and was formerly a member of the Society of Nondestructive Testing, Society for Experimental Stress Analysis, National Society of Corrosion Engineers, and the American Society for Testing Materials.

He co-authored publications and reports including:

1. "Solidification of Steel Castings and Ingots," Trans. AFS, V69, 1961, pp. 422-435.
2. "Bronze Alloys Electric Melting and Quality Control,"

Biographical Note (continued)

Trans. AFS, V69, 1961, pp. 171-178.

3. "Investigation of Solidification of High Strength Steel Castings," Technical Report No. AMRA CR64-04/3.

